Enhancing High-Impact Rainfall Forecasts via Multi-Sensor, Multi-Stage Variational Data Assimilation in WRF: Insights from the CYGMEN Project

Dimitrelos Antonios[1], Fragkoulidis Georgios[1], Karagiannidis Athanassios[1], Vasiliki Kotroni[1], Lagouvardos Kostantinos[1], Oikonomou Christina[2,3], Haralambous Haris[2,4]

[1] National Observatory of Athens, Institute for Environmental Research and Sustainable Development, Athens, Greece
[2] CLOUDWATER LTD, Nicosia, Cyprus
[3] Frederick Research Center, Nicosia, Cyprus
[4] Frederick University, Nicosia, Cyprus

14 August 2026, **Preprint Statement:**
This manuscript is a non-peer-reviewed preprint submitted to EarthArXiv. Subsequent versions of the manuscript may have different content
Corresponding author: a.dimitrelos@noa.gr (ORCID: 0000-0002-6139-0474)

Abstract

Assimilating high-resolution radar reflectivity and complementary observation types remains a central challenge for improving short-term quantitative precipitation forecasts of severe Mediterranean weather systems. This study investigates the effect of multi-source data assimilation configurations using the Weather Research and Forecasting (WRF) model and its three-dimensional variational data assimilation system (3D-Var) to simulate the impact of storm Bora over Greece. Specifically, we evaluate the adjustments induced by synchronous versus multi-stage sequential assimilation of radar reflectivity, Global Navigation Satellite System (GNSS) precipitable water vapor, and surface synoptic observations (SYNOP), while exploring the impact of single versus multiple radar cost-function minimization loops. Diagnostic analysis of thermodynamic increments and low-level transport, combined with categorical forecast verification metrics, reveals that two-stage sequential configurations systematically outperform synchronous methods across light to heavy precipitation regimes. Synchronous ingestion induces localized diabatic heating that artificially deforms the 850 hPa geopotential height field, displacing low-level thermodynamic pathways westward. Conversely, sequential configurations introduce radar echoes into a moisture-corrected background state, preserving favorable thermodynamic profiles and localized storm trajectories. Furthermore, a distinct trade-off governs radar minimization: three minimization loops refine widespread stratiform structures (15–20 mm), whereas a single loop prevents the over-smoothing of peak intensities, yielding enhanced skill for heavy convective cores (30–40 mm). Finally, anchoring the lower troposphere with SYNOP observations provides a horizontal constraint that restricts low-level moisture transport, yielding a substantial relative improvement in predicting short-term heavy rainfall. These insights provide an operational framework for optimizing multi-source data assimilation setups during severe convective events in complex marine-continental interfaces.

1. Introduction

The Mediterranean basin is prone to extreme, low-pressure atmospheric disturbances that pose socioeconomic threats to coastal and continental regions (Lionello et al., 2006). Due to the combination of complex coastal topography and proximity to a warm maritime moisture source, these synoptic systems frequently trigger intense convective cells and catastrophic flash floods (Llasat et al., 2010; Michaelides et al., 2018). The heavy rainfall associated with these systems has been linked to the combined contribution of deep convection and warm conveyor belt transport, as well as to the efficient recycling of remote moisture sources into an anomalously large water budget (Flaounas et al., 2018; 2019). Among the most severe manifestations of these low-pressure perturbations are Mediterranean cyclones termed "medicanes" (Miglietta et al., 2013; Miglietta, 2019; Miglietta et al, 2025). Recent high-impact events, such as medicane Ianos in 2020 (Lagouvardos et al., 2022) and storm Daniel in 2023 (Flaounas et al, 2025), underscore the profound vulnerability of Mediterranean societies, causing widespread negative impacts on agricultural and civil infrastructure, as well as human casualties (Flaounas et al., 2022; Khodayar et al., 2025). In Greece specifically, systematic documentation of high-impact weather events over the past two decades confirms that heavy precipitation and flooding remain the leading cause of weather-related socioeconomic damage nationwide (Papagiannaki et al., 2013; 2026). Given these risks, accurate high-resolution short-term quantitative precipitation forecasts remains a paramount operational necessity.

Despite the continuous advancements of computational capabilities, Numerical Weather Prediction models without ingestion of observation local high precision and resolution data may not be able to provide sufficient predictive skill for localized convective precipitation. This limitation is particularly evident in severe Mediterranean cyclones, whose strong sensitivity to initial conditions makes accurate prediction difficult (Davolio et al., 2009; Ricchi et al., 2017). To address these forecasting challenges, the meteorological community has increasingly turned to data assimilation techniques and ensemble forecasting methodologies (Kalnay, 2003). By integrating observations seamlessly into the model's initial state, data assimilation minimizes initialization errors and enhances overall forecast quality.

Atmospheric data assimilation began with simple spatial objective analysis and optimal interpolation methods, eventually evolving into the multi-dimensional variational suites utilized in modern operational systems, such as the Weather Research and Forecasting Data Assimilation (WRFDA) framework (Barker et al., 2004; 2012; Huang et al., 2009). Three-Dimensional Variational (3D-Var) data assimilation, whose theoretical framework was established by Lorenc (1986), has become one of the most widely adopted techniques in operational weather prediction. Its primary advantage is operational efficiency; it simultaneously ingests numerous heterogeneous observations with a fraction of the computational expense required by more complex four-dimensional variational (4D-Var) or ensemble-based Kalman filtering (EnKF) configurations (Bannister, 2017). However, the main disadvantage of 3D-Var is that it cannot adapt dynamically to flow-dependent structures associated with rapid storm development.

Despite this limitation, the implementation of multiple outer loops (Hsiao et al., 2012; Maiello et al., 2014) and staged (two-step assimilation) physical configurations (Tong et al., 2016) allows 3D-Var to remain a highly adaptable and effective tool for mesoscale analysis initialization.

Beyond the choice of variational method, the specific observation types ingested strongly shape the quality of convective-scale precipitation analyses. Radar reflectivity has been shown to constrain the moisture and hydrometeor fields most directly, with 3D-Var radar data assimilation schemes (Xiao and Sun, 2007; Xiao et al., 2007) yielding consistent short-range quantitative precipitation forecast improvements across a range of convective regimes. Global Navigation Satellite System (GNSS) derived precipitable water vapor and zenith total delay have likewise been assimilated to correct pre-convective moisture biases, with documented benefits for both water vapor and precipitation forecasts using 3D-Var/4D-Var frameworks over Poland (Rohm et al., 2019) and Greece (Giannaros et al., 2020), and using Global Positioning System (GPS) nudging over the wider Mediterranean and central European domain (Caldas-Alvarez and Khodayar, 2020). Surface synoptic observations (SYNOP), meanwhile, remain a comparatively low-cost but effective constraint on the low-level thermodynamic state, anchoring near-surface moisture and temperature fields that condition subsequent convective initiation. While each of these observation types has been evaluated individually, or in simultaneous combination, considerably less attention has been paid to how the order in which they are ingested, either simultaneously within a single cost-function minimization or sequentially across successive analysis stages, affects the resulting increments and precipitation forecast.

The primary aim of this study is to improve short-term precipitation forecasts during a typical, severe Mediterranean low-pressure system that yields high total accumulations and extreme hourly rainfall rates. This research is designed to shed light on how specific data streams, observation combinations, and mathematical cycling loops alter the resulting precipitation patterns. To achieve this, a variety of observational sources are utilized within different data assimilation configurations using the Weather Research and Forecasting (WRF) model. Thus, a sensitivity study is carried out to address the question: “Which data assimilation configurations improve forecast quality, and what are the underlying physical mechanisms driving these improvements?". In doing so, this study extends prior single-sensor or purely simultaneous multi-sensor assimilation studies by directly contrasting synchronous and multi-stage sequential ingestion strategies within a common 3D-Var framework, applied to a single high-impact rainfall event over a data-sparse, topographically complex Mediterranean domain.

2. Methods

2.1 Synoptic Overview of the Bora Storm

To evaluate the prognostic impact of the various observation combinations and data assimilation configurations, a representative severe convective and stratiform precipitation event within the eastern Mediterranean basin was selected. The high-impact storm, named "Bora", was associated with a deep cyclonic system that developed over the Adriatic Sea and traversed the Greek domain between 30 November and 02 December 2024. At the upper levels, the system was driven and sustained by a persistent cut-off low. The interaction between warm, maritime air masses originating from the Mediterranean and continental cold, dry air mass advected from the northeastern Balkan region generated intense thermodynamic instability which resulted in widespread heavy precipitation and localized flash flooding across northern and central Greece (Fig. S1). Rain gauge measurements highlighted extreme precipitation rates and high accumulated totals, particularly over Lemnos Island in the Aegean Sea and the Chalkidiki peninsula. The storm had a devastating impact on several regions of the country with heavy precipitation, landslides, and gale-force winds that caused infrastructure damage to road networks, ports, bridges, dams, and buildings, disruptions to transport, electricity, and water distribution networks, emergency evacuations, livestock losses, and three casualties. Lemnos Island was among the regions with the highest impact, suffering two casualties; on 30 November and 1 December, 208 mm of rainfall were recorded in the center of the island. Rhodes Island was also heavily affected, with 377 mm recorded in the city of Rhodes over the same period. In Central and Western Macedonia, the fire department received over 1660 calls for assistance with damaged trees, clearance of broken branches, water pumping, and evacuations. In Sithonia, Chalkidiki, a man died after being trapped in his car and suffering severe hypothermia. The weather station at the Simonopetra Monastery on Mount Athos recorded a total of 562 mm between 30 November and 2 December, while the nearby Neochori Chalkidiki station recorded more than 450 mm.

2.2 WRFDA Numerical Model and 3D-Var Assimilation Framework

Numerical simulations for the Bora storm event are conducted using the Advanced Research Weather Research and Forecasting (WRF-ARW) model (version 4.6.1) (Skamarock et al., 2019)**.** The computational configuration employs two-way nesting, consisting of a parent domain covering the European continent at a 10 km horizontal grid spacing, and an inner domain resolving the broader Balkan Peninsula at 2 km horizontal resolution. Vertically, the model employs 41 η (eta) levels, extending from the surface up to the model top at 50 hPa. Except for the cumulus scheme, identical model physics configurations were applied across both domains. Cloud and precipitation processes were represented using the Thompson bulk microphysics scheme (Thompson et al., 2008). Convective processes were parameterized on the outer domain using the scale-aware Grell-Freitas ensemble scheme (Grell and Freitas, 2014), whereas cumulus parameterization was disabled on the inner high-resolution domain to allow convection to be explicitly resolved. Boundary layer dynamics were parameterized using the Yonsei University (YSU) non-local planetary boundary layer scheme (Hong et al., 2006). Longwave and shortwave radiative transfer were modeled using the Rapid Radiative Transfer Model (RRTMG; Iacono et al., 2008). Finally, land surface processes were represented using the Unified Noah Land Surface Model (Tewari et al., 2004).

Initial and lateral boundary conditions are derived from the European Centre for Medium-Range Weather Forecasts (ECMWF) ERA5 reanalysis dataset (Hersbach et al., 2020). The simulation initializes on 30 November 2024 at 00:00 UTC and spans 48 hours, with lateral boundary conditions updated at 3-hour intervals.

Data assimilation is performed using the WRFDA system (version 4.6.1) configured for 3D-Var. According to the 3D-Var algorithm, the initial state of the atmosphere, called background (x_b), is adjusted by using observations (y) so that it comes closer to the real atmospheric state at that time. The new estimate of the atmospheric state is named analysis (x) and it is used to initialize the model. It is calculated by minimizing the following cost function $J(x)$, which quantifies how close the analysis is relative to both the background state and the observations:

$$J(x) = \frac{1}{2}(x - x_b)^T B^{-1}(x - x_b) + \frac{1}{2}\big(y - H(x)\big)^T R^{-1}\big(y - H(x)\big), \quad (1)$$

where B is the background error covariance matrix, R is the observation error covariance matrix, and H is the observation operator that converts x into the equivalent of the observations, allowing a direct comparison between them. The B matrix was calculated with the National Meteorological Center (NMC) method (Parrish and Derber, 1992). To capture climatologically similar precipitation events across the eastern Mediterranean, B was calculated over a 19-day window spanning 11 to 29 November 2024. Specifically, forecast differences were generated between 24-hour and 12-hour WRF predictions initialized every 12 hours ($T_{+24} - T_{+12}$). Calculations were performed using the CV5 control variable configuration utilizing streamfunction, unbalanced velocity potential, temperature, surface pressure, and relative humidity across 40 model levels. Horizontal length scales were modeled using a 6-pass recursive filter application (3 forward and 3 adjoint passes) to ensure Gaussian-like error correlation structures.

2.3 Experimental Design and Simulation Objectives

The simulation which does not include any data assimilation (NODA) serves as the baseline for subsequent comparison with the data assimilation experiments. The observational data ingested into the model include three-dimensional radar reflectivity volumes from two C-band Doppler radars provided by General Aviation Applications 3D S.A., GNSS Precipitable Water Vapor (PWV) data provided by the Balkan-Mediterranean Real-Time Severe Weather Service (BeRTISS) (Haralambous et al., 2018), and SYNOP data from the network of surface weather stations operated by the METEO unit of the National Observatory of Athens (NOA) (Lagouvardos et al. 2017). The radar reflectivity data underwent quality control to filter out ground clutter, partial beam blockage, and non-meteorological artifacts. The radar reflectivity data underwent quality control to filter out ground clutter and partial beam blockage (<50% retained; Wang et al., 2016). Low-reflectivity thresholding and observation selection rules were applied following Duda et al. (2019). Then, the observations were thinned to the nested WRF domain grid (2 km horizontal resolution) and the observational error was set to 5 dBZ (Choi et al., 2017; Duda et al., 2019). The locations and coverage range of the two radars are depicted in Fig. 1. Table 1 outlines the experimental simulations along with their corresponding data assimilation configuration and ingested observation types. To allow for model spin-up, data assimilation was performed 6 hours after initialization (06:00 UTC on 30 November 2024), utilizing a 30-min 3D-Var assimilation window. A total of 14,819 radar reflectivity, 202 SYNOP, and 48 GNSS PWV observations were ingested.

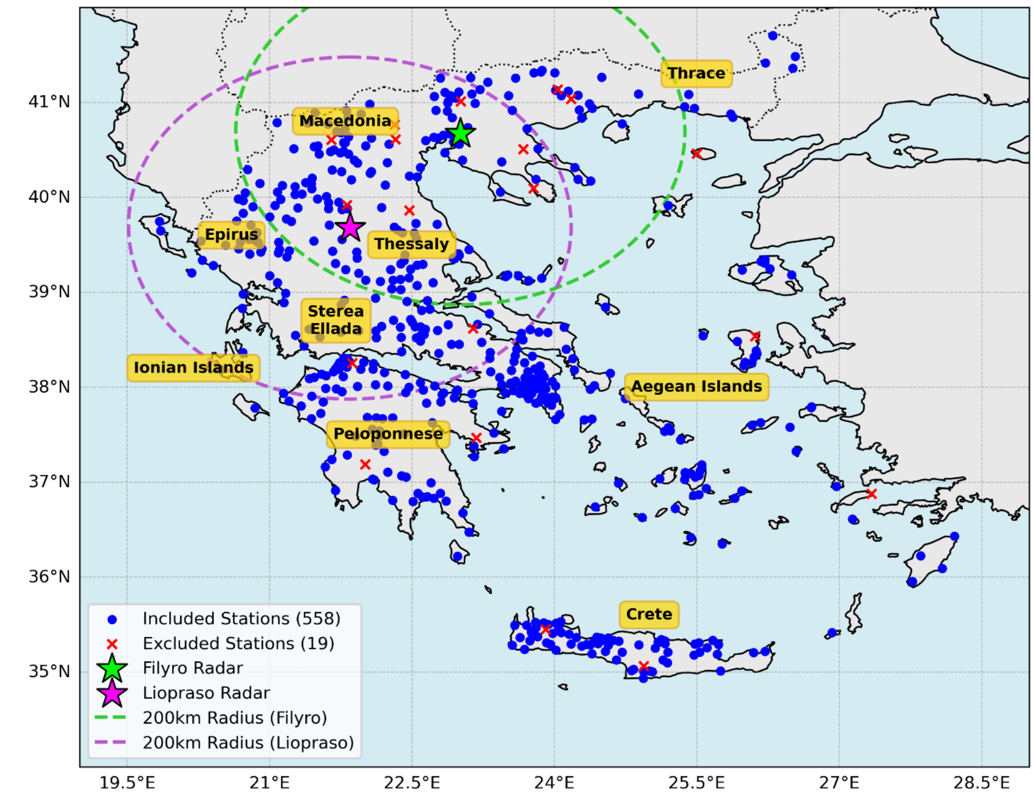

Fig. 1. Spatial extent of the inner (2 km horizontal resolution) WRF simulation domain, covering the broader Balkan Peninsula, together with the surface station network and radar coverage used in this study. Blue circles denote the 558 ground meteorological stations included in the verification analysis, whereas red crosses indicate the 19 stations excluded due to significant underestimation (>50 mm) during the Bora event. Green and purple stars mark the locations of the Filyro and Liopraso radars (40.67°N, 23.01°E and 39.67°N, 21.84°E, respectively), with green and purple dashed lines delineating their 200 km coverage radii.

Table 1. Summary of the experimental simulations, detailing the corresponding data assimilation architecture (synchronous versus sequential), the configuration of outer loops, and the specific categories of ingested observational datasets.

simulations	ingested observations	assimilation configuration
NODA	-	-
GN	GNSS PWV	3 outer loops
SY_GN	SYNOP & GNSS PWV	3 outer loops & synchronous ingestion
RADAR_OL1	Radar Reflectivity	1 outer loop
RADAR_OL3	Radar Reflectivity	3 outer loops
GN_RA_synch	GNSS PWV & Radar Reflectivity	3 outer loops & synchronous ingestion
SY_GN_RA_synch	SYNOP & GNSS PWV & Radar Reflectivity	3 outer loops & synchronous ingestion
GN_RA_stages	GNSS PWV & Radar Reflectivity	3 outer loops & sequential ingestion
SY_GN_RA_stages	SYNOP & GNSS PWV & Radar Reflectivity	3 outer loops & sequential ingestion

In the GN experiment, the GNSS PWV observations are the only observations assimilated, while in SY_GN they are combined with SYNOP observations. The synchronous ingestion implemented in SY_GN implies that both surface and column-integrated variables are optimized within the 3D-Var cost function simultaneously. For both experiments, a multi-outer-loop configuration (3 outer loops) was utilized in WRF DA. In this incremental approach, each outer loop updates the non-linear model trajectory and re-linearizes the observation operators around the latest analysis state, while the inner loops perform the linear cost function minimization. This ensures a smoother blending of the observations into the analysis. The RADAR_OL1 and RADAR_OL3 experiments utilize the radar reflectivity measurements configured with 1 and 3 outer loops, respectively. This study also addresses the deviations between synchronous and sequential (staged) data assimilation pathways when combining radar and conventional (GNSS, SYNOP) data. In GN_RA_synch, GNSS PWV and radar reflectivity are used simultaneously in a single cost function minimization. In contrast, GN_RA_stages handles these observations sequentially: the GNSS PWV is assimilated first, and the resulting analysis is then used as the background state for a second, separate 3D-Var minimization that ingests the radar reflectivity data. This pattern is altered to include SYNOP measurements in the final pair of experiments. SY_GN_RA_synch uses SYNOP, GNSS, and radar observations simultaneously. Conversely, the SY_GN_RA_stages establishes a thermodynamically well-balanced background state by first optimizing SYNOP and GNSS data synchronously, before ingesting the radar reflectivity to refine the microphysical structures of the cyclone. All these four configurations use 3 outer loops per minimization stage. SYNOP observations were not assimilated in isolation, as surface-only analysis provide limited constraint on the vertically integrated moisture field relevant to precipitation; they are therefore evaluated in combination with GNSS PWV throughout this study.

2.4 Precipitation Forecast Verification

To evaluate the impact of the various data assimilation strategies on quantitative precipitation forecasts, a station-based verification framework is employed. Precipitation forecasts of the 9 experiments are compared to in-situ surface observations from the METEO unit/NOA network over distinct temporal windows (6-hourly and 12-hourly interval accumulations). Observational datasets underwent quality control to filter out stations with missing or spurious records, resulting in the removal of 19 out of 577 stations (Fig. 1). To mitigate the "double-penalty" effect inherent to high-resolution grid-point verification (Ebert, 2008), a spatial upscaling (super-observation) technique is utilized. The 2 km inner model domain is partitioned into a coarser grid consisting of 10×10 km cells. Within each 10×10 km cell, point measurements from all enclosed surface stations are arithmetically averaged to yield a single representative observed precipitation value (i.e., a super observation). This upscaled observation is subsequently evaluated against the spatial mean of the corresponding 5×5 block of WRF grid cells (representing the equivalent 10×10 km neighborhood). This approach effectively assesses the aggregate rainfall volume within a localized neighborhood rather than disproportionately penalizing minor spatial displacement errors associated with convective cells. Statistical evaluation is performed using a contingency-table approach to derive standard categorical metrics, specifically the Critical Success Index ($\mathrm{CSI} = \frac{A}{A+B+C}$), Probability of Detection ($\mathrm{POD} = \frac{A}{A+C}$), False Alarm Ratio ($\mathrm{FAR} = \frac{B}{A+B}$), and the Frequency Bias ($\mathrm{FBIAS} = \frac{A+B}{A+C}$), where A, B, and C denote hits, false alarms, and misses, respectively. These skill scores are computed across a progressive range of precipitation intensity thresholds (from 5 mm to 40 mm, where each threshold x represents accumulated rainfall ≥ x mm) to evaluate model performance as a function of rainfall severity. To assess both country-wide impact and localized performance where most of the precipitation was measured (Northern Greece), all metrics are evaluated across two spatial domains: the entire Greek territory and a 200 km radius around the Filyro radar site in the broader Thessaloniki area (Fig. 1). In addition to these threshold-dependent categorical measures, continuous error statistics are computed to quantify the magnitude of precipitation forecast errors independent of any detection threshold. The Mean Absolute Error (MAE) and Mean Error (ME) are calculated for each experiment as:

$$\mathrm{MAE} = \frac{1}{N}\sum_{i=1}^{N}|F_i - O_i|, \qquad (2)$$

$$\mathrm{ME} = \frac{1}{N}\sum_{i=1}^{N}(F_i - O_i), \qquad (3)$$

where F_i and O_i are the modeled and super-observed accumulated precipitation values (mm) at verification cell i, and N is the total number of verification cells. Positive Bias values indicate a systematic overestimation of precipitation, while negative values indicate underestimation. This verification pipeline is executed over two aforementioned distinct spatial scales (whole Greek and radar regions) to isolate regional performance. The assessment focuses specifically on the 06:00–12:00 UTC and 06:00–18:00 UTC accumulation windows on 30 November 2024 to capture the core evolutionary phases of the storm event.

3. Results

3.1 Area-Aggregated Verification Across All Assimilation Configurations

Based on the calculated precipitation metrics for the accumulated rainfall we can infer which simulation performs better and captures the dynamics of the Bora storm. The CSI, along with the POD, FAR, and FBIAS are computed for the 6 and 12 hour accumulated rainfall after the data assimilation. As stated in the Methods section, two regions are examined; the whole Greek domain and a 200 km radius circular region around the Filyro radar site. In addition, verification is performed over a short (6 hours) and a longer period (12 hour) accumulation window to distinguish how the different kind of observations assimilation affect the forecast at different lead times. Figure 2 and 3 display the nationwide and radar area metrics, respectively, for 6 hours accumulated rainfall (06-12 UTC). The metrics are calculated for various accumulated rainfall thresholds (≥5, 10, 15, 20, 30, 40 mm) in order to distinguish the relative improvement or deterioration in different precipitation regimes. The same are shown in Figures 4 and 5 where the metrics refer to the 12-hour accumulated rainfall from 06 to 18 UTC. In addition, Figures 6 and 7 present the ME and MAE over the 6-hour window for the entire Greek domain and the radar sub-region, respectively. Similarly, Figures 8 and 9 show the corresponding 12-hour metrics for the Greek domain and the radar sub-region. Each bar in each figure is annotated with the relative improvement or degradation of the corresponding metric value (median ME and MAE in Figs. 6-9) compared to NODA, as well as the relative change in the interquartile range (IQR) in Figs. 6-9. The metrics are rounded to two decimal places and their relative improvements over NODA to whole numbers, whereas figures display unrounded values. Computed metrics are rounded to two decimal places, while relative improvements over NODA are rounded to whole percentages (unrounded values are shown in figures). The ≥ 40 mm threshold is omitted from Figure 3 due to a lack of detected events in the simulations. Additionally, the ≥ 15 mm threshold is excluded from ME and MAE investigation as it yields redundant information. The ≥ 30 and ≥ 40 mm thresholds are also excluded from the ME and MAE analyses within the 200 km radar domain for both 6- and 12-hour periods owing to few precipitation hits between the assimilated simulations and the baseline.

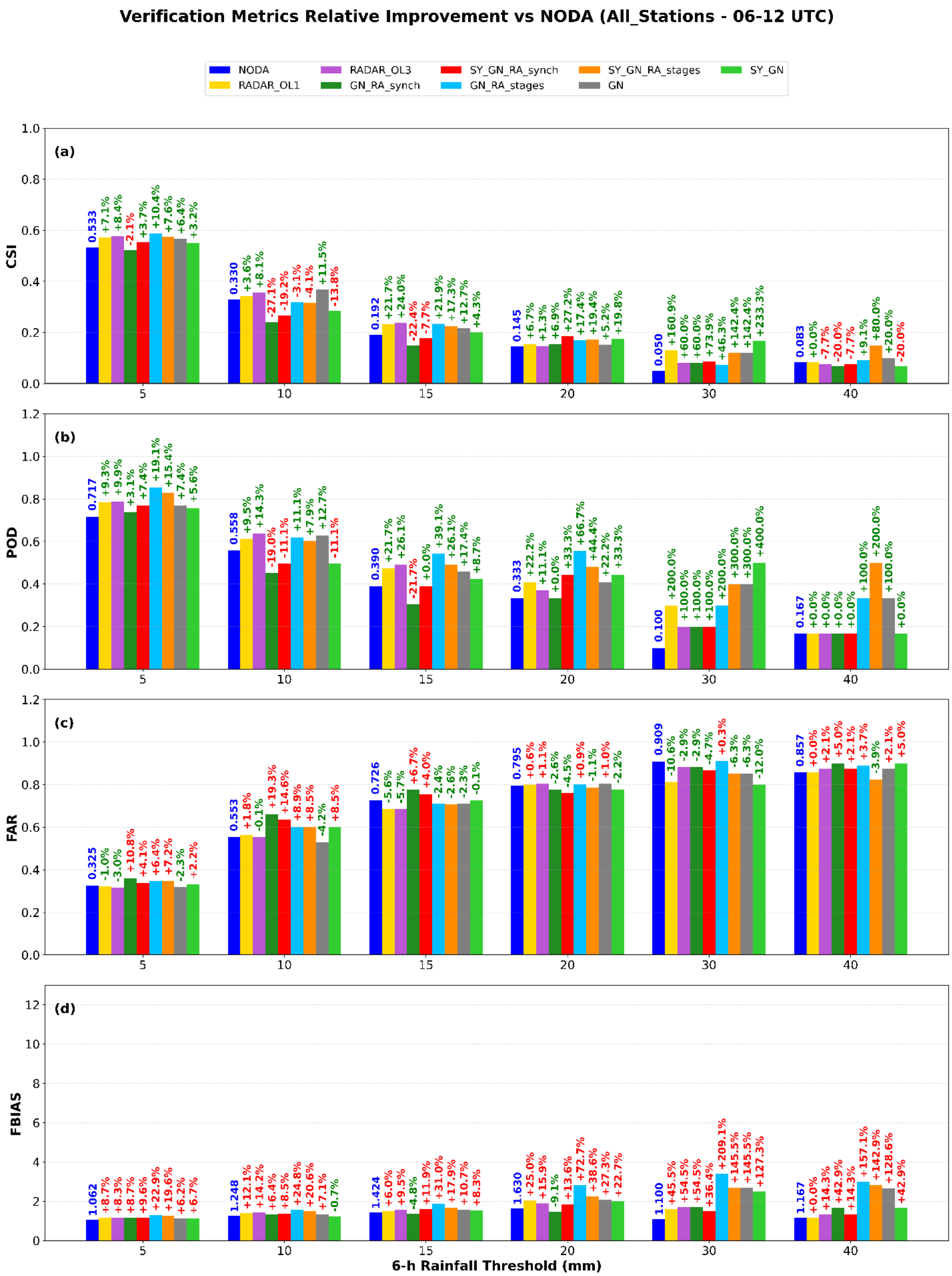

Fig. 2. The nationwide verification metrics CSI, POD, FAR, FBIAS for 6 hour (06-12 UTC of November 30, 2024) accumulated rainfall calculated over different precipitation thresholds (>5, 10, 15, 20, 30, 40 mm). Relative improvements (degradations) for each metric are annotated above the corresponding bars in green (red).

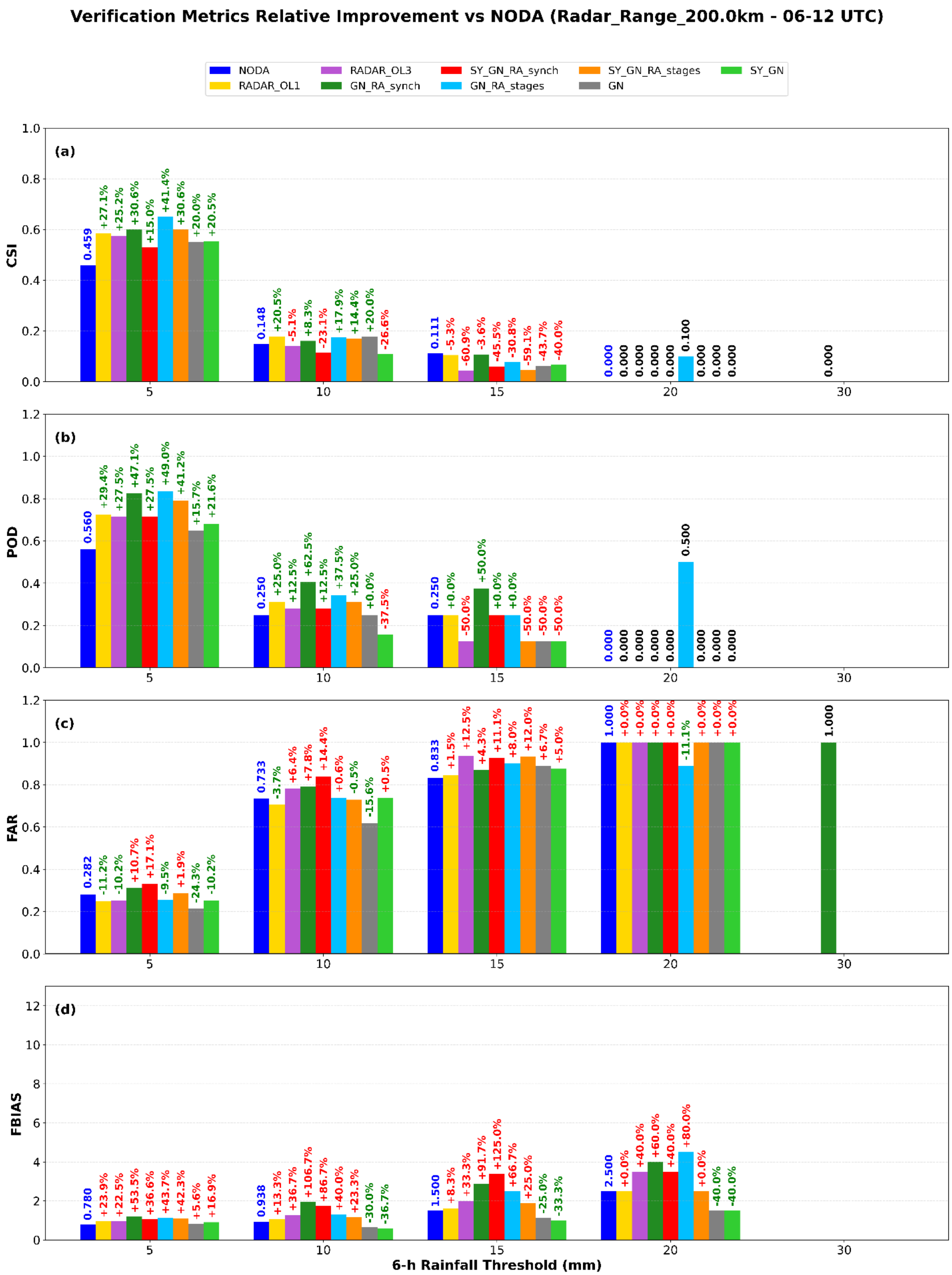

Fig. 3. The 200 km radius area around the Filyro radar site verification metrics CSI, POD, FAR, FBIAS for 6 hour (06-12 UTC of November 30, 2024) accumulated rainfall calculated over different precipitation thresholds (>5, 10, 15, 20, 30 mm). Relative improvements (degradations) for each metric are annotated above the corresponding bars in green (red).

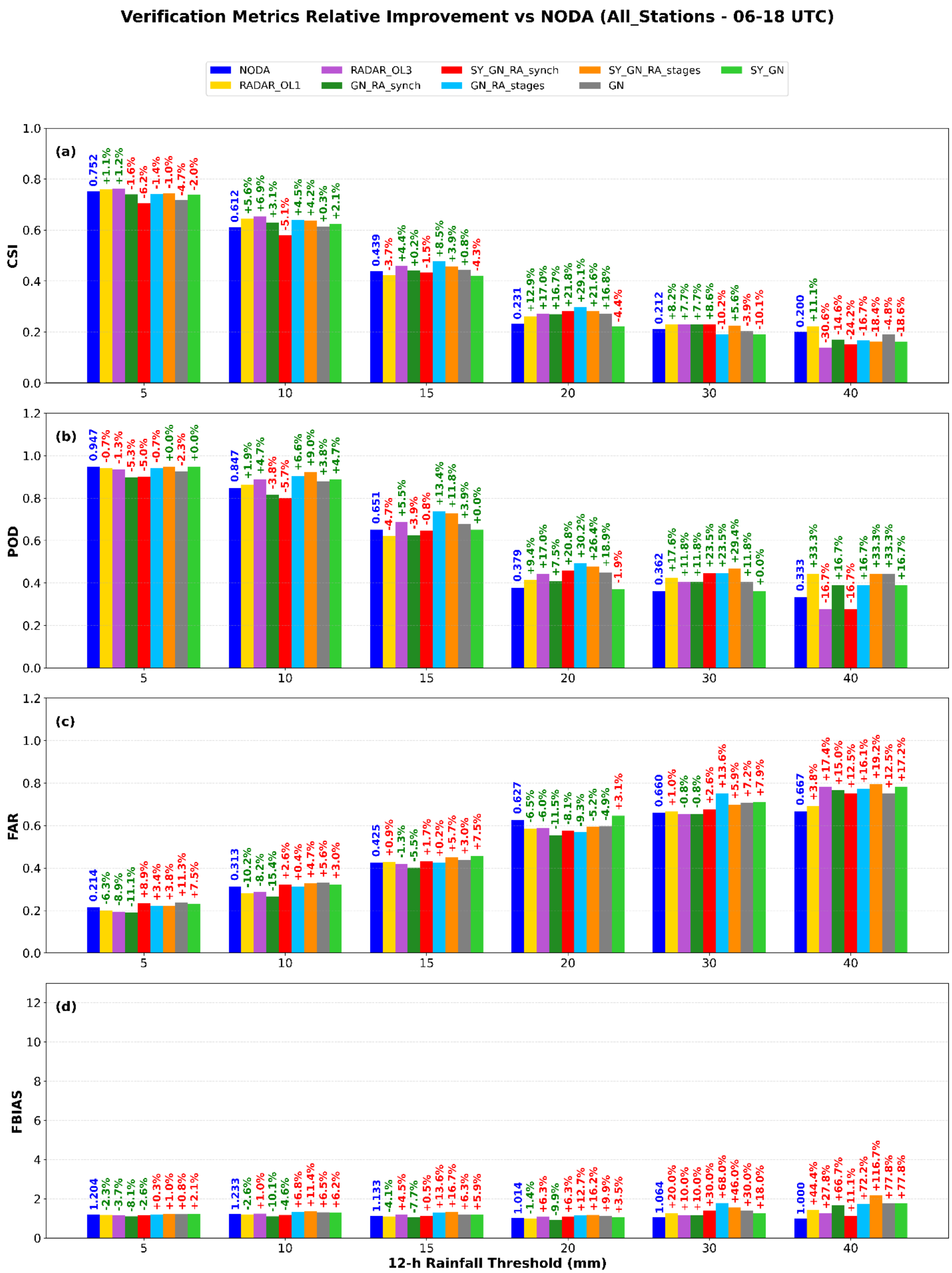

Fig. 4. The nationwide verification metrics CSI, POD, FAR, FBIAS for 12 hour (06-18 UTC of November 30, 2024) accumulated rainfall calculated over different precipitation thresholds (>5, 10, 15, 20, 30, 40 mm). Relative improvements (degradations) for each metric are annotated above the corresponding bars in green (red).

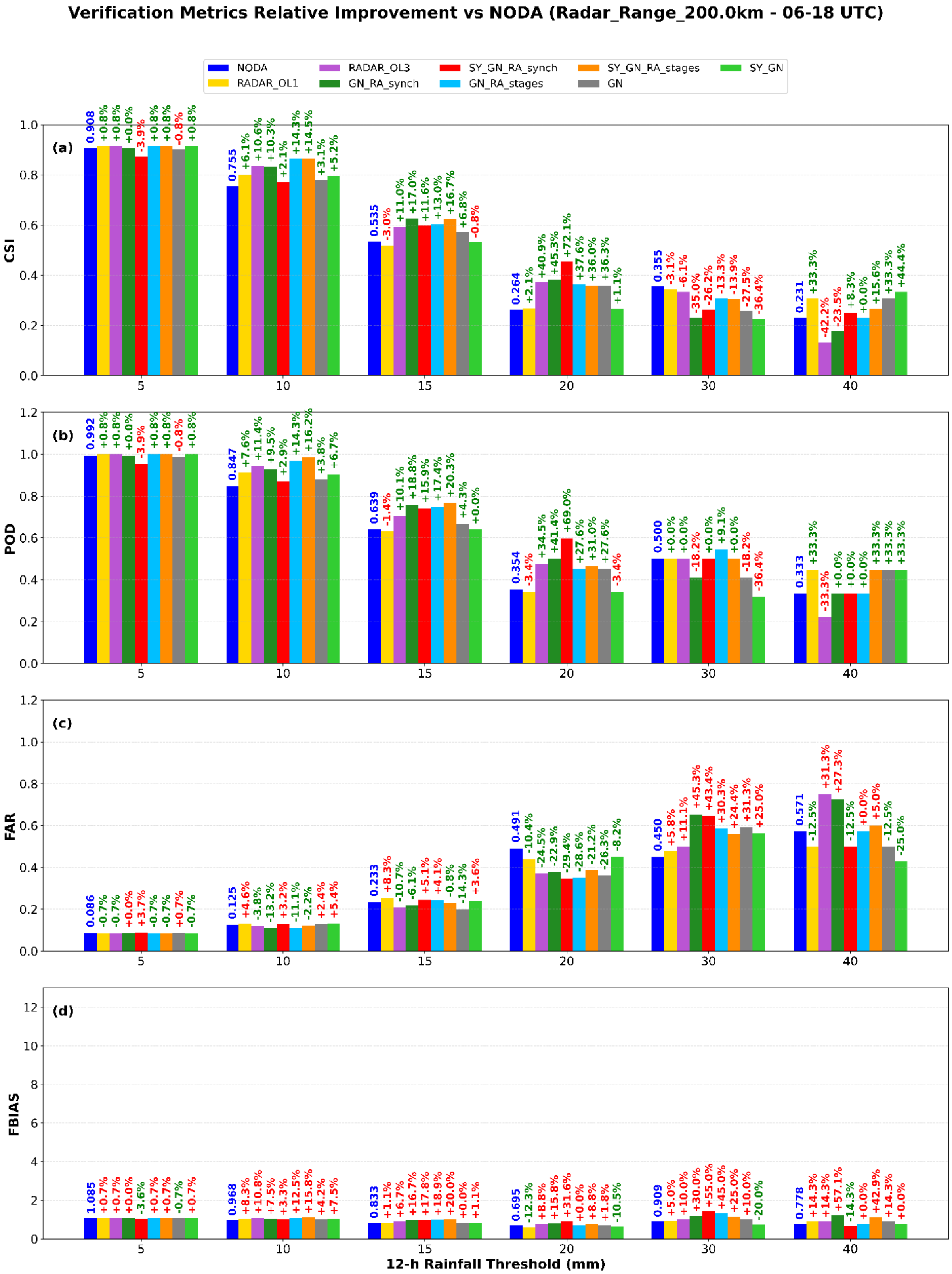

Fig. 5. The 200 km radius area around the Filyro radar site verification metrics CSI, POD, FAR, FBIAS for 12 hour (06-18 UTC of November 30, 2024) accumulated rainfall calculated over different precipitation thresholds (>5, 10, 15, 20, 30, 40 mm). Relative improvements (degradations) for each metric are annotated above the corresponding bars in green (red).

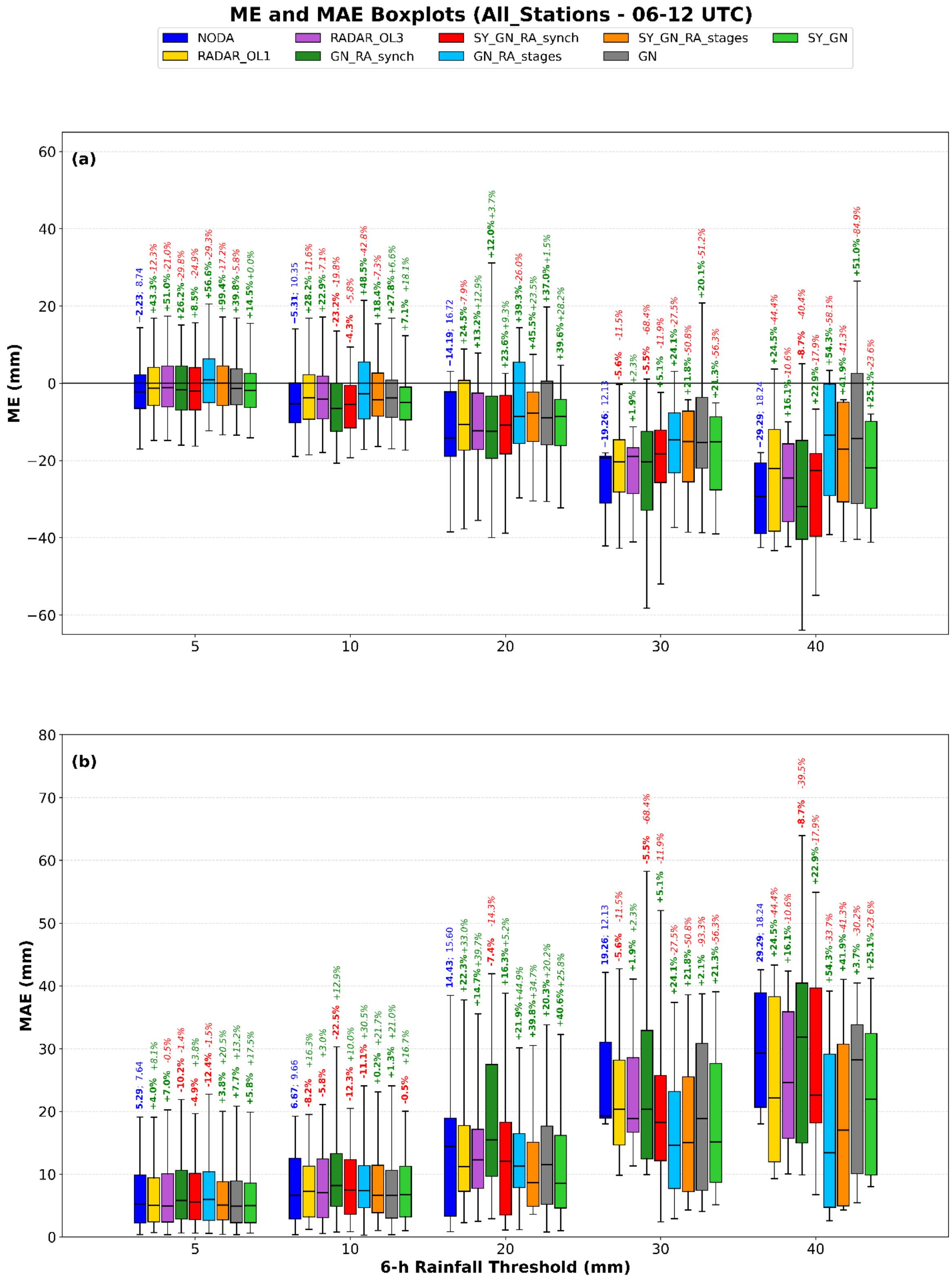

Fig. 6. The nationwide verification metrics ME, MAE for 6 hour (06-12 UTC of November 30, 2024) accumulated rainfall calculated over different precipitation thresholds (>5, 10, 20, 30, 40 mm). Relative improvements (degradations) for median ME, median MAE, and IQR are annotated above the corresponding bars in green (red). The IQR relative improvements are annotated after the ME or MAE ones.

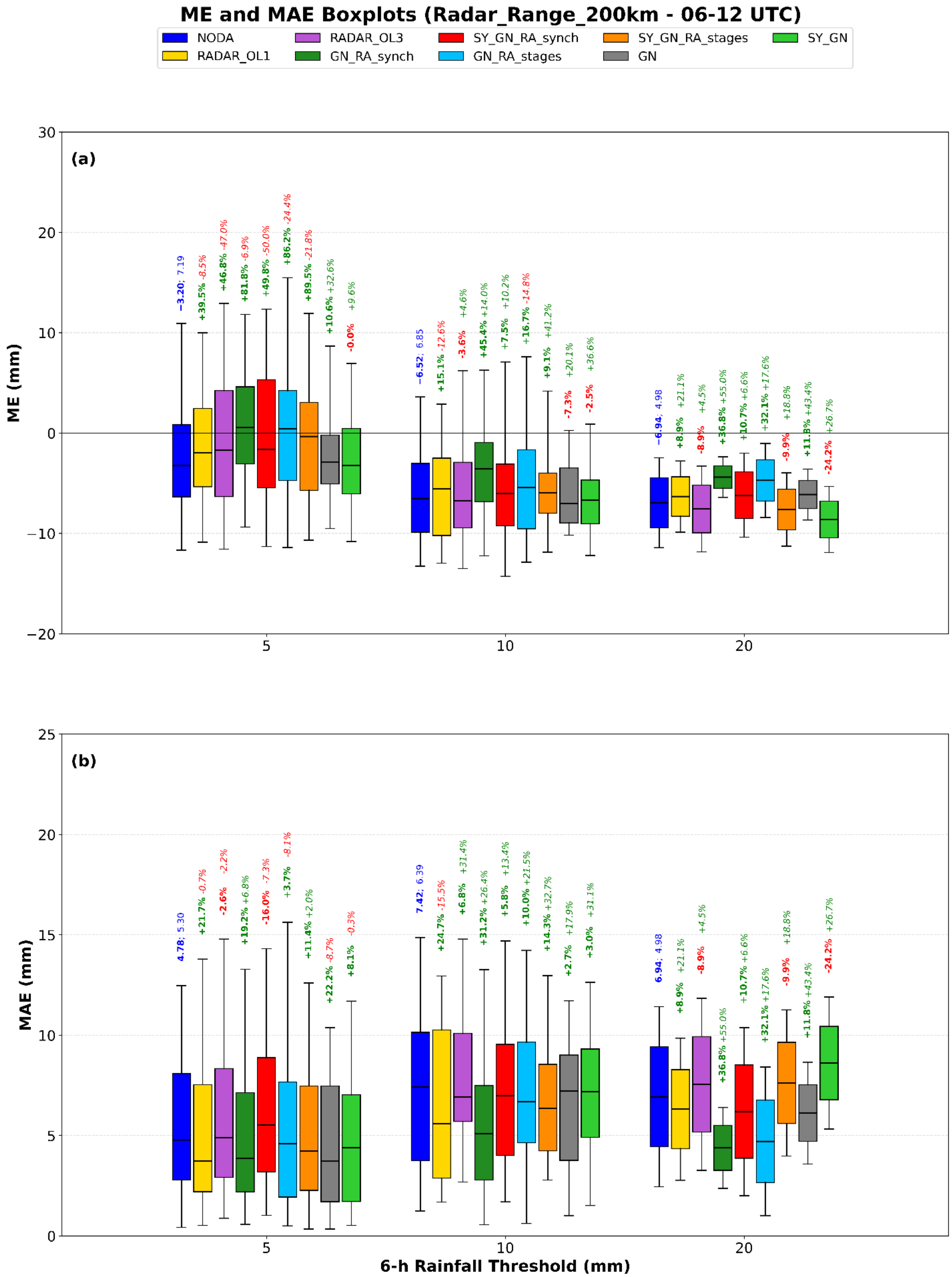

Fig. 7. The 200 km radius area around the Filyro radar site verification metrics ME, MAE for 6 hour (06-12 UTC of November 30, 2024) accumulated rainfall calculated over different precipitation thresholds (>5, 10, 20 mm). Relative improvements (degradations) for median ME, median MAE, and IQR are annotated above the corresponding bars in green (red). The IQR relative improvements are annotated after the ME or MAE ones.

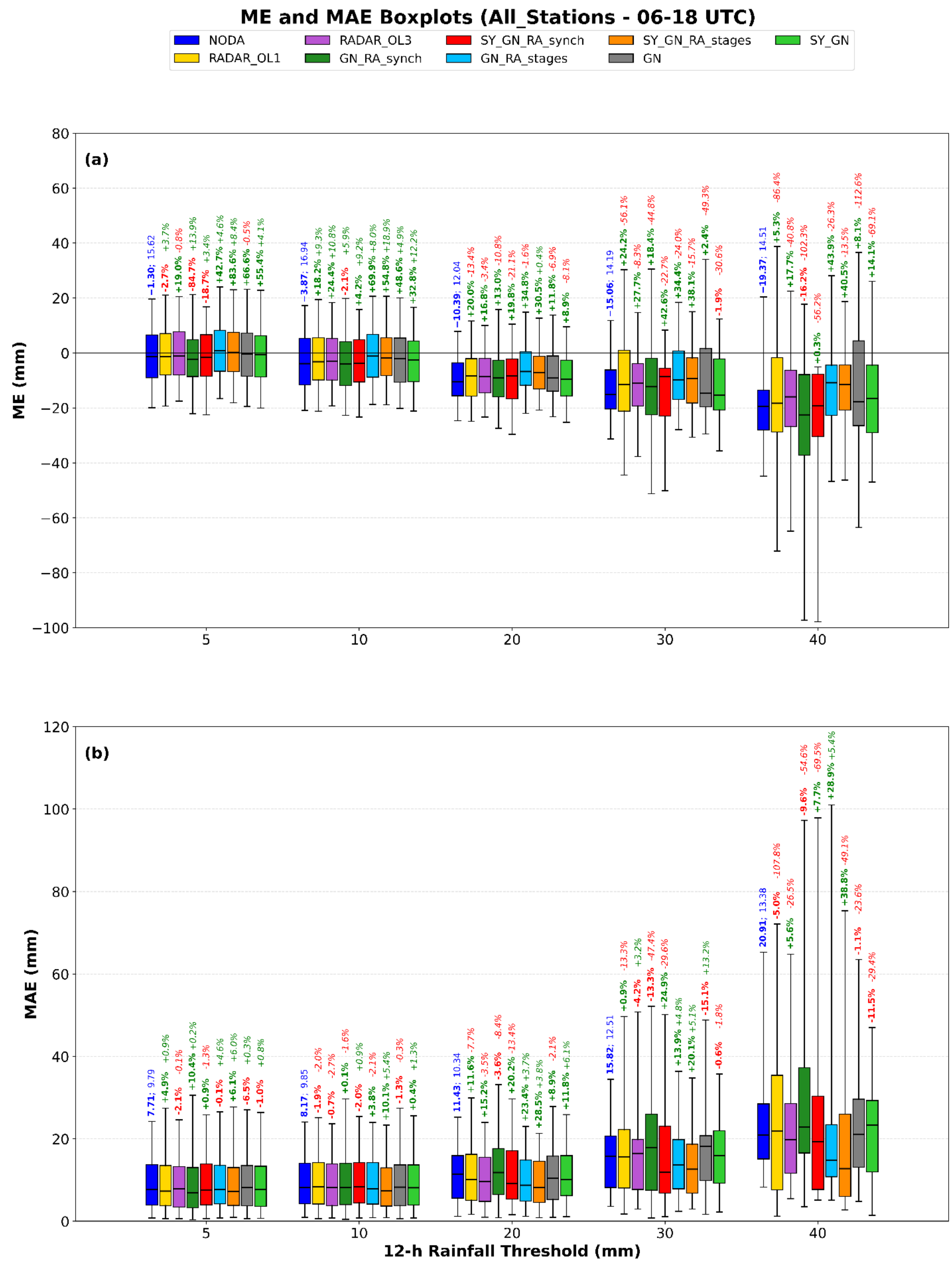

Fig. 8. The nationwide verification metrics ME, MAE for 12 hour (06-18 UTC of November 30, 2024) accumulated rainfall calculated over different precipitation thresholds (>5, 10, 20, 30, 40 mm). Relative improvements (degradations) for median ME, median MAE, and IQR are annotated above the corresponding bars in green (red). The IQR relative improvements are annotated after the ME or MAE ones.

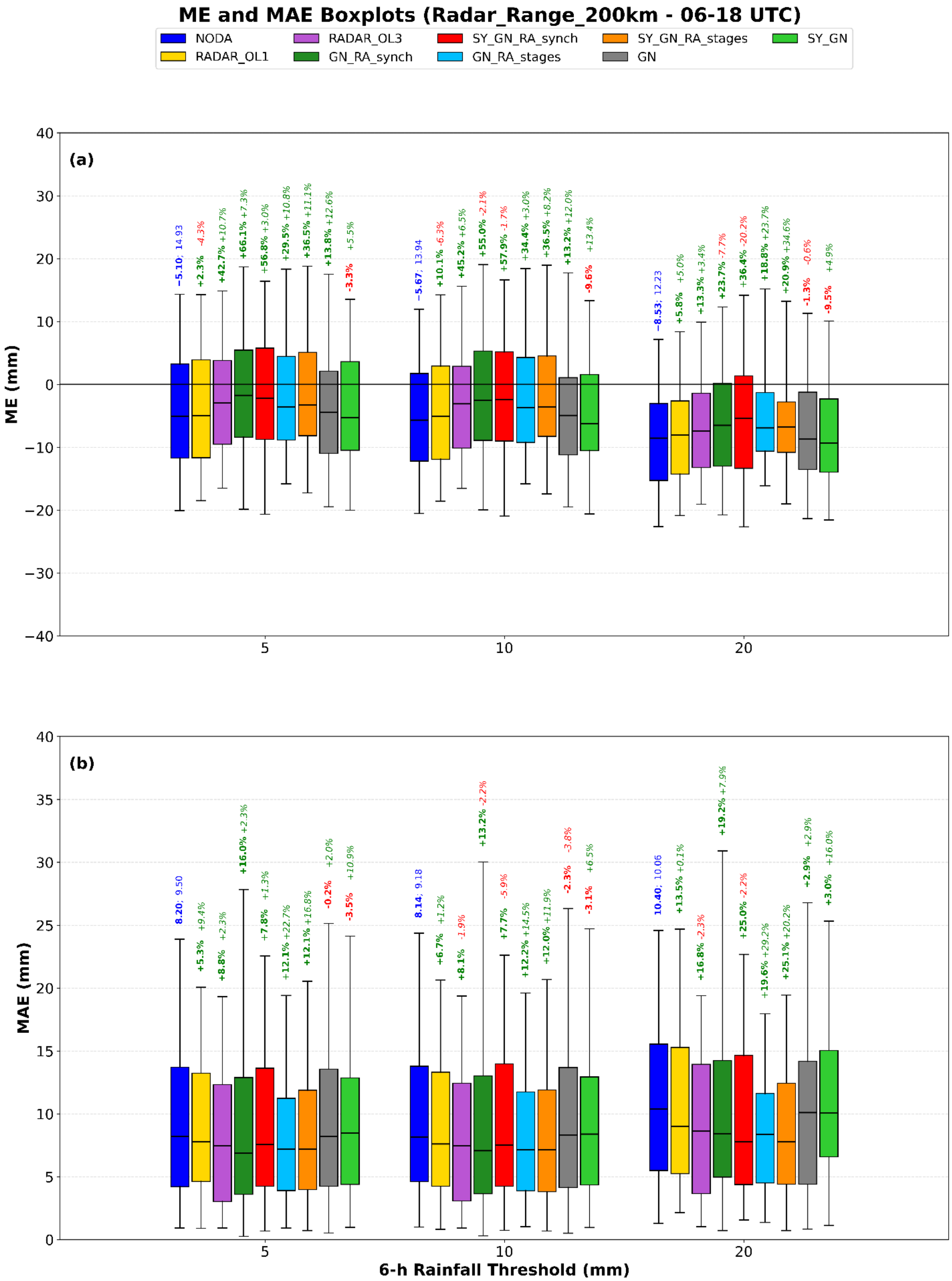

Fig. 9. The 200 km radius area around the Filyro radar site verification metrics ME, MAE for 12 hour (06-18 UTC of November 30, 2024) accumulated rainfall calculated over different precipitation thresholds (>5, 10, 20 mm). Relative improvements (degradations) for median ME, median MAE, and IQR are annotated above the corresponding bars in green (red). The IQR relative improvements are annotated after the ME or MAE ones.

In general, the CSI and the POD are higher when we consider the longer period, meaning that simulations in the long run capture better the spatial structure of the rainbands as the storm intensifies and expands throughout Greece (Figs. 2-5). Also, for the 12-hour period the FAR and the FBIAS are lower compared to the 6-hour period which shows that the 12-hour simulations reduce the overestimation of precipitation regions (Figs. 2c,d-5c,d). To determine which configuration consistently outperforms NODA across both spatial areas and verification windows, relative metric improvements were calculated ($\frac{\text{metric}_{\text{DA}}-\text{metric}_{\text{NODA}}}{\text{metric}_{\text{NODA}}}$ %; in Figs. 2–9, percentages in green and red colors show relative improvement or decline, respectively). Additionally, a simple ranking of high-performance occurrences is provided in the Supplement (Figs. S2 and S3) to highlight which simulation is better. Note that relative percentage changes become highly sensitive to small absolute differences when baseline NODA scores approach zero, particularly at high precipitation thresholds where hit counts are low; these cases are interpreted with caution below.

The SY_GN_RA_stages and GN_RA_stages experiments stand out as the most performant configurations overall. The GN_RA_stages performs exceptionally well across light-to-moderate accumulated precipitation thresholds (≥ 5 mm to ≥ 20 mm) for both 6-hour and 12-hour accumulation windows and in both spatial regions (Figs. 2–9). Specifically, GN_RA_stages yields the highest occurrence of relative CSI improvements compared to NODA (Fig. S2). Furthermore, its MAE distribution is consistently reduced compared to NODA across all thresholds, most notably it frequently yields the lowest precipitation underestimation for moderate to higher thresholds (≥20 up to ≥40 mm) compared to the other simulations (Figs. 6b-9b). More specifically, during the initial 6-hour period within the 200 km radar region, GN_RA_stages increases CSI by 41% (0.65 vs NODA 0.46) and 18% (0.18 vs NODA 0.15) relative to NODA for the light precipitation thresholds of ≥ 5 mm and ≥ 10 mm, respectively (Fig. 3a). This improvement is driven by 49% and 38% boosts in POD for these same thresholds without any significant degradation in FAR (Fig. 3b). Notably, for moderate precipitation in the radar area during the first 6 hours after the data assimilation, GN_RA_stages is the sole simulation to have a non-zero CSI (CSI=0.1) at the ≥ 20 mm threshold (Fig. 3a), though this reflects a very small number of exceedance events and should be interpreted as marginal rather than robust skill. This localized skill extends into the 12-hour window, where GN_RA_stages boosts radar-region CSI by 14%, 13%, and 38% across the ≥ 10 mm light threshold, the ≥ 15 mm and ≥ 20 mm moderate thresholds, respectively (Fig. 5a). Across the nationwide domain, GN_RA_stages similarly maintains superior skill over NODA across windows (6h: ≥ 5 mm CSI of 0.59 vs NODA 0.53 (Fig. 2a); 12h: ≥ 20 mm CSI of 0.3 vs NODA 0.23 (Fig. 4a)). Furthermore, in the error distribution boxplots, GN_RA_stages reduces median MAE at the ≥ 40 mm heavy threshold by 54% in the 6-hour window (13.39 mm vs NODA 29.29 mm (Fig. 6b)) and holds for almost all the thresholds lower ME magnitudes in the 12-hour window compared to the other simulations (Figs. 8a and 9a).

SY_GN_RA_stages exhibits clear advantages over GN_RA_stages in overall error reduction and heavy threshold performance (≥ 30 mm to ≥ 40 mm) across both spatial domains (Figs. 2–9). Over the 200 km radar domain during the 12-hour window, SY_GN_RA_stages achieves higher CSI at the heaviest threshold (0.27 vs 0.23 at ≥ 40 mm (Fig. 5a)) while keeping median MAE values low and comparable to GN_RA_stages across both spatial regions (Figs. 8b and 9b). Nationally within the initial 6-hour window, SY_GN_RA_stages yields lower median MAE across light-to-moderate thresholds (≥ 5 mm to ≥ 20 mm; e.g., 8.68 vs 11.26 at ≥ 20 mm (Fig. 6a)) and superior CSI at heavy thresholds (≥ 30 mm and ≥ 40 mm: 0.12 and 0.15 vs 0.07 and 0.09 (Fig. 2a)). Over the 12-hour window nationwide, SY_GN_RA_stages achieves the lowest median MAE overall at the ≥ 40 mm heavy threshold (12.8 vs GN_RA_stages 14.87 and NODA 20.91 (Fig. 8a)) alongside higher ≥ 30 mm CSI (0.22 vs GN_RA_stages 0.19 (Fig. 4a)). On the other hand, GN_RA_stages retains the upper hand in short-term radar-domain light precipitation skill (6h: ≥ 5 mm CSI of 0.65 vs 0.6 (Fig. 3a)) and nationwide 6-hour heavy rainfall MAE at ≥ 40 mm (13.39 vs 17.01 (Figure 6b)). Overall, these results highlight a distinct trade-off between the two runs. While GN_RA_stages delivers peak performance for immediate (6-hour), highly localized light-to-moderate precipitation events (≥ 5 mm to ≥ 20 mm) within the radar domain (Fig. 3), SY_GN_RA_stages provides broader value through superior nationwide error reduction (Figs. 6 and 8), persevering forecast skill out to the 12-hour window (Figs. 4, 5, 8, 9), and enhanced skill in capturing heavy rainfall (≥ 30 mm to ≥ 40 mm) across both spatial domains (Figs. 2, 4, 3, 5).

Across evaluation windows, the primary strength of GN lies in the 6-hour period nationwide delivering robust CSI enhancements across nearly all thresholds (Fig. 2a) alongside significant MAE reductions in the light-to-moderate regime (≥ 5 mm to ≥ 20 mm (Fig. 6b)) while maintaining selective localized strength at the moderate ≥ 20 mm threshold during the 12-hour window (Figs. 5a). Specifically, over the wider nationwide domain during the 6-hour window, GN outperforms NODA across light-to-moderate thresholds (≥ 5 mm to ≥ 15 mm), with nationwide CSI gains up to 12% (reaching 0.37 at ≥ 10 mm vs NODA 0.33 (Fig. 2a)). Within the 200 km radar domain across light thresholds (≥ 5 mm and ≥ 10 mm), CSI gains reach 20% (0.55 vs 0.46 and 0.18 vs 0.15, respectively (Fig. 3a)). For moderate-to-heavy rainfall (≥ 15 mm to ≥ 40 mm), GN achieves a nationwide ≥ 30 mm CSI of 0.12 (modest increase compared to the NODA score of 0.05), matching SY_GN_RA_stages (Fig. 2a)) and reduces ≥ 20 mm MAE to 11.5 (vs NODA 14.43, a 20% reduction (Fig. 6b)). MAE improvements are further highlighted by a 22% reduction (3.72 vs 4.78) for the light ≥ 5 mm precipitation threshold in the radar domain at 6h (Fig. 7b). Notably, marked localized enhancements persist into the 12-hour period within the 200 km radar domain, where GN achieves substantial CSI improvements at ≥ 20 mm (36%; 0.36 vs. 0.26) and ≥ 40 mm (33%; 0.31 vs 0.23, accompanied by a 13% MAE reduction) (Figs. 5b and 9b). Overall boxplot analysis shows that GN achieves an average 35% ME magnitude reduction across thresholds at 6 hours (Figs. 6a and 7a). However, the precipitation forecast skill of GN dissipates over the 12-hour period on the broader spatial scale: its nationwide ≥ 30 mm heavy CSI drops slightly below NODA (0.20 vs. 0.21 (Fig. 4a)), its 12-hour nationwide light ≥ 5 mm CSI drops to 0.72 (vs NODA 0.75 (Fig. 4a)), and average MAE accuracy drops by 3% below NODA (Fig. 8b).

It is worth noting that when the SYNOP measurements are combined with the GNSS PWV (SY_GN) then the nationwide relative improvement of CSI boosts compared to GN within the 6 hour period for ≥ 30 and ≥ 40 mm thresholds (Fig. 2a). MAE reductions are also greater compared to GN for the same examined region and time period (Fig. 6b).

Radar-only data assimilation simulations deliver strong short-term performance over the 6-hour window, particularly RADAR_OL3 across the nationwide domain (Figs. 2 and 6). Remarkably, both RADAR_OL1 and RADAR_OL3 sustain high skill over the extended 12-hour window across both the radar-focused and nationwide regions (Figs. 4, 5, 8, 9). Across light-to-moderate thresholds (≥ 5 mm to ≥ 20 mm), both configurations yield high CSI scores and low MAE values over 12 hours (Fig. 4a). More specifically, the RADAR_OL3 yields better CSI gains for these thresholds nationwide and within the radar range for both time windows for most of the times. RADAR_OL3 demonstrates even greater efficacy over 12 hours in the radar range achieving a 41% relative CSI increase at ≥ 20 mm (Fig. 5a) which is accompanied by a 17% MAE reduction. On the other hand, RADAR_OL1 manages to be better for the heavier threshold (≥ 30 and ≥ 40 mm) where the relative improvement of CSI are greater in both 6 and 12 hour window nationwide and within the radar range. More particularly, for the first 6 hours in the radar range the CSI is almost tripled for ≥ 30 mm (Fig. 2a) and for the 12 hour period for ≥ 40 mm the CSI relative increase is 11% and 33% increase for nationwide and radar range, respectively (Figs. 4a and 5a). Consequently, both radar-only configurations prove highly effective for short-term and extended lead times, with RADAR_OL1 standing out as a particularly effective configuration for moderate-to-heavy rainfall across regions (Figs. 2–9).

In contrast, the synchronous multi-stage configuration SY_GN_RA_synch delivers moderate categorical skill across evaluation windows, yet achieves substantial error reductions for moderate-to-heavy rainfall (≥ 20 mm to ≥ 40 mm) (Figs. 6–9). While its overall CSI performance remains limited, it achieves substantial MAE reductions for heavy accumulation events over the 12-h window (Figs. 8b and 9b). More precisely, SY_GN_RA_synch reduces median MAE by 45% at ≥ 30 mm (8.34 vs NODA 15.22) and by 27% at ≥ 40 mm (15.15 vs NODA 20.81) within the radar region (Fig. 9b), while maintaining nationwide 12-hour MAE reductions of 25% at ≥ 30 mm (11.89 vs NODA 15.82) and 20% at ≥ 20 mm (Fig. 8b).

In contrast, identifying the least performant assimilation configurations highlights the operational limitations of synchronous single-stage and non-radar assimilation strategies across different accumulation windows and spatial regions. During the initial 6-hour window, GN_RA_synch shows notable skill limitations among the assimilation experiments across both spatial areas (Figs. 2, 3, 6, 7). While it incorporates data assimilation, its synchronous formulation yields low categorical skill nationwide across light thresholds (6h CSI of 0.52 at ≥ 5 mm and 0.24 at ≥ 10 mm (Fig. 2a)), the highest 6-hour nationwide ≥ 5 mm false alarm ratio (FAR = 0.36; FBIAS =

1.16 (Figure 2c, d)), and zero skill at moderate-to-heavy thresholds above ≥ 20 mm in the 200 km radar footprint (CSI = 0.0 (Fig. 3a)). Furthermore, it produces the largest nationwide 6-hour median MAE at ≥ 40 mm (31.85 mm (Fig. 6b)). Over the extended 12-hour window, SY_GN and GN emerge as the weakest assimilation configurations (Figs. 4, 5, 8, 9). SY_GN records the highest nationwide 12-hour median MAE at ≥ 40 mm (23.32 mm (Fig. 8b)) and exhibits low skill at moderate-to-heavy thresholds nationwide (12h CSI of 0.22 at ≥ 20 mm and 0.19 at ≥ 30 mm (Fig. 4a)). Similarly, GN exhibits skill decay over the 12-hour time period with the nationwide ≥ 30 mm CSI dropping to 0.20 (Fig. 4a), and the radar-domain ≥ 5 mm CSI decreasing to 0.72 (Fig. 5a), resulting in larger mean errors at the ≥ 40 mm threshold nationwide (MAE = 21.14 mm (Fig. 8b)) over 12 hours.

3.2 From Increments to Dynamics: Explaining Simulation Deviations

3.2.1 Potential temperature and water vapor mixing ratio increments

In order to understand why the data assimilation simulations, lead to different precipitation patterns, the different combinations and data ingestion methods are examined. In particular, the potential temperature and water vapor mixing ratio increments ($\Delta x = x_{analysis} - x_{background}$) are calculated and depicted in Figures 10 and 11, respectively.

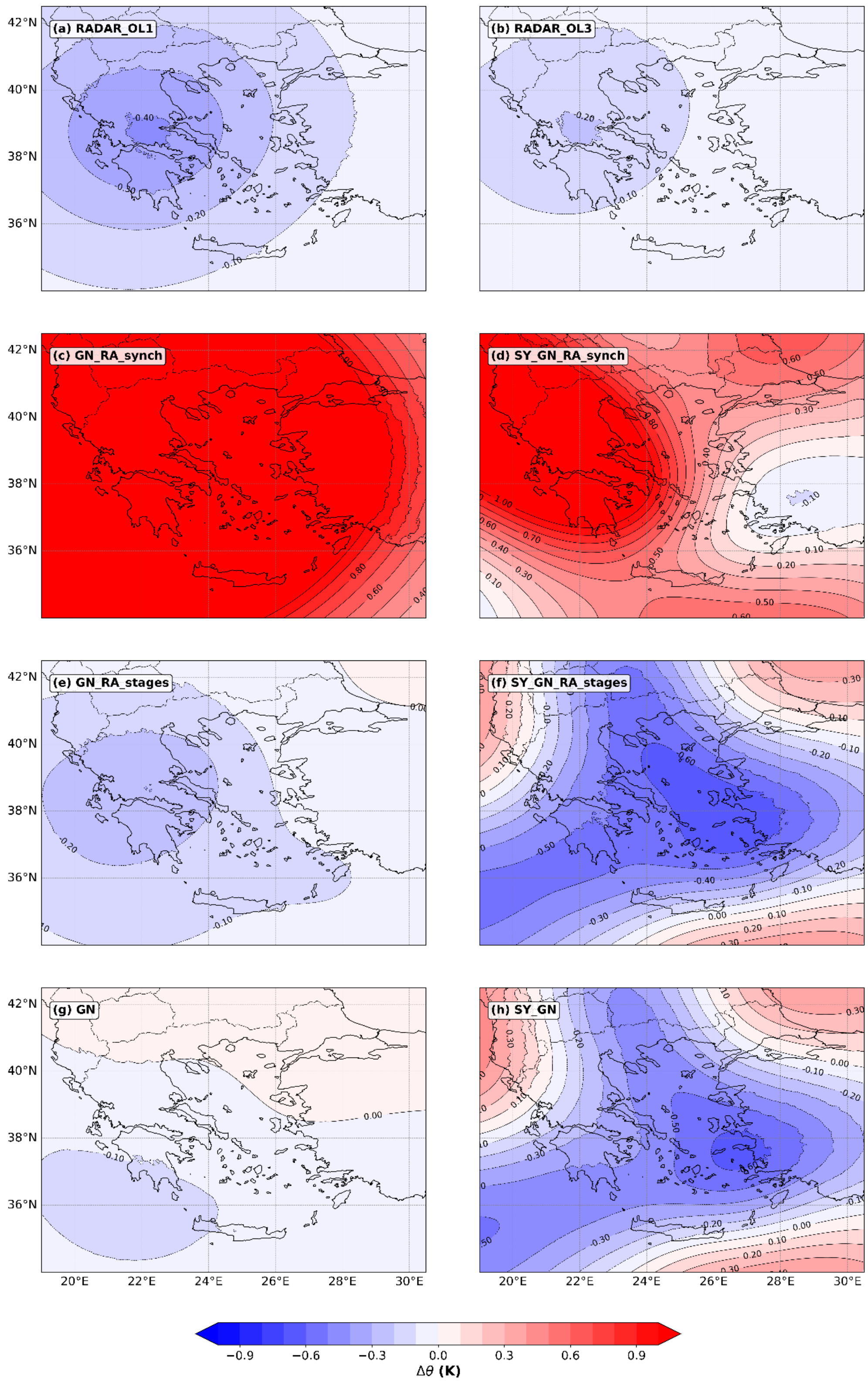

Figure 10. Potential temperature increments (Δθ [K]) calculated at 9th sigma model level (which corresponds roughly to 850 hPa level) for the RADAR_OL1, RADAR_OL3, GN_RA_synch, SY_GN_RA_synch, GN_RA_stages, SY_GN_RA_stages, GN, and SY_GN simulations. Contour lines are displayed at intervals of 0.10°C.

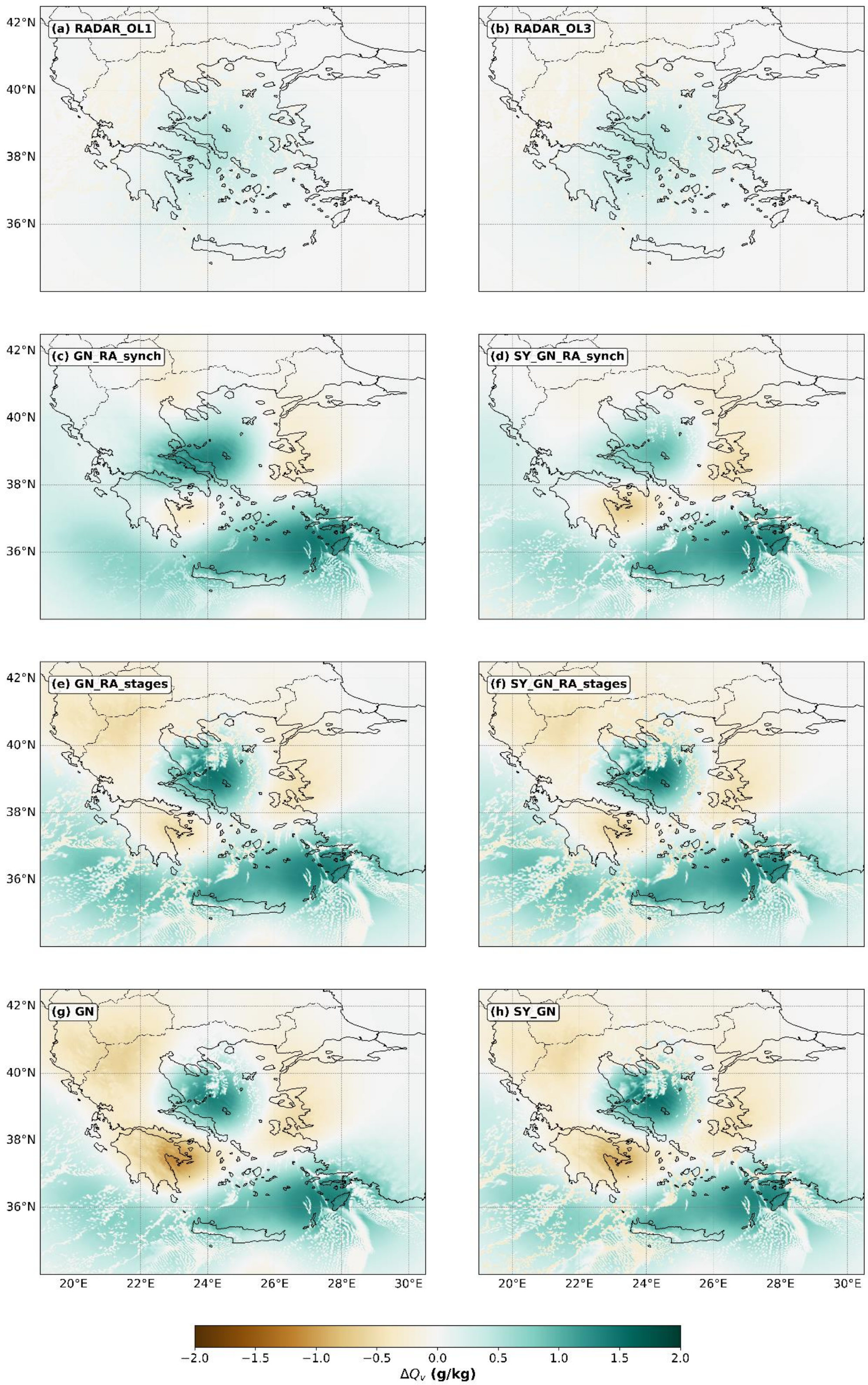

Figure 11. Water vapor mixing ratio increments (ΔQ_v [g kg^{-1}]) calculated at 9th sigma model level (which corresponds roughly to 850 hPa level) for the RADAR_OL1, RADAR_OL3, GN_RA_synch, SY_GN_RA_synch, GN_RA_stages, SY_GN_RA_stages, GN, and SY_GN simulations.

Radar reflectivity data assimilation produces a localized drop of potential temperature over central continental Greece, forming concentric regions of negative increments (Figs. 10a, b). This cooling effect is spatially broader and more intense in the 1-outer-loop configuration (RADAR_OL1) than in the 3-outer-loop configuration (RADAR_OL3). This difference could be attributed to the fact that the three-outer-loop setup presents higher flexibility to dynamically adjust the analysis toward the model's background state. The two radar assimilation simulations yield quite similar water vapor mixing ratio increments, characterized by a positive, increment at the center of the Greek domain and a contrasting drying effect across western and northern continental Greece (Figs. 11a, b). The localized cooling seen in Figs. 10a, b could be a direct consequence of the radar-detected increased cloud water over central continental Greece, which induces a temperature drop via simulated evaporative cooling. The drying effect at the center of the Greek domain (Figs. 11a, b) likely represents the system's balancing response to the clear-air (zero-echo) regions observed by the radar network.

In the GN simulation, the ingestion of precipitable water vapor (PWV) induces a strong, positive water vapor mixing ratio dipole over the Aegean Sea, with its centers located over the core of the Greek domain and the southeastern Aegean (Fig. 11g). This pattern indicates that GNSS observations successfully adjusted the moisture field transported into the domain. Furthermore, these moisture adjustments trigger organized zonal potential temperature increments—characterized by a warming trend from southwest to northeast Greece—to accommodate the relocated moisture dipole while maintaining the hydrostatic equilibrium of the atmosphere (Fig. 10g).

When radar reflectivity measurements and GNSS PWV are ingested simultaneously (GN_RA_synch), the resulting patterns of potential temperature and water vapor mixing ratio differ from single-source data assimilation. The positive water vapor increment dipole broadens, which effectively limits drying over continental Greece (Fig. 11c). This spatial expansion indicates that the high-resolution radar echoes reinforce the moisture plumes identified by the GNSS sensors. The most profound change manifests in the potential temperature increments (Fig. 10c). Here, the combined effect of radar and GNSS measurements lead to the injection of moisture and hydrometeors into the troposphere. This injection is accompanied by latent heat release, with the peak emission located over central Greece. Notably, this warming response contrasts with the net cooling produced when radar reflectivity is assimilated on its own. This thermal anomaly expands across the Greek region and slowly fades towards Turkey.

To fully understand the formation of the data assimilation increments in the SY_GN_RA_synch experiment, it is necessary to first isolate how the SYNOP observations modify the background state. The assimilation of SYNOP data generates a circular core of negative potential temperature increments centered in the eastern Aegean Sea. This low-level cooling pattern gradually expands along a southwest-to-northwest axis across the Aegean Sea (Fig. S2). Dynamically, this region acts as a key transport pathway where warm, moist air is advected towards northwestern Greece during the BORA storm. Concurrently, the water vapor mixing ratio increments exhibit a widespread, subtle drying effect over the entire Greek domain (Fig. S4). Hence, the SYNOP observations act to cool the warm sector of the surface low-pressure system while reducing ambient tropospheric moisture. Consequently, this suppresses the net heat and moisture transport within the lower troposphere over the Aegean Sea.

Fig. 10d also displays the potential temperature increments when all the available kinds of measurements are used synchronously (SY_GN_RA_synch). The dominant positive core over central continental Greece observed in the GN_RA_synch run is preserved. This signifies that the combined effect of radar reflectivity and GNSS PWV, which results in latent heat injection, is the primary dynamic driver. However, this warm anomaly fades progressively toward the Aegean Sea, where the positive increments weaken and veer northward over the Chalkidiki peninsula (southwestern Macedonia) and southward toward the coastal Peloponnese. This spatial shift encompasses the core of the BORA surface low, effectively sharpening the potential temperature gradient across the Aegean basin. In the moisture field (Fig. 11d), the characteristic water vapor mixing ratio dipole persists, yet its spatial extension is visibly constrained compared to the GN_RA_synch experiment. This is accompanied by a more pronounced drying effect over continental Greece, indicating that the SYNOP observations impose a spatial constraint.

In the SY_GN experiment, the resulting analysis increments reveal that SYNOP measurements dictate the thermal adjustment mechanisms, whereas the GNSS PWV controls the moisture ones. The potential temperature increment topology remains nearly identical to the SYNOP, characterized by low-level cooling over the Aegean basin (Fig. 10h). The only discernible variation is a slight spatial narrowing of the -0.4 K contour corridor passing between the southern Peloponnese and western Crete. This preservation of the thermal structure indicates that while GNSS PWV strongly influences the column moisture, it exerts negligible direct effect on the atmospheric thermal fields when combined with SYNOP observations. Conversely, the water vapor mixing ratio increments retain the dipole signature characteristic of GNSS-driven runs (Fig. 11h). This demonstrates that deep-column PWV observations effectively override the localized surface drying constraints imposed by SYNOP stations. This outcome contrasts with SY_GN_RA_synch, where the addition of radar reflectivity alongside SYNOP and GNSS led to a less spatially confined moisture dipole.

In GN_RA_stages, the positive potential temperature increments seen in the synchronous GN_RA_synch configuration vanish and are entirely superseded by a broad negative increment core over central Greece (Fig. 10e), which is an opposite thermal response to that produced when the same two observation types (GNSS PWV and radar reflectivity) are ingested simultaneously. This suggests that the order in which observations are assimilated, and not only their content, plays a role in determining whether the combined moisture and hydrometeor information is resolved as a warming (latent-heat-release) or cooling (evaporative) signal. The moisture injected into the atmosphere from the ingested GNSS PWV measurements during the first stage pre-conditions the background, leading to enhanced evaporative cooling when radar echoes are introduced over central continental Greece in the second stage. The characteristic water vapor mixing ratio increment dipole persists in the final analysis but is spatially broadened by the radar data compared to GN (Fig. 11e). Consequently, because the radar reflectivity is assimilated into a moisture-corrected background, it alters the initial zonal temperature increments into an expansive circular pattern that originates over central Greece and extends across the Aegean Sea to encompass the positive moisture dipole.

The potential temperature and water vapor mixing ratio increments for the final two-stage sequential configuration (SY_GN_RA_stages), where a combined SYNOP-GNSS analysis is utilized as the background for a subsequent radar reflectivity ingestion is also illustrated in Figs. 10f and 11f. Remarkably, the final potential temperature increment topology reverts to a pattern closely resembling the SYNOP, completely absorbing the localized mainland thermal anomalies seen in previous radar-inclusive runs. This complete shift demonstrates that establishing a robust, hydrostatically balanced synoptic mass field in the first stage prevents the subsequent radar cloud analysis from inducing localized potential temperature increments. Instead, the primary modification is a pronounced spatial expansion of the main circular cooling core northward into the Northern Aegean Sea. Concurrently, the water vapor mixing ratio increments preserve the characteristic marine moisture dipole, maintaining reduced drying over continental Greece. This indicates that pre-conditioning the deep-column moisture and surface mass fields simultaneously in the first stage constrains the radar's echoes responses and preserving a stable, horizontally diffuse moisture structure prior to model integration.

3.2.2 Impact of Assimilation Increments on Geopotential Height and Low-Level Thermodynamic Transport

The aforementioned variations in potential temperature and mixing ratio increments directly alter the structural characteristics of the surface low-pressure system. For this reason, the geopotential height patterns at 850 hPa are examined, aiming to reveal the different dynamics that emerge from the various experiments (Fig. 12). Red contours are overlaid on each data assimilation figure to clearly highlight the structural modifications within this key region. White areas denote regions where mountainous terrain penetrates the 850 hPa plane. Also, the 500 hPa charts for the geopotential height are displayed in Fig. S5 for completeness.

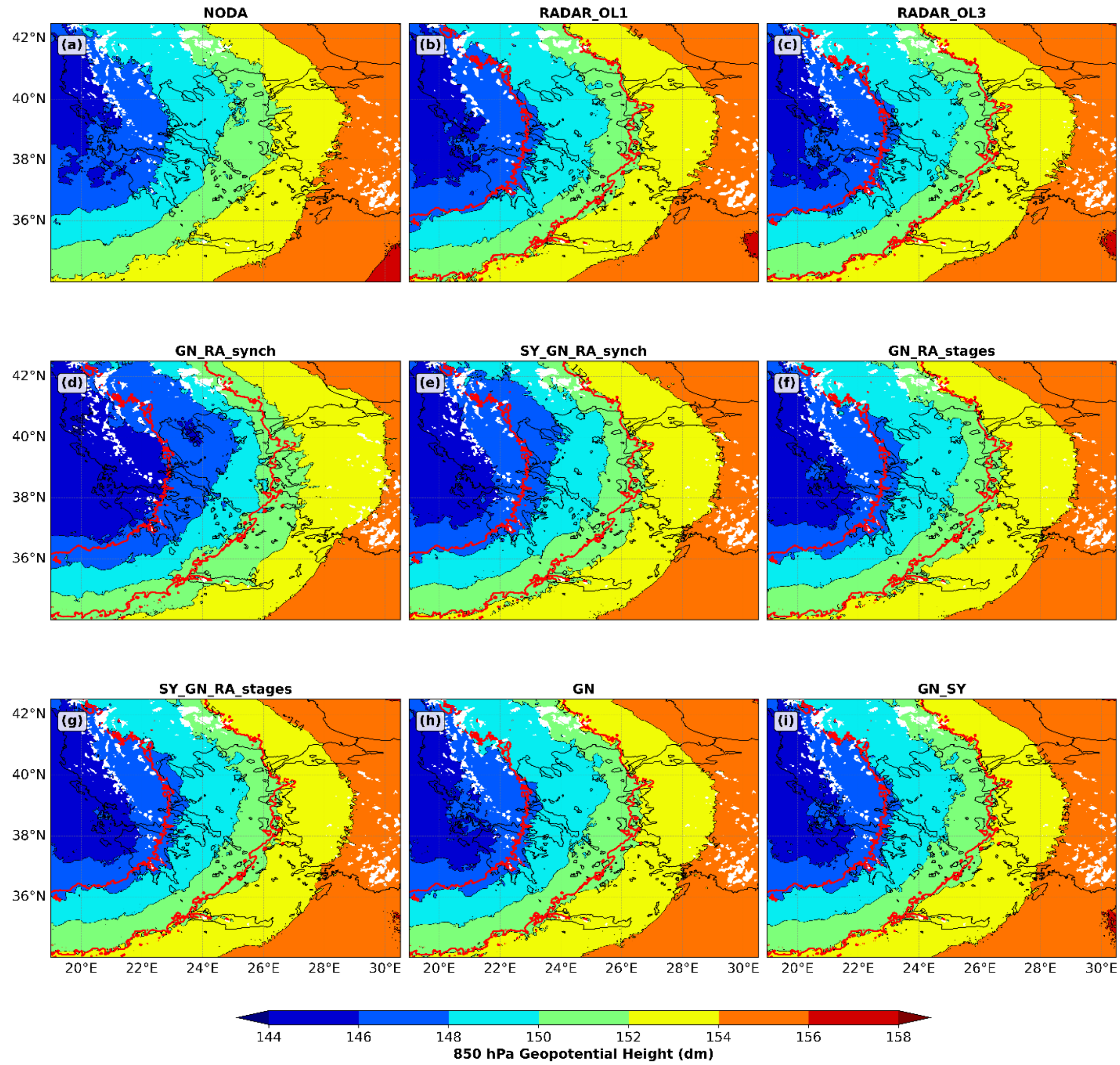

Fig. 12. Geopotential height at 850 hPa for NODA (a), RADAR_OL1 (b), RADAR_OL3 (c), GN_RA_synch (d), SY_GN_RA_synch (e), GN_RA_stages (f), SY_GN_RA_stages (g), GN (h), and SY_GN (i) simulations. Contours are plotted every 2 dm (solid lines). For reference, the 148 and 152 dm contours from the NODA simulation are overlaid as red contours across all data assimilation experiments.

Particular focus is placed over the Aegean Sea, where highly humid and warm air is transported from the southwestern sector of the cyclone towards northern Greece (Figs. 13 and 14). To emphasize how the changes in the geopotential height causes different dynamics, the integrated horizontal transport of sensible heat and water vapor flux from the surface up to about 700 hPa (12^{th} model eta level) at 09 UTC is shown. More precisely, the Integrated horizontal Vapor Transport (IVT, kg m^{-1} s^{-1}) and Integrated horizontal Sensible Heat Transport (IHT, W m^{-1}) are calculated as:

$$\mathrm{IVT} = \frac{1}{g}\int_{p_{sfc}}^{p_{700\ hPa}} \mathrm{qv}\, \mathrm{V}\, dp, \tag{4}$$

$$\mathrm{IHT} = \frac{C_p}{g}\int_{p_{sfc}}^{p_{700\ hPa}} \mathrm{T}\, \mathrm{V}\, dp, \tag{5}$$

where g is the gravity acceleration ($9.81\ \mathrm{m\ s^{-2}}$), qv is the water vapor mixing ratio ($\mathrm{kg\ kg^{-1}}$), C_p is the specific heat capacity of dry air at constant pressure ($1004.0\ \mathrm{J\ kg^{-1}\ K^{-1}}$), $V = (u, v)$ is the horizontal wind vector ($\mathrm{m\ s^{-1}}$), and T is the absolute temperature (K). To physically interpret the mechanisms driving differences in precipitation across the nine simulations, the IHT and IVT are analyzed at 09:00 UTC which is 3 hours after the data assimilation. This time selection allows sufficient model spin-up after the observation ingestion while the forecast differences begin to emerge and become distinguishable.

Integrated Heat Transport & Assimilation Anomalies

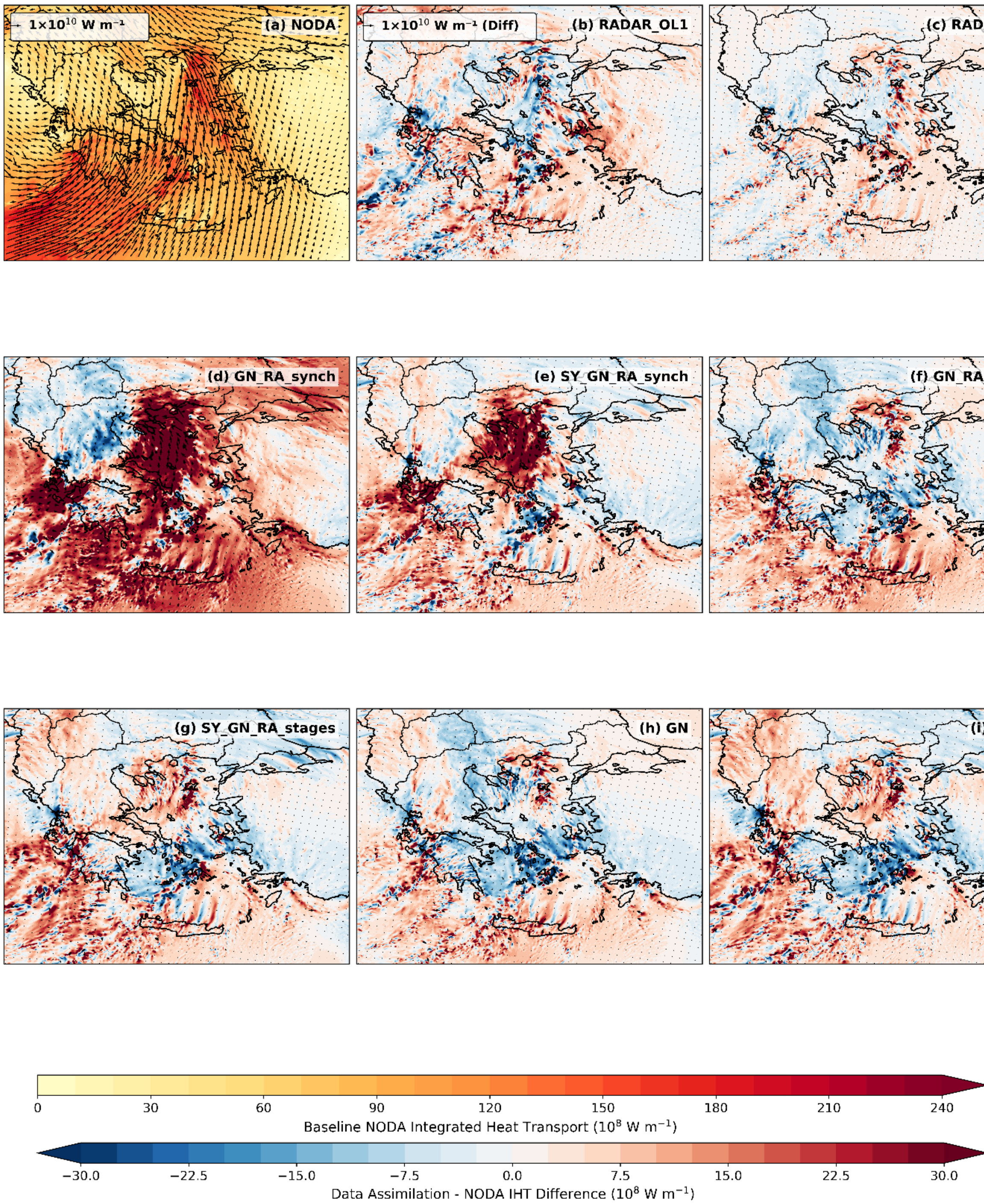

Figure 13. Vertically integrated (surface to ~700 hPa) horizontal sensible heat flux at 09 UTC for the NODA baseline simulation (a), followed by the respective difference fields between each data assimilation experiment and NODA (b-i). The subsequent figures in the panel display the anomalies relative to NODA for RADAR_OL1 (b), RADAR_OL3 (c), GN_RA_synch (d), SY_GN_RA_synch (e), GN_RA_stages (f), SY_GN_RA_stages (g), GN (h), and SY_GN (i), respectively. Two reference arrows with their numeric value in the a, b figures of the panel indicate the magnitude of the horizontal transport and horizontal transport differences between the da simulations and NODA.

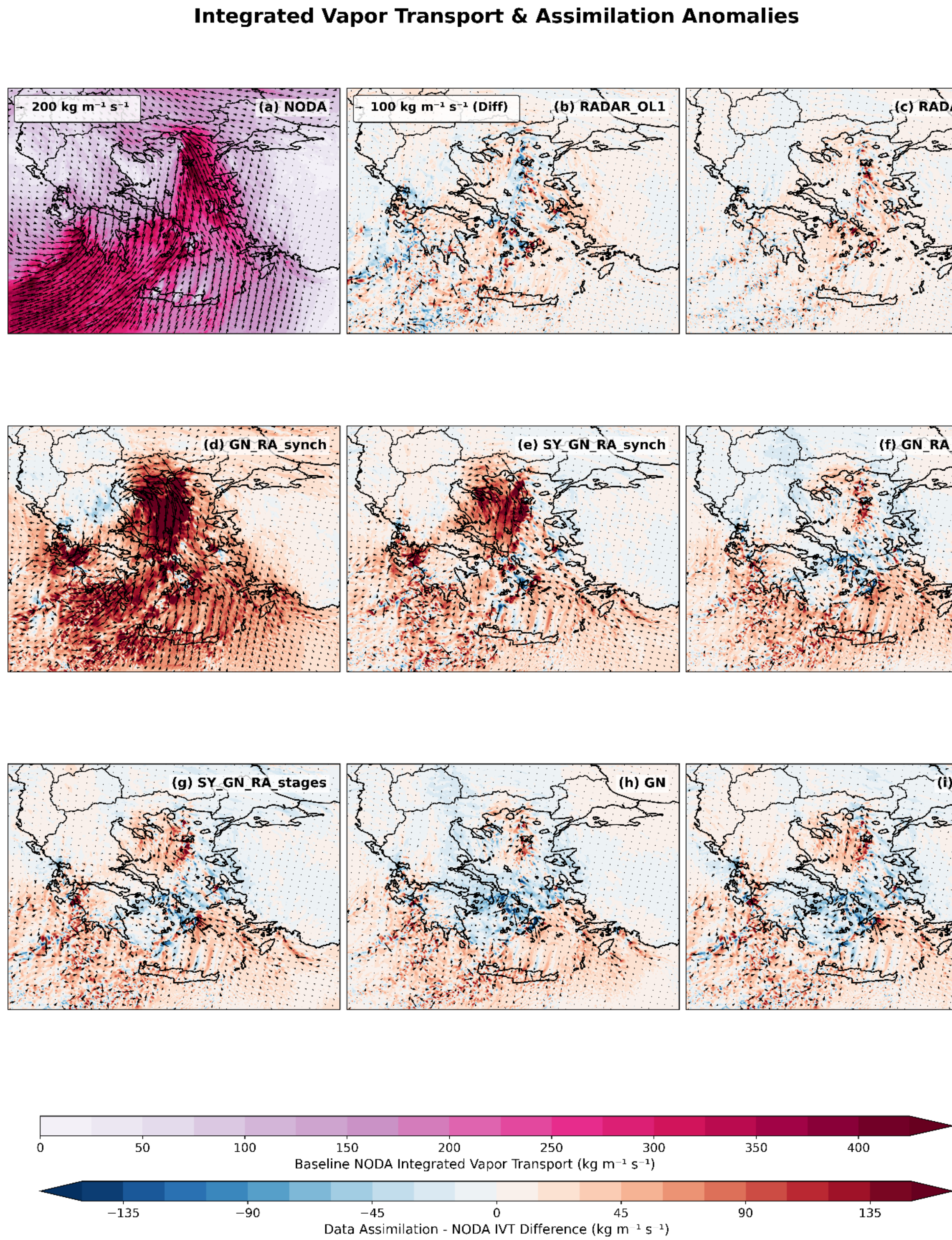

Figure 14. Vertically integrated (surface to ~700 hPa) horizontal water vapor mixing ratio flux at 09 UTC for the NODA baseline simulation (a), followed by the respective difference fields between each data assimilation experiment and NODA (b-i). The subsequent figures in the panel display the anomalies relative to NODA for RADAR_OL1 (b), RADAR_OL3 (c), GN_RA_synch (d), SY_GN_RA_synch (e), GN_RA_stages (f), SY_GN_RA_stages (g), GN (h), and SY_GN (i), respectively. Two reference arrows with their numeric value in the a, b figures of the panel indicate the magnitude of the horizontal transport and horizontal transport differences between the da simulations and NODA.

Figs. 12a, b indicate that the geopotential height contours in RADAR_OL1 and RADAR_OL3 expand eastward, particularly across the central Aegean Sea. In both simulations, the spacing between the 148 and 150 dm contours widens, whereas the interval between the 150 and 152 dm contours contracts, compared to the NODA experiment. This tightening is slightly greater in RADAR_OL3. Consequently, RADAR_OL1 induces an eastward shift of the horizontal heat and moisture fluxes around Lemnos Island (northeastern Aegean) relative to NODA (Figures 13a, b and 14a, b). Simultaneously, enhanced transport is directed over the central and western Aegean Sea, the marine basin north of Crete, and central continental Greece. Conversely, RADAR_OL3 yields smaller anomalies across most of the domain, except near Lemnos, where an influx originating from the southwest drives a more pronounced transport of heat and moisture than in RADAR_OL1.

The eastward expansion of the geopotential height contours reaches its maximum extent in GN_RA_synch and SY_GN_RA_synch (Figs. 12d, e). Specifically, in GN_RA_synch, the 146 dm contour displaces so far eastward that it nearly aligns with the baseline 148 dm position from the NODA run. Given the synoptic importance of the Aegean marine basin, we examine the geopotential gradient bounded by the 146, 148, and 150 dm contours along a latitudinal cross-section spanning from the Attica region to Lemnos Island. Near the latitude of Lemnos, the spacing between the 148 and 150 dm contours contracts relative to its width over Attica. This tighter gradient is further reinforced by a localized 146 dm low-height anomaly that develops over central Chalkidiki, effectively narrowing the low-level flow from the central to the northern Aegean (Fig. 12d). Consequently, an intense northward transport of heat and moisture is channeled across the Aegean before veering westward over northern continental Greece (Figs. 13d and 14d). Furthermore, thermodynamic fluxes within this corridor, across the wider Aegean basin, along the transport pathway extending from the southeastern Peloponnese to the island of Crete, and along the western coast of Greece are significantly enhanced relative to the NODA baseline.

A similar structural tightening occurs in SY_GN_RA_synch, where both the 148–150 dm and 150–152 dm contour intervals narrow at the Lemnos latitude (Fig. 12e); meanwhile, at the latitude of eastern Central Greece, the entire 148–152 dm corridor contracts compared to NODA. The resulting horizontal transport of heat and moisture exhibits a similar spatial pattern to GN_RA_synch, though with a smaller flux magnitude (Figs. 13e and 14e). Additionally, the heat and moisture transport anomalies are attenuated compared to GN_RA_synch over the northern Peloponnese and northwestern continental Greece.

In both GN_RA_stages and SY_GN_RA_stages, the 148–150 dm and 150–152 dm contour spacings contract relative to NODA along the Lemnos Island and Attica latitudinal cross-sections, with the latter synoptic-staged run exhibiting a slightly narrower corridor across the Aegean Sea (Figs. 12f, g). Evaluating the radial horizontal gradient of the 148–152 dm contours extending outward from the cyclonic core reveals that this radial distance is shortened in both sequential experiments, though it is least contracted when only the GNSS PWV observations are assimilated (GN_RA_stages). Consequently, horizontal heat and moisture fluxes intensify south of Lemnos in both simulations (Figs. 13f, g and 13f, g). Notably, these thermodynamic transports veer more vigorously westward over northern continental Greece in GN_RA_stages, whereas they expand further across the Northern Aegean in SY_GN_RA_stages. Furthermore, while the southern coast of the Peloponnese, the western Greek coastline, the northern marine basin of Crete, and the southeastern Aegean all experience enhanced heat and moisture transport compared to NODA, the magnitude of these flux anomalies is significantly smaller when the SYNOP observations are deployed.

When evaluating GN and SY_GN, the previously examined contour spacings (148-152 dm) are wider than those observed in the sequential data assimilation experiments (Figs 12f, g, h, i). Additionally, while the radial horizontal distance of the 148–152 dm contours outward from the cyclone core is shorter than the NODA baseline in both runs, it remains more expanded than in their sequential counterparts. Across both experimental setups (GN, SY_GN (standalone) and GN_RA_stages, SY_GN_RA_stages (sequential)), utilizing from the conventional measurements only the GNSS PWV measurements yield consistently a greater expansion of this radial distance alongside a slightly narrower latitudinal corridor over the Aegean Sea. Consequently, the horizontal heat and moisture transport in the GN simulation is primarily channeled along a longitudinal axis intersecting Lemnos Island, before undergoing a more pronounced westward cyclonic veering over northern Greece (Figs. 13h and 14h). Conversely, the SY_GN simulation exhibits less pronounced westward veering over northern Greece, with the thermodynamic flux expanding more broadly across the Northern Aegean (Figs. 13i and 14i). Furthermore, while both simulations capture enhanced heat and moisture transport over the southwestern Aegean, the Crete region, and the southwestern coast of Greece, the intensity of these fluxes is attenuated in SY_GN relative to GN. Instead, the SY_GN run concentrates a higher volume of heat and moisture transport over southwestern continental Greece compared to the standalone GNSS configuration.

3.2.3 Spatial Verification of Precipitation Forecasts and Impact of Data Assimilation

To contextualize the spatial verification of the data assimilation experiments, the underlying synoptic circulation pathways and the resulting rainband distribution of the Bora Storm must first be established. Although absolute ground truth of the storm's full spatial structure is unavailable, the general precipitation patterns can be reasonably characterized using a combination of superobed rain gauge observations and the baseline forecast. As reflected in these observations and circulation charts, the precipitation structure during the initial 6-hour window (06–12 UTC) is governed by distinct maritime and continental moisture streams (Figs. S6 and S7).

The primary maritime inflow originates from southern maritime Greece (southern maritime inflow), which feeds moisture directly from southwestern to southeastern maritime Greece and affects the precipitation over Crete and Rhodes Islands. From there, this marine inflow splits into two distinct paths: a western corridor that channels moisture through the Central Aegean Sea, and an eastern path that passes along central coastal Turkey. These two paths subsequently merge into a single, primary inflow toward northeastern continental Greece, forming the eastern marine branch that directly impacts Lemnos Island and the adjacent northeastern continental coastline.

Concurrently, a secondary stream wraps cyclonically around the northern and western flanks of the Bora low-pressure core to form the western continental branch, driving moist air over the central west coast of Greece and into central continental Greece.

As the storm proceeds into the 12-hour window (06–18 UTC), these pathways extend and mature (Figs. S7 and S8); the eastern marine branch veers to the west, severely impacting central and eastern Chalkidiki, while the western continental branch moves southwards and merges with the eastern marine branch. This interaction enhances and broadens moisture transport toward the western Aegean and the broader Thessaloniki region.

Figs. 15 and 16 compare the 6-hour and 12-hour accumulated precipitation derived from observations and simulations. To ensure a concise comparison, the observation locations derived from superobing correspond to the exact locations of the simulated rainfall. In these figures, locations are depicted as spots color-coded by rainfall magnitude and precipitation differences between the simulations and the observations. Larger spots highlight significant discrepancies.

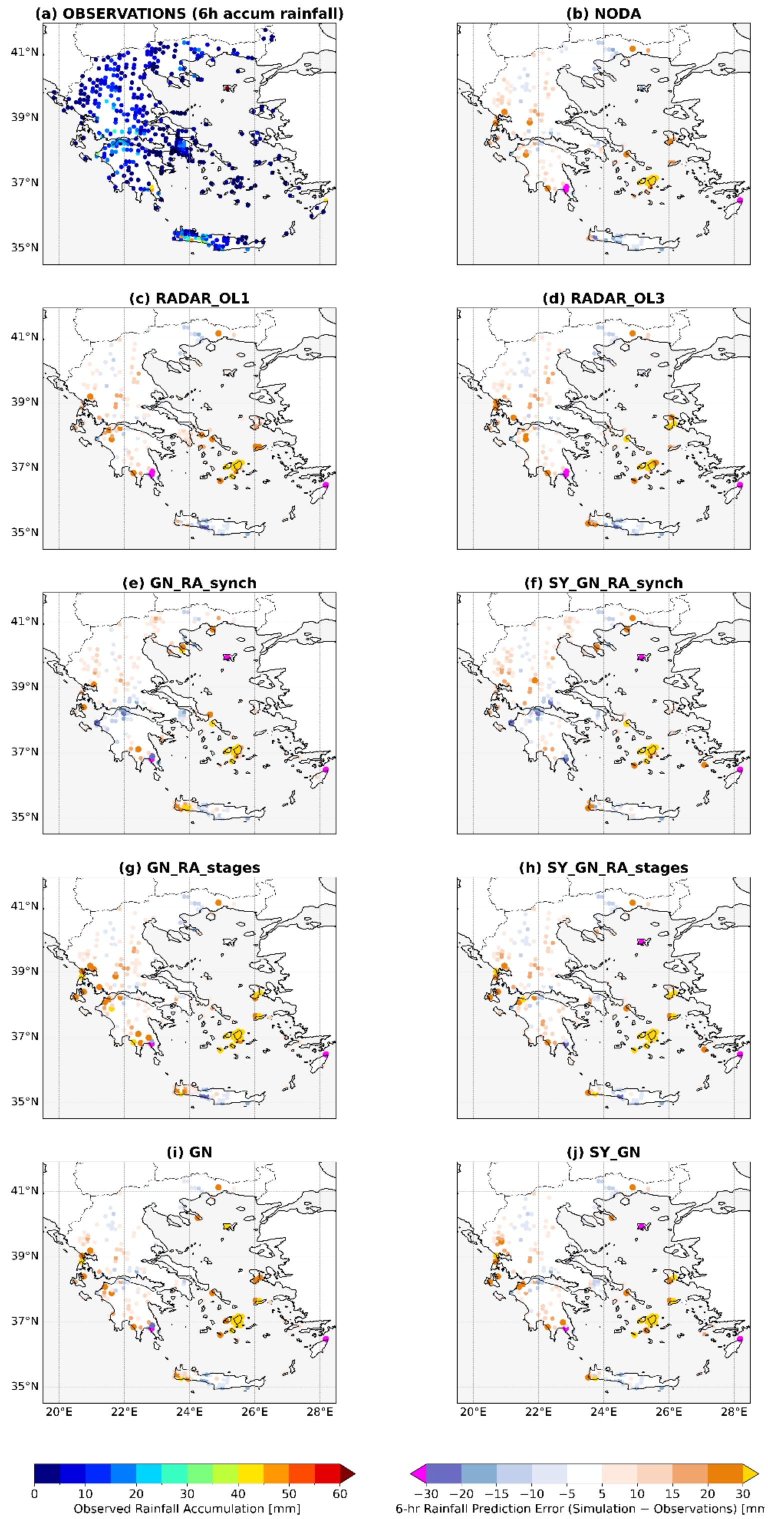

Figure 10. Spatial distribution of 6-hour accumulated rainfall (06:00–12:00 UTC on November 30, 2024). Top-Left Figure (a): Superobbed rain gauge observations (mm). Remaining Panels (b-j): Rainfall differences (mm) calculated as the simulation minus the observations. The plots display the baseline simulation and data assimilation experiments in the following order: NODA (b), RADAR_OL1 (c), RADAR_OL3 (d), GN_RA_synch (e), SY_GN_RA_synch (f), GN_RA_stages (g), SY_GN_RA_stages (h), GN (i), and SY_GN (j).

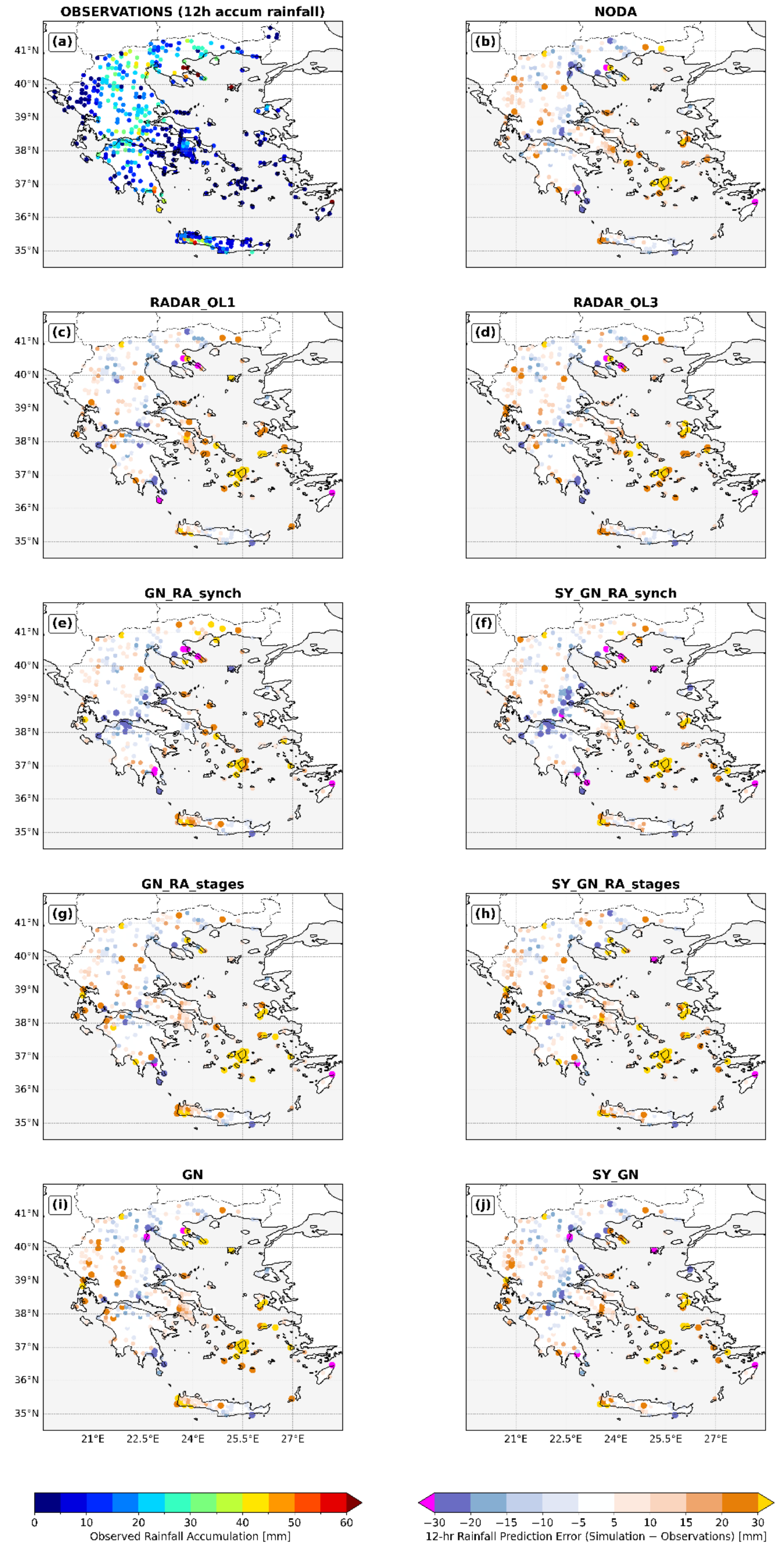

Figure 16. Spatial distribution of 12-hour accumulated rainfall (06:00–18:00 UTC on November 30, 2024). Top-Left Figure (a): Superobed rain gauge observations (mm). Remaining Panels (b-j): Rainfall differences (mm) calculated as the simulation minus the observations. The plots display the baseline simulation and data assimilation experiments in the following order: NODA (b), RADAR_OL1 (c), RADAR_OL3 (d), GN_RA_synch (e), SY_GN_RA_synch (f), GN_RA_stages (g), SY_GN_RA_stages (h), GN (i), and SY_GN (j).

3.2.3.1 The eastern maritime and western continental branches

The NODA experiment systematically underestimates the 6- and 12-hour accumulated rainfall over Lemnos (Figs. 15b and 16b). In addition, Fig. 16b shows that the precipitation is misplaced over the Chalkidiki region and underestimated along the western coast of Thrace (Kavala area). Furthermore, the 12-hour accumulated rainfall is overestimated across central continental Greece (Thessaly and Epirus) while being underestimated over Thessaloniki and the region to its northwest. Finally, NODA fails to capture the precipitation over Rhodes Island during the 12-hour period, producing a pronounced dry bias with little to no accumulated rainfall. Consequently, the moisture transport branches are incorrectly positioned; the effects of data assimilation in rectifying them are discussed below.

In RADAR_OL1 and RADAR_OL3, evaporative cooling from the ingested radar echoes leads to an eastward expansion of the 148, 150, and 152 dm geopotential height contours (Figs. 12b, c). Consequently, horizontal heat and moisture transport is channeled toward Lemnos Island (Figs. 13b, c and 14b, c), directing the eastern marine branch over the island and yielding accurate precipitation forecasts for the area during the 6 hour period (Figs. 15c, d). However, as this concentrated thermodynamic transport persists, it leads to an overestimation of the 12 hour accumulated precipitation over the island (Figs. 16c, d). Additionally, due to greater cyclonic veering of moisture transport (Figs. S9 and S10), the underestimation of 12-hour precipitation over the Kavala area remains; nevertheless, both simulations capture the rainfall over the Thessaloniki area and central continental Greece (Figs. 15c, d and 16c, d). Finally, the radar simulations fail to capture the rainfall over Rhodes Island; because this region lies deep within the southeastern Aegean—far beyond the effective scanning range of the continental radar network—it remains observationally unconstrained.

The synchronous simulations (GN_RA_synch and SY_GN_RA_synch) fail to capture the 6 and 12 hour accumulated rainfall over Lemnos Island. This is caused by an intense eastward expansion of the 146 and 148 dm geopotential height contours over central Chalkidiki at 850 hPa (Figs. 12d, e), which prematurely steers and broadens the eastern marine branch westward (Fig. S11). Consequently, horizontal maritime heat and moisture transport are enhanced west of Lemnos (Figs. 13d, e and 14d, e), driving an abrupt moisture veering over northeastern continental Greece (Figs. S12, S13). This leads to an overestimation of 6-hour rainfall over southern Chalkidiki and Thasos Island (Figs. 15e, f). As the moisture transport advances further inland during the 12-hour period, precipitation remains underestimated over Lemnos and central Chalkidiki while being overestimated across western coastal Thrace (Kavala area) and north of the Chalkidiki peninsula (Figs. 16e, f). Furthermore, the synchronous runs underestimate 6 and 12 hour rainfall over the northern Peloponnese and central Sterea Ellada (Figs. 15e, f and 16e, f) despite sustained and expanded moisture transport along the western continental branch (Figs. S10, S11). This underestimation is attributed to a northward displacement of the low-pressure center. The more northerly track straightens the flow along the western branch, causing the moist airstream to pass the coast with reduced turning and weaker low-level moisture convergence. In contrast, the remaining data assimilation experiments position the cyclone core further south, which increases cyclonic turning over the Ionian Sea and concentrates low-level moisture convergence along the western coast of Greece (Figs. S9, S10, S13-17).

The sequential simulations (GN_RA_stages and SY_GN_RA_stages) yield a narrower 148–152 dm geopotential height passage over the Aegean Sea (Figs. 12f, g), forcing low-level thermodynamic transport to intensify south of Lemnos Island (Figs. 13f, g and 14f, g). Within this sequential pair, however, the absence of surface constraints in GN_RA_stages allows the 850 hPa geopotential height contours to form a wider path over the central Aegean Sea. This structural configuration is counterbalanced by a more pronounced radial contraction and vigorous cyclonic veering of the contours directly over northern continental Greece relative to SY_GN_RA_stages. Consequently, greater horizontal heat and moisture transport affects Lemnos Island initially, closely aligning with observations during the first 6 hours (Fig. 15g) before shifting westward into eastern Chalkidiki by 12 hours, where it causes an overestimation of precipitation (Fig. 16g). In contrast, in SY_GN_RA_stages, advected heat and moisture transport expands broadly across the northern Aegean basin. This steers the eastern marine branch westward (Figs. 13g and 14g), underestimating rainfall over Lemnos while directing excess moisture into central and eastern Chalkidiki, resulting in an overestimation of precipitation (Figs. 15g, i and 16g, i). Meanwhile, both simulations yield greater precipitation along the central west coast of Greece compared to NODA across both time windows, though a detailed analysis of this region is omitted here.

In the GN simulation, omitting surface thermal adjustments via SYNOP measurements allows the model to maintain a broad latitudinal 850 hPa geopotential corridor over the Aegean Sea relative to SY_GN (Figs. 12h, i). This configuration drives greater moisture and heat transport toward Lemnos Island (Figs. 13h, i and 14h, i), causing the model to overestimate local precipitation (Figs. 15i and 16i). As this heat and moisture mass subsequently reaches the northern coastline (Fig. S16), it results in a precipitation overestimation across the eastern edge of Chalkidiki during both the 6- and 12-hour accumulation windows (Figs. 15i and 16i).

Integrating surface observations in the SY_GN simulation alters these downstream dynamics. The SYNOP data introduce a distinct low-level cooling footprint over the Aegean basin that modifies regional geopotential height gradients relative to the GN baseline (Figs. 12g, h). Instead of maintaining a sharply focused transport axis, this altered circulation forces the low-level thermodynamic fluxes to expand broadly across the wider northern Aegean marine basin (Figs. 13i and 14i). Because the advected water vapor mass spreads laterally across the open sea rather than concentrating into a narrow core, the net thermodynamic flux reaching the northern coast is effectively diluted relative to the focused core that veered westward just north of Lemnos in GN (Figs. S16 and S17). Consequently, SY_GN exhibits a less pronounced overestimation over Chalkidiki than the standalone GN run (Figs. 15i, j and 16i, j). Conversely, precipitation over Lemnos Island becomes severely underestimated as the eastern marine branch shifts westward.

Across the broader Chalkidiki area, neither simulation corrects the rainfall magnitude, as both underestimate precipitation across both short and extended time windows. In central Sterea Ellada and the northern Peloponnese, both runs yield results during the initial 6 hours that are similar to those of the staged simulations (Figs. 15g, i). Over the 12-hour period, however, the performance of GN deteriorates across central and western Greece due to an overestimation of precipitation, whereas SY_GN performs better in these regions (Figs. 16g, i).

3.2.3.2 The southern maritime inflow (Crete & Rhodes Islands)

However, when GNSS PWV and/or SYNOP measurements are included (all data assimilation simulations except for RADAR_OL1 and RADAR_OL3) in the data assimilation, the simulated low-level water vapor and heat transport over Rhodes increase notably (Figs. 13 and 14), allowing the model to successfully detect the precipitation (Figs. 15 and 16). Although this simulated rainfall remains underestimated and slightly misplaced toward the center of the island, its development highlights the crucial impact of local measurements. By directly updating the local thermodynamic fields, these observations successfully alter the magnitude and spatial extent of the primary marine rainband, which otherwise develops entirely to the east of the island in the unconstrained configurations.

For the island of Crete, the accumulated precipitation is altered when the SYNOP measurements are integrated into the data assimilation system. More specifically, the overestimation of precipitation (Figs. 15 and 16) is largely driven by the enhanced horizontal transport of heat and moisture in the area caused by the GNSS PWV observations compared to NODA (Figs. 13 and 14). The ground station measurements restrain this increase in horizontal transport, keeping the simulated precipitation closer to the observations.

Consequently, SY_GN_RA_stages performs better in this area than GN_RA_stages. The same is true for SY_GN_RA_synch and SY_GN compared to GN_RA_synch and GN, respectively. This improvement arises from the drying effect of the SYNOP observations, which sharpen and better define the boundaries of the moisture plumes.

4. Discussion

4.1 The Impact of Sequential (Stages) versus Synchronous (Synch) Assimilation

Overall, the two-stage sequential data assimilation configurations (GN_RA_stages and SY_GN_RA_stages) outperform the synchronous configurations. This predictive advantage is evident across nearly all rainfall thresholds, from light to heavy regimes and it is particularly pronounced within the localized 200 km radar range domain. However, this superior performance is accompanied by the trade-offs in spatial placement, including downstream overestimation over Chalkidiki and in the case of SY_GN_RA_stages a persistent dry bias over Lemnos.

The underlying cause of these divergent behaviors is that the synchronous simulations (GN_RA_synch and SY_GN_RA_synch) are forced to ingest high-resolution radar reflectivity data concurrently with either deep-column integrated precipitable water vapor (GNSS PWV) or GNSS PWV and surface SYNOP observations together. This simultaneous ingestion induces sudden, localized diabatic heating that sharpens the geopotential height gradients across the Attica–Lemnos latitudinal corridor. This modification oversteers the eastern maritime branch too far to the west of its natural trajectory. This structural oversteering directly triggers the severe dry biases observed over Lemnos Island, as well as the downstream precipitation misplacements during the early hours of the forecast lifecycle. Furthermore, this synchronous configuration results in a northward misplacement of the low core which weakens the cyclonic turning of the moist airstream and leads to an underestimation of rainfall over the western coast. Such rapid thermal and moisture imbalances introduced by the analysis are well-documented vulnerabilities of synchronous multi-source 3D-Var systems. Unlike four-dimensional variational systems (Huang et al., 2009), which use time-dependent model physics to smoothly integrate asynchronous observations, a static 3D-Var update ingests all data at a single instant. This sudden insertion disrupts local mass and wind fields, creating artificial imbalances that distort the early convective evolution.

In contrast, the sequential configurations (GN_RA_stages and SY_GN_RA_stages) bypass this broad latent heating by introducing the radar echoes into a moisture-corrected background state. This step-wise implementation is consistent with Tong et al. (2016), who demonstrated that assimilating synoptic-scale and radar observations in separate 3D-Var steps, rather than simultaneously, produced a more accurate quantitative precipitation forecast by allowing each observation type to constrain its own characteristic scale before the other is introduced. Consequently, the improved representation of both the eastern maritime and western continental moisture branches enables a more accurate capture of the overall rainfall pattern.

4.2 The Impact of Multi-Loop (OL3) versus Single-Loop (OL1) Radar Reflectivity Assimilation

The comparison between the single outer loop (RADAR_OL1) and multi-outer loop (RADAR_OL3) configurations reveals a distinct, threshold-dependent performance split rather than a sweeping superiority of one setup over the other. Specifically, multiple outer loops optimize the broad spatial structure of light-to-moderate rainbands, whereas a single outer loop better preserves the localized intensity of heavy convective rain. This behavior is supported by both nationwide and 200 km radar range metrics across the 6-hour and 12-hour windows. In light-to-moderate precipitation thresholds (≥ 15 and ≥ 20 mm), the multi-loop configuration refines widespread stratiform structures, yielding higher CSI scores. This specific improvement is highly consistent with Tong et al. (2016), who noted that multiple outer loop iterations in 3D-Var radar data assimilation allow the non-linear observation operators to gradually adjust the background state, effectively optimizing widespread mesoscale rainbands.

On the other hand, in heavy precipitation thresholds (≥ 30-40 mm), RADAR_OL1 avoids the over-smoothing or dampening effects inherent to multiple iterations, outscoring RADAR_OL3 at the 30 mm and 40 mm thresholds during both verification periods. As shown in Mediterranean convective environments by Maiello et al. (2014), localized convective cores can be overly suppressed or diluted when subjected to repetitive, non-linear minimization updates that tend toward a smoother, widespread analysis mean. This is consistent with Vendrasco et al. (2020), who compared one- and two-outer-loop 3D-Var radar configurations for convective nowcasting and similarly found that additional outer loops increased spurious convection and false alarm rates while providing only a small gain in detection, resulting in better overall skill with a single outer loop. The authors linked this behavior to the same dynamical-balance vulnerability addressed by the large-scale analysis constraint of Vendrasco et al. (2016) where each additional non-linear minimization pass has the potential to compound noise in the analysis when the background is not otherwise constrained. Hence, regulating the amount of evaporative cooling injected through the selection of outer loops introduces key structural changes that can be optimized to enhance precipitation forecast skill.

4.3 The Impact of SYNOP observations across Data Assimilation Configurations

The integration of surface synoptic observations introduces a horizontal boundary constraint to the lower troposphere, altering the spatial allocation of precipitation by modulating heat and moisture advection near the surface. In particular, assimilating GNSS PWV alone (GN) captures broad, light-to-moderate rainbands well by humidifying the atmosphere, but it suffers from unconstrained moisture transport. Conversely, when surface synoptic measurements are included (SY_GN), this excess moisture is spatially confined, and the warm sector of the storm is cooled. This surface anchoring process is physically supported by classical variational principles (e.g., Lorenc, 1986; Bannister, 2017), where ground-level mass observations bound the planetary boundary layer and restrain unconstrained multi-source adjustments aloft. While this structural constraint slightly dampens forecast performance for lighter rainfall thresholds, it improves prediction accuracy for heavy, localized convective rainfall cores (≥ 30 mm) within the short-term 6-hour period. Beyond this initial window, however, the positive impact of the SYNOP data fades (Table 2). This is a transient behavior consistent with other high resolution Mediterranean data assimilation studies, where the forecast benefits of assimilated observations on convective-scale precipitation have similarly been found to be short-lived, typically lasting only a few hours before decaying (Carrió et al., 2025). Specifically, when evaluated over the broader 12-hour window the metrics show a minor deterioration compared to those calculated for the 6-hour window when moderate to high precipitation thresholds are considered (≥15, ≥20, ≥30, ≥40 mm) (Table 2). This temporal decay reflects the rapid upscale error propagation typical of localized severe convective events, where fine-scale unconstrained mesoscale dynamics over time supersede the initial surface-level corrections (Rotunno and Snyder, 2008).

Table 2. Relative improvement values of CSI compared to baseline for the GN and SY_GN for the whole Greek region. The bold black values depict the drop of forecast skill of SY_GN compared to GN for the 12-h window.

simulation	**≥ 5 mm**		**≥ 10 mm**		**≥ 15 mm**		**≥ 20 mm**		**≥ 30 mm**		**≥ 40 mm**	
rel. improv.	6-h	12-h	6-h	12-h	6-h	12-h	6-h	12-h	6-h	12-h	6-h	12-h
GN (%)	+6	-5	+12	+0.3	+13	**+1**	+5	**+17**	+142	**-4**	20	**-5**
SY_GN (%)	+3	-2	-14	+2	+4	**-4**	+20	**-4**	+233	**-10**	-20	**-19**

In the synchronous configuration, SYNOP measurements partly buffer the sudden localized diabatic heating that heavily oversteers moisture to the west, which otherwise causes severe dry biases over Lemnos Island in the GN_RA_synch run. This stabilizing effect improves the short-term (6-hour) nationwide CSI across light-to-moderate thresholds, reducing the initial shocks arising from concurrent observation data ingestion into the system.

Similarly, within the sequential framework, the addition of SYNOP observations (SY_GN_RA_stages) unlocks a clear performance increase during the short-term 6-hour window for high-intensity convective rainfall thresholds (≥ 30 mm), yielding a notable relative improvement over the baseline, outperforming the GN_RA_stages. In addition, examining the CSI within the mature 12-hour window shows that surface anchoring stabilizes the 30 mm threshold, shifting a -10% deficit in GN_RA_stages relative to NODA into a +6% relative gain (whole Greek region). Consequently, these metrics confirm that anchoring the planetary boundary layer with surface observations provides an essential physical mechanism for preserving the structural placement and intensity of the heaviest convective cores across both synchronous and sequential data assimilation configurations.

4.4 The Impact of Radar Reflectivity Insertion across GNSS and SYNOP Configurations

The prognostic gain of inserting radar reflectivity data into both the standalone GN and SY_GN frameworks is examined.

Comparing the GN against its radar-augmented counterpart, GN_RA_stages, reveals that radar insertion provides a systematic improvement in the long-term placement of broad precipitation zones. This is evident in the 12-hour window, where GN_RA_stages yields higher CSI scores across light-to-moderate thresholds across both examined regions (≥5, ≥10, ≥15, ≥20 mm). However, adding radar to GN leads to short and long-term spatial displacements of convective cells, leading to a drop in the 6-hour heavy rainfall thresholds (≥ 30, 40 mm).

When radar reflectivity is added to the surface-constrained framework (SY_GN_RA_stages), it provides a balanced and resilient forecast. The radar echoes build upon the anchored low troposphere thermodynamics established by SY_GN. This combination minimizes the short-term

(6 hours window) high-threshold degradation and maximizes mature-stage (12-hour window) skill.

Examining whether it is more beneficial to combine GNSS PWV observations with surface stations (SY_GN) or radar reflectivity (GN_RA_stages) highlights an operational trade-off between focusing on the environment the storm grows in, or on the storm itself. GN_RA_stages leverages microphysical adjustments, outperforming SY_GN across light-to-moderate thresholds (from ≥ 5 up to ≥15 mm) in the 6-hour window and extends this advantage for the ≥40 mm threshold. At the ≥ 20 and ≥ 30 mm thresholds, however, SY_GN achieves a larger relative improvement over NODA than GN_RA_stages during the short term 6-hour window. This suggests that surface networks provide a short-lived edge specifically for the most localized, highest-intensity convective cores in the earliest forecast hours. GN_RA_stages in the long run (12-hour window) outperforms SY_GN in almost all precipitation thresholds (except for ≥ 40 mm) which denotes that the radar-augmented GNSS assimilation offers the more consistently reliable configuration both across the broader precipitation spectrum and over the longer forecast window.

5. Summary and Conclusions

The primary objective of this study was to evaluate the prognostic impact of synchronous versus sequential data assimilation configurations, the optimal looping of radar reflectivity updates, and the sole or combined effects of radar, GNSS, and SYNOP observations. Based on the comprehensive verification metrics and physical diagnostics, the main conclusions are summarized below:

- The two-stage sequential data assimilation configurations (GN_RA_stages and SY_GN_RA_stages) consistently outperform their synchronous counterparts across nearly all precipitation intensity thresholds, particularly within the localized 200 km radar range.
- Synchronous data ingestion induces a sudden diabatic heating that oversteers moisture transport to the west. Sequential configurations introduce radar echoes into an already moisture-corrected background state restoring the natural trajectory of the marine moisture transport.

- The selection of radar reflectivity outer loops reveals a distinct, threshold-dependent trade-off rather than a uniform superiority. A multi-outer-loop approach refines widespread stratiform structures and improves light-to-moderate rainband placement (≥ 5–20 mm), whereas a single outer loop prevents the excessive smoothing of peak intensities, yielding superior skill for heavy convective thresholds (≥ 30–40 mm).
- The integration of surface synoptic observations (SYNOP) introduces an essential horizontal boundary constraint to the lower troposphere that restricts low-level moisture transport. By cooling the storm's warm sector, surface anchoring suppresses widespread wet biases in light-to-moderate precipitation thresholds while preserving the structural placement and localized intensity of heavy convective cores (≥ 30 mm) during the short-term 6-hour window.
- Complementing a GNSS baseline with surface stations (SY_GN) provides a rigid ground-level boundary constraint that excels at early storm localization at the short-term 6-hour ≥ 30 mm threshold. In contrast, radar-only and sequential radar adjustments (GN_RA_stages) better preserve localized light-to-moderate precipitation skill over extended forecast lead times within the radar domain.
- The sequential configuration utilizing GNSS PWV and radar reflectivity measurements (GN_RA_stages) yields the highest forecast skill across light-to-moderate thresholds, where it benefits from flexible moisture steering. However, incorporating SYNOP observations into this sequential chain (SY_GN_RA_stages) introduces a vital structural constraint that enhances broad nationwide error reduction, preserves forecast skill over longer lead times, and reliably captures the heaviest convective cores across both spatial domains.

This study demonstrates that the assimilation of radar reflectivity, GNSS PWV, and SYNOP observations and the order and configuration in which they are combined measurably affects forecast skill for high-impact Mediterranean rainfall events. Building on these results, several avenues for future work emerge. Future work should explore the impact of higher-frequency cycling windows to determine if accelerated radar updates can improve the forecast quality of such systems. Additionally, a thorough sensitivity study should be performed to properly calibrate the length and variance scale factors within the WRFDA model to maximize the observational impact on the data assimilation forecast. Also, in multi-stage sequential configurations, the background error covariance matrix in the second analysis step should be dynamically updated based on the analysis error covariance derived from the first step, as demonstrated by Xu et al. 2016. Finally, this framework should be applied to a broader variety of Mediterranean convective events, including more complex cyclones such as medicanes, to test the operational versatility and statistical robustness of these suggested configurations.

Acknowledgements

This work is realized within the CYGMEN project (Project Protocol Number: STRATEGIC INFRASTRUCTURES/1222/0198). It was conducted in the framework of the "RESTART 2016-2020" Programmes for Research, Technological Development and Innovation (RTDI), which is co-financed by the Republic of Cyprus and the European Regional Development Fund. The authors gratefully acknowledge General Aviation Applications 3D SA for providing the raw weather radar data used in this study. With extensive experience in weather modification, meteorological applications, and weather radar operations, 3D S.A.'s support and willingness to make these data available were essential for the successful completion of this research.

All the data which are used in this study can be found at https://zenodo.org/ with a registered DOI: 10.5281/zenodo.21725315. For any questions regarding the methodology and analysis, please contact a.dimitrelos@noa.gr.

References

Bannister, R.N., 2017. A review of operational methods of variational and ensemble-variational data assimilation. Q.J.R. Meteorol. Soc. 143, 607-633. https://doi.org/10.1002/qj.2982

Barker, D. M., Huang, W., Guo, Y., Bourgeois, A. J., Xiao, Q.N., 2004: A Three-Dimensional Variational Data Assimilation System for MM5: Implementation and Initial Results. Mon. Wea. Rev. 132, 897–914. https://doi.org/10.1175/1520-0493(2004)132<0897:ATVDAS>2.0.CO;2

Barker, D., Xiang-Yu, H., Liu, Z., Auligné, T., Zhang, X., Rugg, S., Ajjaji, R., Bourgeois, A., et al., 2012. The Weather Research and Forecasting Model's Community Variational/Ensemble Data Assimilation System: WRFDA. Bull. Amer. Meteor. Soc. 93, 831–843. https://doi.org/10.1175/BAMS-D-11-00167.1

Caldas-Alvarez, A., Khodayar, S., 2020. Assessing atmospheric moisture effects on heavy precipitation during HyMeX IOP16 using GPS nudging and dynamical downscaling. Nat. Hazards Earth Syst. Sci. 20, 2753–2776. https://doi.org/10.5194/nhess-20-2753-2020

Carrió, D. S., Mazzarella, V., Ferretti, R., 2025. High-resolution data assimilation for two maritime extreme weather events: a comparison between 3D-Var and EnKF. Nat. Hazards Earth Syst. Sci. 25, 2999–3026. https://doi.org/10.5194/nhess-25-2999-2025

Choi, Y., Cha, D.-H. Kim, J., 2017. Tuning of length-scale and observation-error for radar data assimilation using four dimensional variational (4D-Var) method. Atmos. Sci. Lett, 18, 441-448. https://doi.org/10.1002/asl.787

Davolio, S., Miglietta, M. M., Moscatello, A., Pacifico, F., Buzzi, A., Rotunno, R., (2009). Numerical forecast and analysis of a tropical-like cyclone in the Ionian Sea. Nat. Hazards Earth Syst. Sci. 9, 551–562. https://doi.org/10.5194/nhess-9-551-2009

Duda, J. D., Wang, X., Wang, Y., Carley, J. R., 2019. Comparing the Assimilation of Radar Reflectivity Using the Direct GSI-Based Ensemble–Variational (EnVar) and Indirect Cloud Analysis Methods in Convection-Allowing Forecasts over the Continental United States. Mon. Wea. Rev. 147, 1655–1678. https://doi.org/10.1175/MWR-D-18-0171.1

Ebert, E.E., 2008. Fuzzy verification of high-resolution gridded forecasts: a review and proposed framework. Met. Apps. 15, 51-64. https://doi.org/10.1002/met.25

Flaounas, E., Kotroni, V., Lagouvardos, K. et al., 2018. Heavy rainfall in Mediterranean cyclones. Part I: contribution of deep convection and warm conveyor belt. Clim Dyn. 50, 2935–2949. https://doi.org/10.1007/s00382-017-3783-x

Flaounas, E., Fita, L., Lagouvardos, K. et al., 2019. Heavy rainfall in Mediterranean cyclones, Part II: Water budget, precipitation efficiency and remote water sources. Clim Dyn. 53, 2539–2555. https://doi.org/10.1007/s00382-019-04639-x

Flaounas, E., Davolio, S., Raveh-Rubin, S., Pantillon, F., Miglietta, M. M., Gaertner, M. A., Hatzaki, M., Homar, V., Khodayar, S., Korres, G., Kotroni, V., Kushta, J., Reale, M., Ricard, D., 2022. Mediterranean cyclones: current knowledge and open questions on dynamics, prediction, climatology and impacts. Weather Clim. Dynam. 3, 173–208. https://doi.org/10.5194/wcd-3-173-2022

Flaounas, E., Dafis, S., Davolio, S., Faranda, D., Ferrarin, C., Hartmuth, K., Hochman, A., Koutroulis, A., Khodayar, S., Miglietta, M. M., Pantillon, F., Patlakas, P., Sprenger, M., Thurnherr, I., 2025. Dynamics, predictability, impacts and climate change considerations of the catastrophic Mediterranean Storm Daniel (2023). Weather Clim. Dynam. 6, 1515–1538. https://doi.org/10.5194/wcd-6-1515-2025

Giannaros, C., Kotroni, V., Lagouvardos, K., Giannaros, T. M., Pikridas, C., 2020. Assessing the Impact of GNSS ZTD Data Assimilation into the WRF Modeling System during High-Impact Rainfall Events over Greece. Remote Sensing. 12(3), 383. https://doi.org/10.3390/rs12030383

Grell, G. A., Freitas, S. R., 2014. A scale and aerosol aware stochastic convective parameterization for weather and air quality modeling. Atmos. Chem. Phys. 14, 5233–5250. https://doi.org/10.5194/acp-14-5233-2014

Haralambous, H., Oikonomou, C., Pikridas, C., et al., 2018. "BeRTISS project: Balkan-Mediterranean real-time severe weather service", Proc. SPIE 10773, Sixth International Conference on Remote Sensing and Geoinformation of the Environment (RSCy2018), 1077313; https://doi.org/10.1117/12.2324129

Hersbach, H., Bell B., Berrisford P., et al., 2020. The ERA5 global reanalysis. Q J R Meteorol Soc. 146, 1999–2049. https://doi.org/10.1002/qj.3803

Hong, S., Y. Noh, Dudhia, J., 2006. A New Vertical Diffusion Package with an Explicit Treatment of Entrainment Processes. Mon. Wea. Rev. 134, 2318–2341. https://doi.org/10.1175/MWR3199.1

Hsiao, L., Chen, D., Kuo, Y., Guo, Y., Yeh, T., Hong, J., Fong, C., Lee, C., 2012. Application of WRF 3DVAR to Operational Typhoon Prediction in Taiwan: Impact of Outer Loop and Partial Cycling Approaches. Wea. Forecasting. 27, 1249–1263. https://doi.org/10.1175/WAF-D-11-00131.1

Huang, X. Y., Xiao, Q., Barker, D. M., Zhang, X., Michalakes, J., Huang, W., et al., 2009. Four-Dimensional Variational Data Assimilation for WRF: Formulation and Preliminary Results. Mon. Wea. Rev. 137, 299–314. https://doi.org/10.1175/2008MWR2577.1

Iacono, M. J.,Delamere, J. S., Mlawer, E. J., Shephard, M. W., Clough, S. A., Collins, W. D., 2008. Radiative forcing by long-lived greenhouse gases: Calculations with the AER radiative transfer models. J. Geophys. Res. 113, D13103. https://doi.org/10.1029/2008JD009944

Kalnay, E., 2002. Atmospheric Modeling, Data Assimilation and Predictability. Cambridge: Cambridge University Press. https://doi.org/10.1017/CBO9780511802270

Khodayar, S., Kushta, J., Catto, J. L., Dafis, S., Davolio, S., Ferrarin, C., et al., 2025. Mediterranean cyclones in a changing climate: A review on their socio-economic impacts. Reviews of Geophysics. 63, e2024RG000853. https://doi.org/10.1029/2024RG000853

Lagouvardos, K., Kotroni, V., Bezes, A., Koletsis, I., Kopania, T., Lykoudis, S., Mazarakis, N., Papagiannaki, K., Vougioukas, S., 2017. The automatic weather stations NOANN network of the National Observatory of Athens: operation and database. Geosci. Data J. 4, 4-16. https://doi.org/10.1002/gdj3.44

Lagouvardos, K., Karagiannidis, A., Dafis, S., Kalimeris, A., Kotroni, V., 2022. Ianos—A Hurricane in the Mediterranean. Bull. Amer. Meteor. Soc. 103, E1621–E1636. https://doi.org/10.1175/BAMS-D-20-0274.1

Llasat, M. C., Llasat-Botija, M., Prat, M. A., Porcú, F., Price, C., Mugnai, A., Lagouvardos, K., Kotroni, V., Katsanos, D., Michaelides, S., Yair, Y., Savvidou, K., Nicolaides, K., 2010. High-impact floods and flash floods in Mediterranean countries: the FLASH preliminary database. Adv. Geosci. 23, 47–55. https://doi.org/10.5194/adgeo-23-47-2010

Lionello, P., Malanotte-Rizzoli, P., Boscolo, R. (Eds.)., 2006. Mediterranean climate variability (Vol. 4). Amsterdam: Elsevier.

Lorenc, A.C., 1986. Analysis methods for numerical weather prediction. Q.J.R. Meteorol. Soc. 112, 1177-1194. https://doi.org/10.1002/qj.49711247414

Maiello, I., Ferretti, R., Gentile, S., Montopoli, M., Picciotti, E., Marzano, F. S., Faccani, C., 2014. Impact of radar data assimilation for the simulation of a heavy rainfall case in central Italy using WRF–3DVAR, Atmos. Meas. Tech. 7, 2919–2935. https://doi.org/10.5194/amt-7-2919-2014

Michaelides, S., Karacostas, T., Sánchez, J. L., Retalis, A., Pytharoulis, I., Homar, V., Romero, R., Zanis, P., Giannakopoulos, C., Bühl, J., Ansmann, A., Merino, A., Melcón, P., Lagouvardos, K., Kotroni, V., Bruggeman, A., López-Moreno, J. I., Berthet, C., Katragkou, E., Tymvios, F., Hadjimitsis, D. G., Mamouri, R.-E., Nisantzi, A., 2018. Reviews and perspectives of high impact atmospheric processes in the Mediterranean. Atmospheric Research. 208, 4–44. https://doi.org/10.1016/j.atmosres.2017.11.022

Miglietta, M. M., 2019. Mediterranean Tropical-Like Cyclones (Medicanes). Atmosphere. 10(4), 206. https://doi.org/10.3390/atmos10040206

Miglietta, M. M., Laviola, S., Malvaldi, A., Conte, D., Levizzani, V., Price, C., 2013. Analysis of tropical-like cyclones over the Mediterranean Sea through a combined modeling and satellite approach. Geophys. Res. Lett. 40, 2400–2405. https://doi.org/10.1002/grl.50432

Miglietta, M. M., et al., 2025. Defining Medicanes: Bridging the Knowledge Gap between Tropical and Extratropical Cyclones in the Mediterranean. Bull. Amer. Meteor. Soc. 106, E1955–E1971. https://doi.org/10.1175/BAMS-D-24-0289.1

Papagiannaki, K., Lagouvardos, K., Kotroni, V., 2013. A database of high-impact weather events in Greece: a descriptive impact analysis for the period 2001–2011. Nat. Hazards Earth Syst. Sci. 13, 727–736. https://doi.org/10.5194/nhess-13-727-2013

Papagiannaki, K., Kotroni, V., Lagouvardos, K., 2026. Impact-Based Analysis of Weather-Related Hazards in Greece (2000–2025): Insights from the High-Impact Weather Events Database (HIWE-DB). Climate. 14(5), 105. https://doi.org/10.3390/cli14050105

Parrish, D. F., Derber, J. C., 1992. The National Meteorological Center's Spectral Statistical-Interpolation Analysis System. Mon. Wea. Rev. 120, 1747–1763. https://doi.org/10.1175/1520-0493(1992)120<1747:TNMCSS>2.0.CO;2

Ricchi, A., Miglietta, M. M., Barbariol, F., Benetazzo, A., Bergamasco, A., Bonaldo, D., Cassardo, C., Falcieri, F. M., Modugno, G., Russo, A., Sclavo, M., Carniel, S., 2017. Sensitivity of a Mediterranean Tropical-Like Cyclone to Different Model Configurations and Coupling Strategies. Atmosphere. 8(5), 92. https://doi.org/10.3390/atmos8050092

Rohm, W., Guzikowski, J., Wilgan, K., Kryza, M., 2019. 4DVAR assimilation of GNSS zenith path delays and precipitable water into a numerical weather prediction model WRF. Atmos. Meas. Tech. 12, 345–361. https://doi.org/10.5194/amt-12-345-2019

Rotunno, R., Snyder, C., 2008. A Generalization of Lorenz's Model for the Predictability of Flows with Many Scales of Motion. J. Atmos. Sci. 65, 1063–1076. https://doi.org/10.1175/2007JAS2449.1

Skamarock, W., Klemp, J., Dudhia, J., Gill, D. O., Liu, Z., Berner, J., Wang, W., Powers, J. G., Duda, M. G., Barker, D., Huang, X.-Y., 2019. A Description of the Advanced Research WRF Model Version 4.1. https://doi.org/10.5065/1dfh-6p97

Tewari, M., Chen, F., Wang, W., Dudhia, J., LeMone, M. A., Mitchell, K., Ek, M., Gayno, G., Wegiel, J., Cuenca, R. H., 2004. Implementation and verification of the unified noah land surface model in the WRF model. Bulletin of the American Meteorological Society, 2165-2170.

Thompson, G., Field, P. R., Rasmussen, R. M., Hall, W. D., 2008. Explicit Forecasts of Winter Precipitation Using an Improved Bulk Microphysics Scheme. Part II: Implementation of a New Snow Parameterization. Mon. Wea. Rev. 136, 5095–5115. https://doi.org/10.1175/2008MWR2387.1

Tong, W., Li, G., Sun, J., Tang, X., Zhang, Y., 2016. Design Strategies of an Hourly Update 3DVAR Data Assimilation System for Improved Convective Forecasting. Wea. Forecasting. 31, 1673–1695. https://doi.org/10.1175/WAF-D-16-0041.1

Vendrasco, E. P., Sun, J., Herdies, D. L., Frederico de Angelis, C., 2016. Constraining a 3DVAR Radar Data Assimilation System with Large-Scale Analysis to Improve Short-Range Precipitation Forecasts. J. Appl. Meteor. Climatol. 55, 673–690. https://doi.org/10.1175/JAMC-D-15-0010.1.

Vendrasco, E. P., Machado, L. A. T., Ribeiro, B. Z., Freitas, E. D., Ferreira, R. C., Negri, R. G., 2020. Cloud-Resolving Model Applied to Nowcasting: An Evaluation of Radar Data Assimilation and Microphysics Parameterization. Wea. Forecasting. 35, 2345–2365. https://doi.org/10.1175/WAF-D-20-0017.1

Wang, Y., Zhang, J., Chang, P. L., Langston, C., Kaney, B., Tang, L., 2016. Operational C-Band Dual-Polarization Radar QPE for the Subtropical Complex Terrain of Taiwan, Advances in Meteorology., 4294271, 15 pages. https://doi.org/10.1155/2016/4294271

Xiao, Q., Kuo, Y., Sun, J., Lee, W., Barker, D. M., Lim, E., 2007. An Approach of Radar Reflectivity Data Assimilation and Its Assessment with the Inland QPF of Typhoon Rusa (2002) at Landfall. J. Appl. Meteor. Climatol. 46, 14–22. https://doi.org/10.1175/JAM2439.1

Xiao, Q., Sun, J., 2007. Multiple-Radar Data Assimilation and Short-Range Quantitative Precipitation Forecasting of a Squall Line Observed during IHOP_2002. Mon. Wea. Rev. 135, 3381–3404. https://doi.org/10.1175/MWR3471.1

Xu, Q., Wei, L., Gao, J., Zhao, Q., Nai, K., Liu., S., 2016.
Multistep variational data assimilation: important issues and a spectral approach. Tellus A: Dynamic Meteorology and Oceanography. 68:1, 31110. https://doi.org/10.3402/tellusa.v68.31110

Supplement

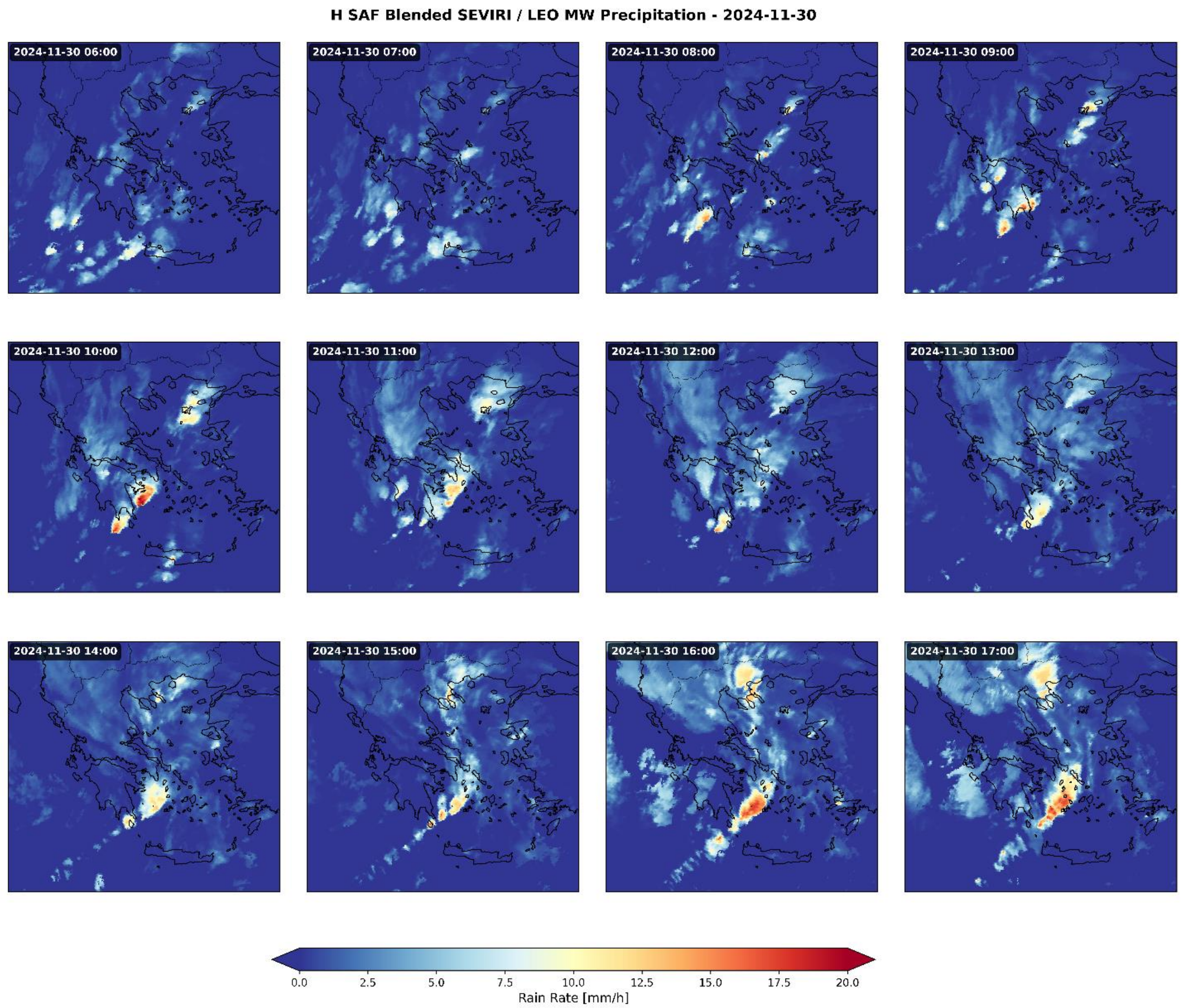

Fig. S1. Hourly evolution of the observed rainfall rate from the H SAF H60B product (Blended SEVIRI / LEO MW precipitation) during the BORA storm event on 30 November 2024, from 06:00 to 17:00 UTC. The sequence illustrates the spatial and temporal development of the precipitation system, including the initiation, organization, and subsequent evolution of the main rainbands over Greece and the surrounding region. The H SAF H60B rainfall rate estimates provide an observational reference for evaluating the representation of the storm evolution in the numerical simulations and data assimilation experiments. **Source:** EUMETSAT SAF on Support to Operational Hydrology and Water Management, copyright (2024) EUMETSAT (https://hsaf.meteoam.it/).

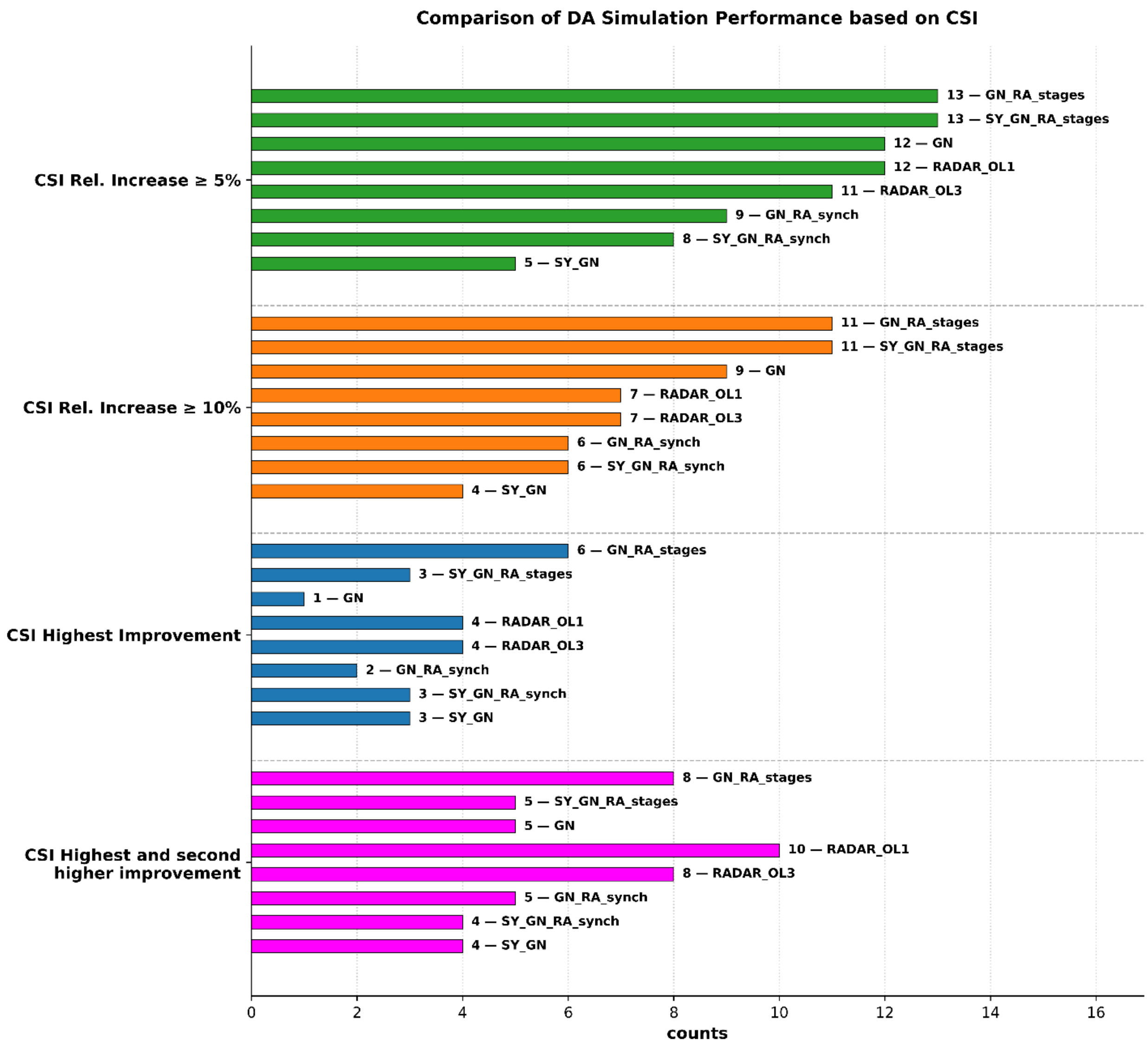

Fig. S2. Number of occurrences across all precipitation thresholds and time intervals where CSI achieved a relative improvement of ≥ 5% (first bar chart), ≥ 10% (second bar chart). The third and fourth bar charts display the number of instances where a given simulation achieved the highest overall CSI, and the highest or second-highest CSI, respectively, compared to all other simulations.

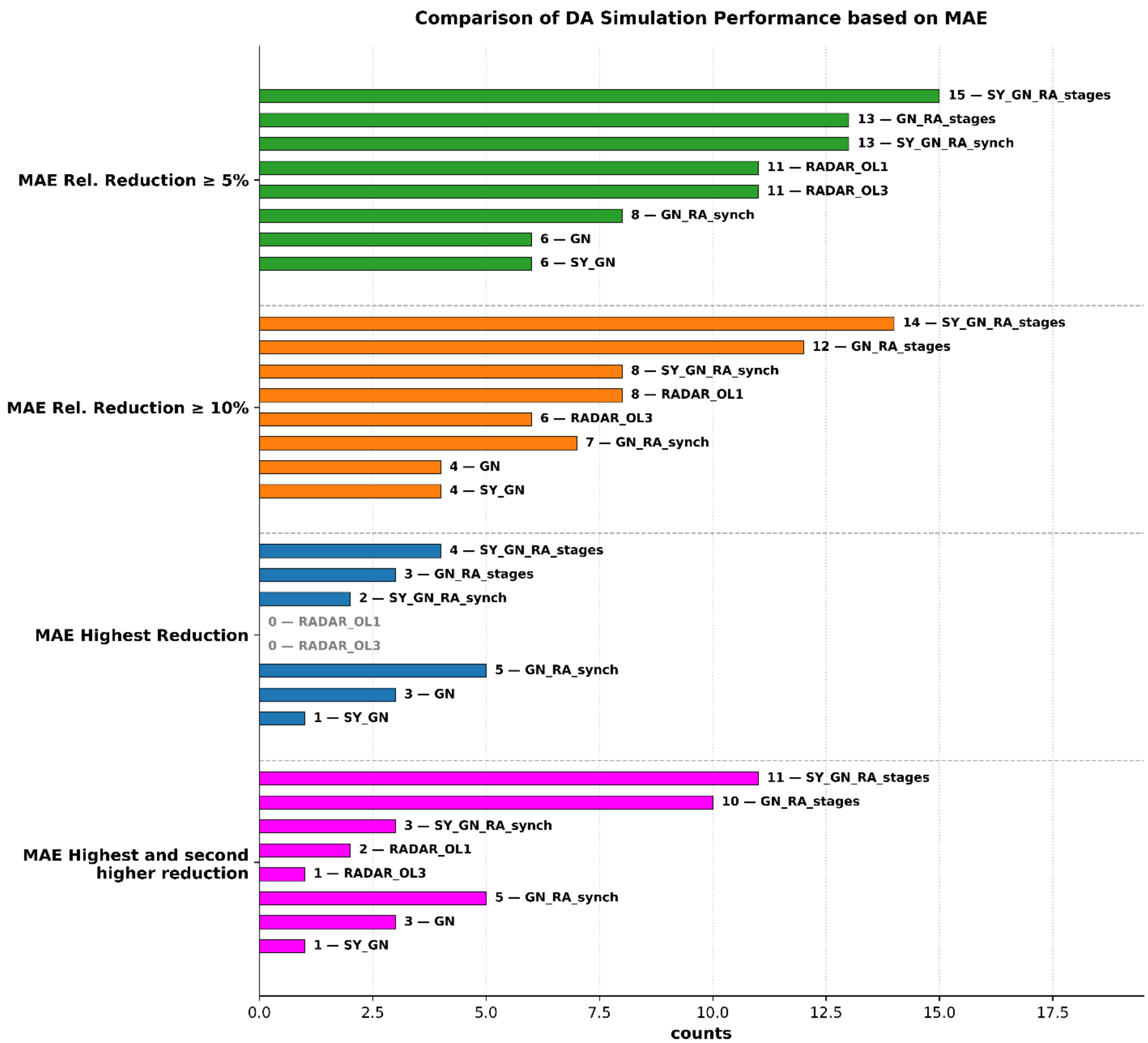

Fig. S3. Number of occurrences across all precipitation thresholds and time intervals where MAE achieved a relative improvement of ≥ 5% (first bar chart), ≥ 10% (second bar chart). The third and fourth bar charts display the number of instances where a given simulation achieved the highest overall MAE, and the highest or second-highest MAE, respectively, compared to all other simulations.

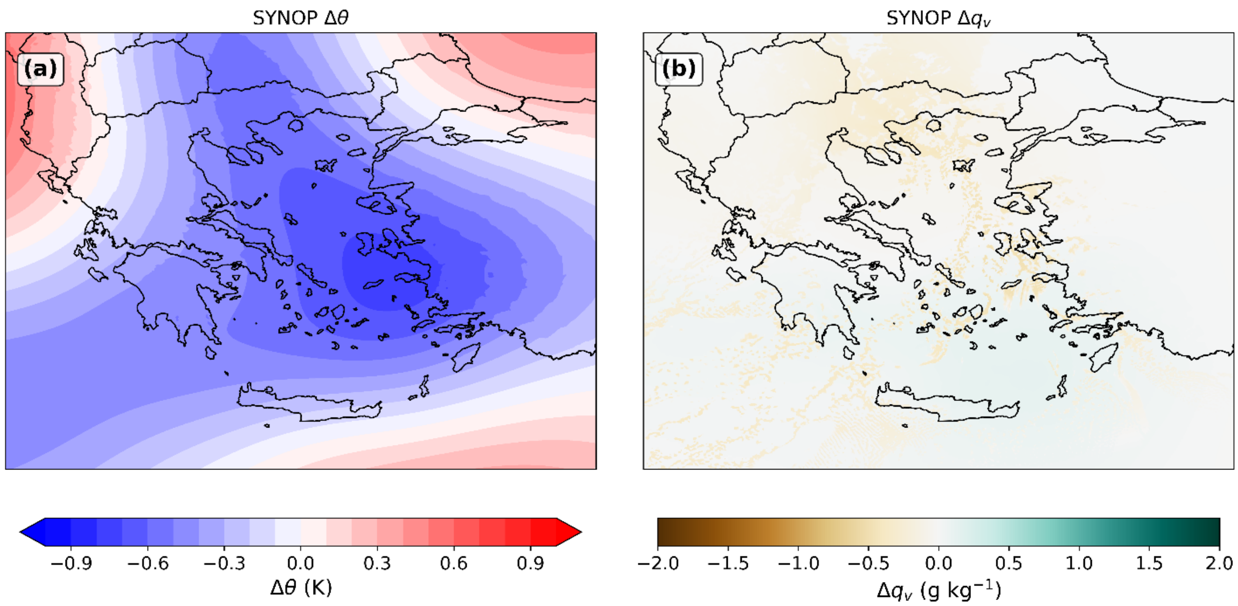

Fig. S4. Analysis increments of potential temperature (a) and water vapor mixing ratio (b) from the SYNOP data assimilation experiment at the 9th WRF model level over Greece. The increments are calculated relative to the background (first-guess) state as ($\Delta\theta=\theta_{SYNOP}-\theta_B$) and ($\Delta qv=qv_{SYNOP}-qv_B$), where (θ) is the potential temperature and (q_v) is the water vapor mixing ratio, Δθ is the potential temperature increment (K), Δqv is the water vapor mixing ratio increment (kg kg^{-1}), θ_{SYNOP} and qv_{SYNOP} are the potential temperature and water vapor mixing ratio after SYNOP assimilation, θ_B and qv_B are the corresponding background (first-guess) fields. The left panel shows the potential temperature increments in K, while the right panel presents the corresponding water vapor mixing ratio increments in kg kg^{-1}. Positive values indicate an increase of the respective variable introduced by the SYNOP assimilation, whereas negative values indicate a reduction relative to the background field.

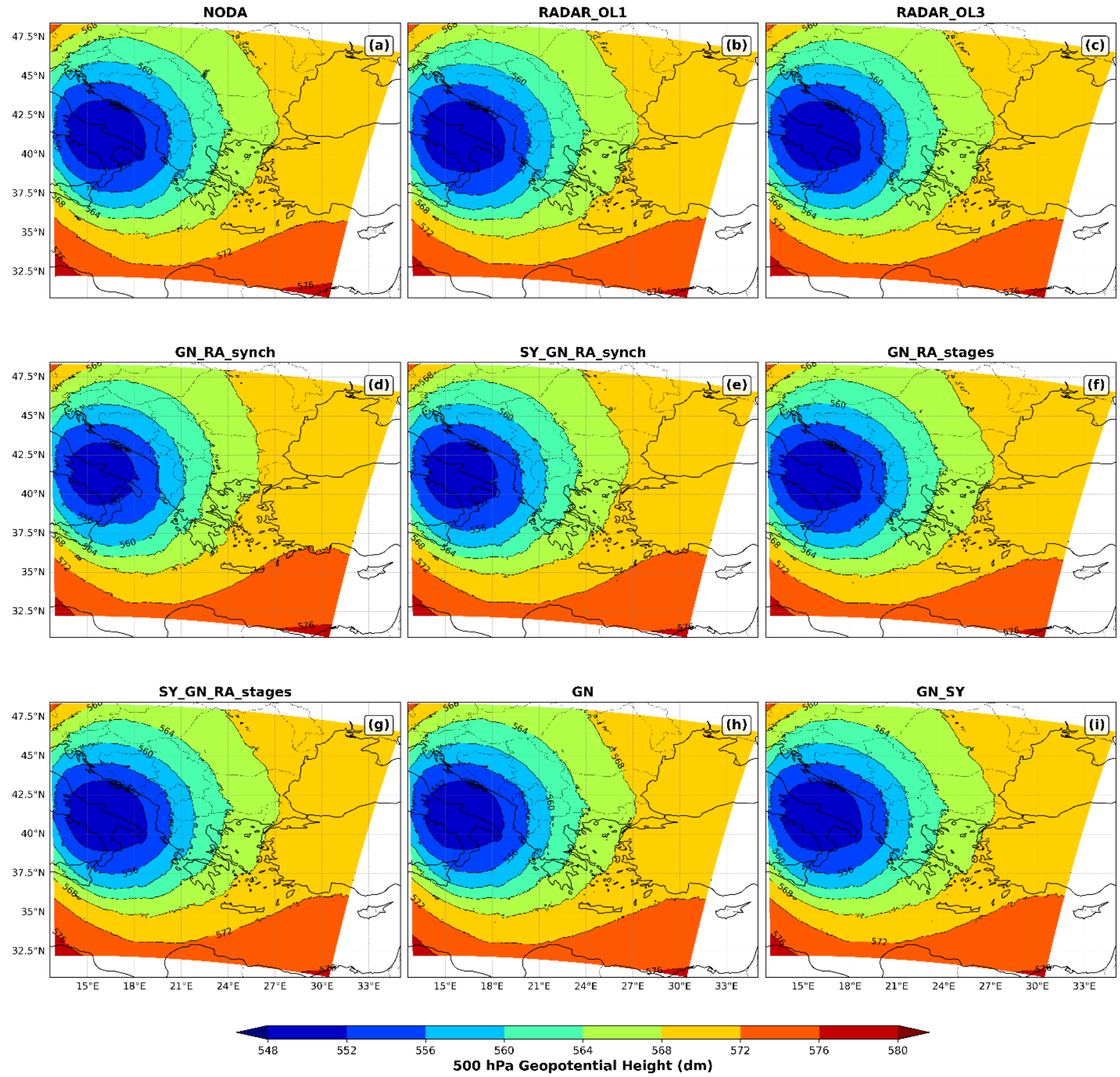

Fig. S5. Geopotential height at the 500 hPa pressure level for the nine numerical experiments (a-i) at 09:00 UTC over Greece and the surrounding eastern Mediterranean region. The 500 hPa geopotential height field was obtained by vertical interpolation of the WRF three-dimensional geopotential height field to the 500 hPa isobaric surface. Filled contours represent geopotential height values in decameters (dm), with contour intervals of 4 dm. The figure illustrates the impact of the different data assimilation configurations on the mid-tropospheric circulation pattern. Differences among the experiments indicate modifications in the position and intensity of synoptic-scale features, such as ridges and troughs, resulting from the assimilation of the available observations compared with the NODA (no data assimilation) experiment.

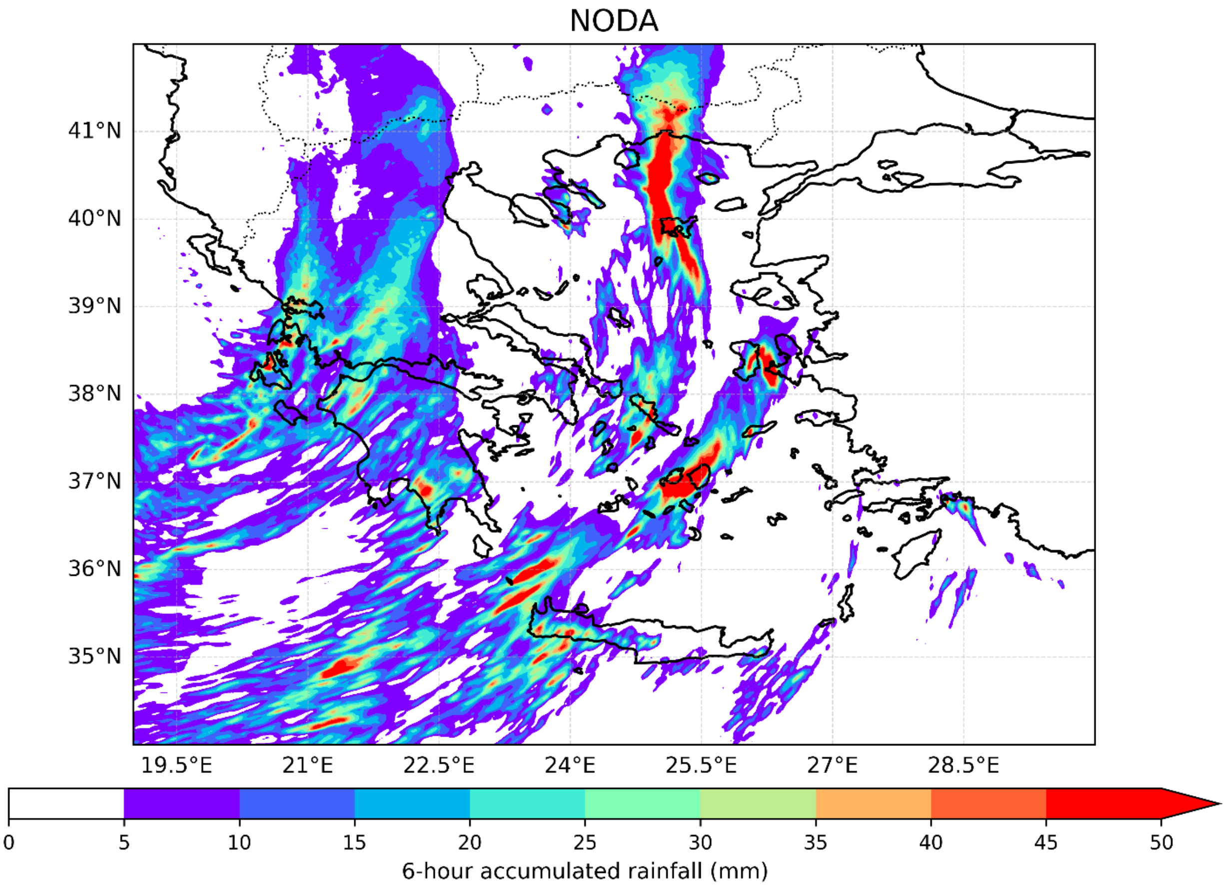

Fig. S6. 6-hour accumulated rainfall from the NODA experiment for the period 06:00–12:00 UTC on 30 November 2024 over Greece and the surrounding region. Filled contours represent rainfall accumulation (mm) with intervals of 5 mm.

NODA

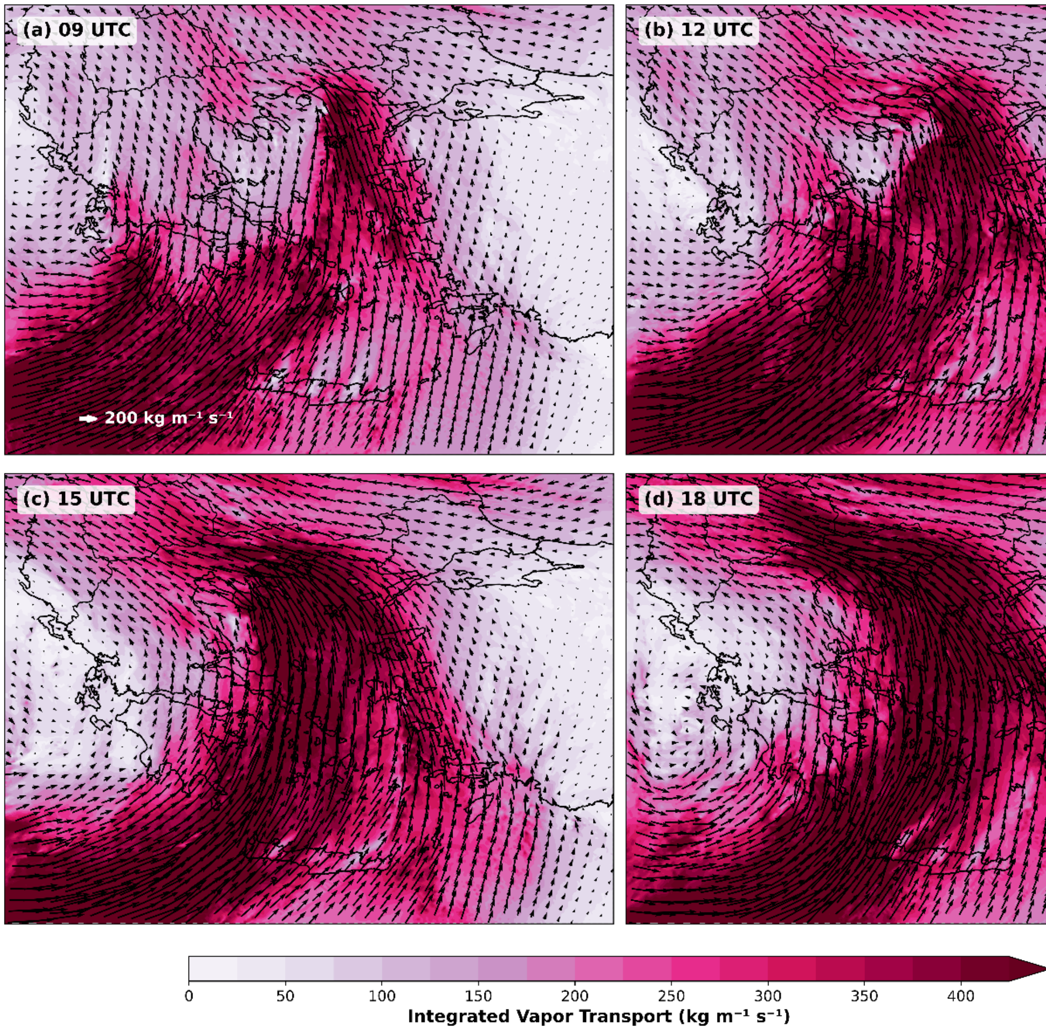

Fig. S7. Horizontal water vapor mixing ratio transport integrated from surface up to about 300hPa (corresponds to 22^{th} eta level) (IVT) of NODA. The figures show the evolution of IVT every 3 hours from 09 UTC to 18 UTC on 30/11/2024.

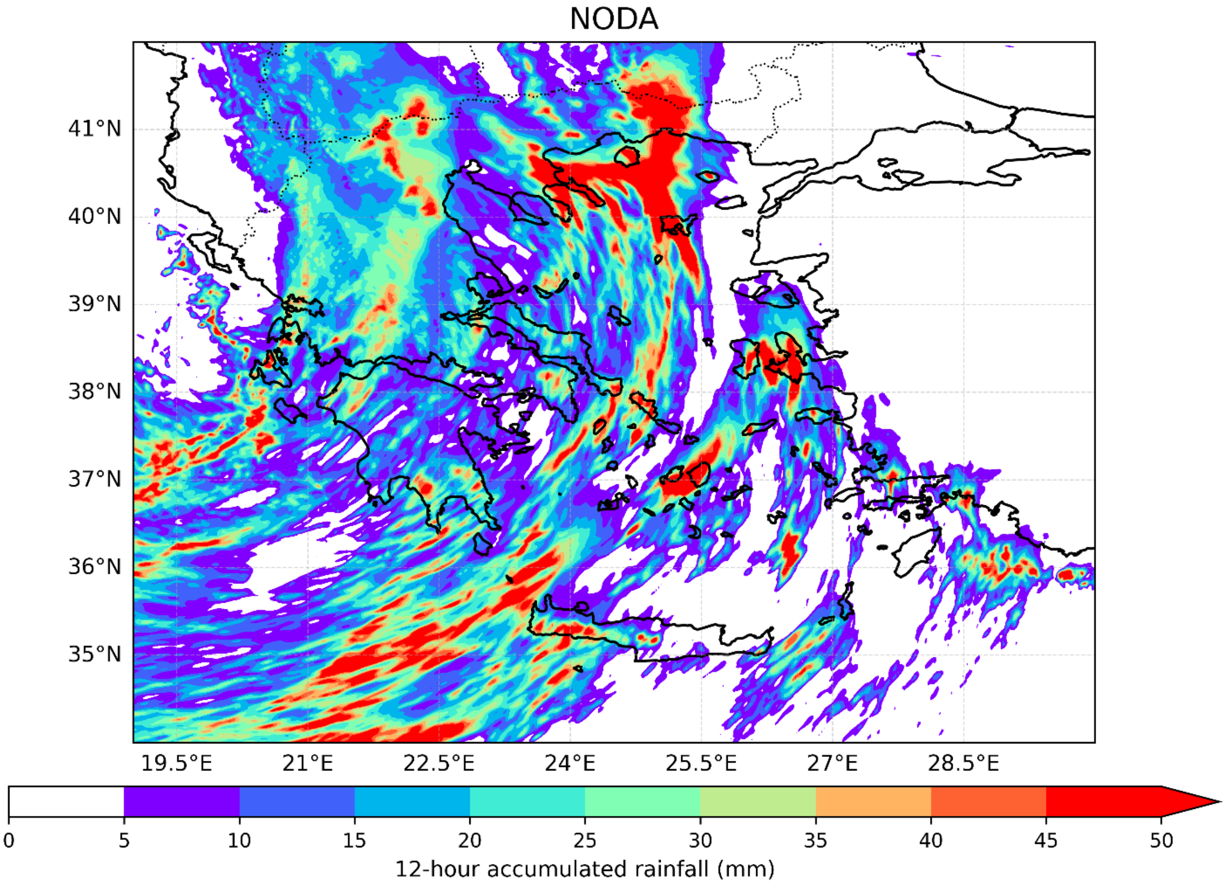

Fig. S8. 12-hour accumulated rainfall from the NODA experiment for the period 06:00–18:00 UTC on 30 November 2024 over Greece and the surrounding region. Filled contours represent rainfall accumulation (mm) with intervals of 5 mm.

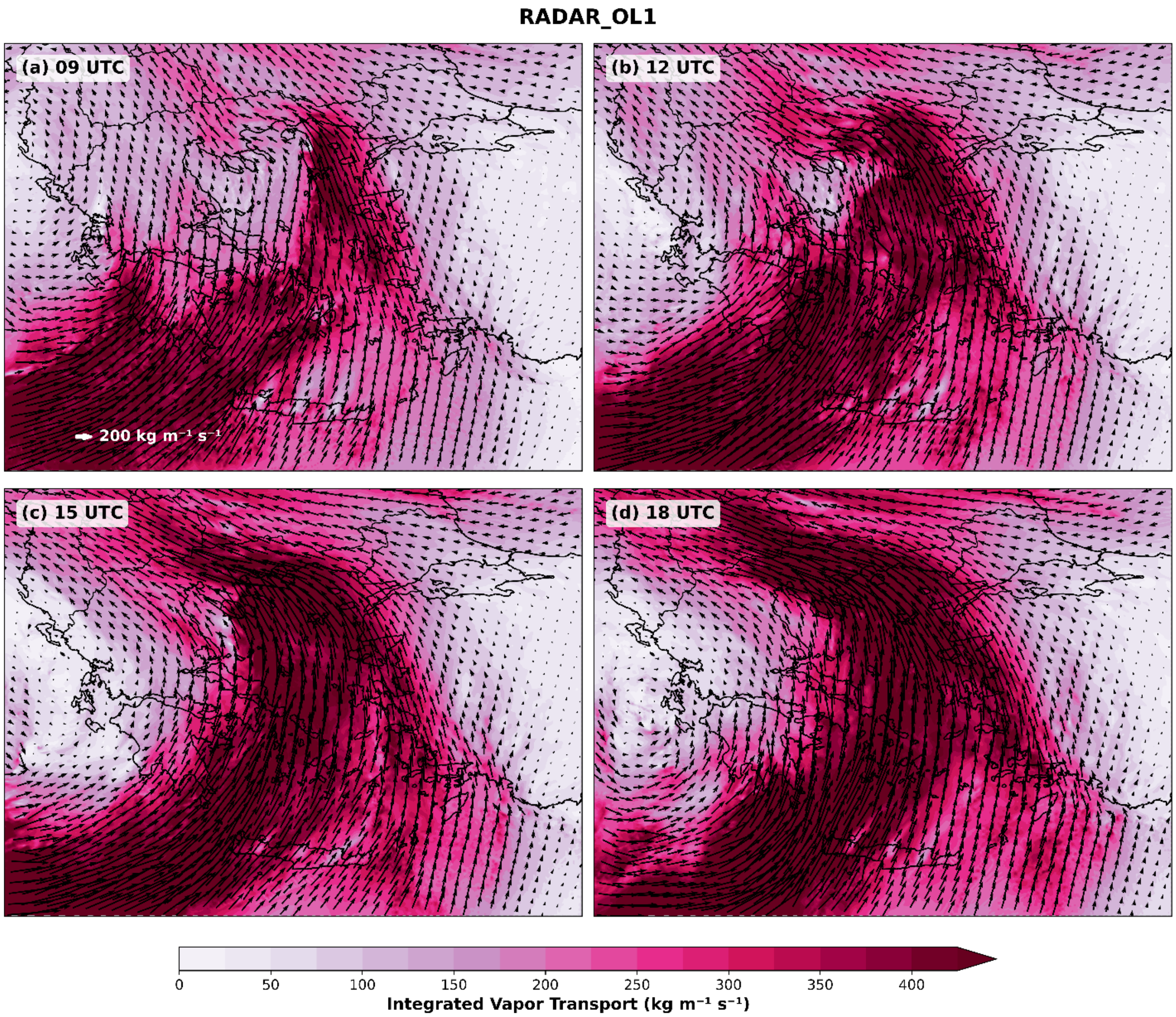

Fig. S9. Horizontal water vapor mixing ratio transport integrated from surface up to about 300hPa (corresponds to 22th eta level) (IVT) of RADAR_OL1. The figures show the evolution of IVT every 3 hours from 09 UTC to 18 UTC on 30/11/2024.

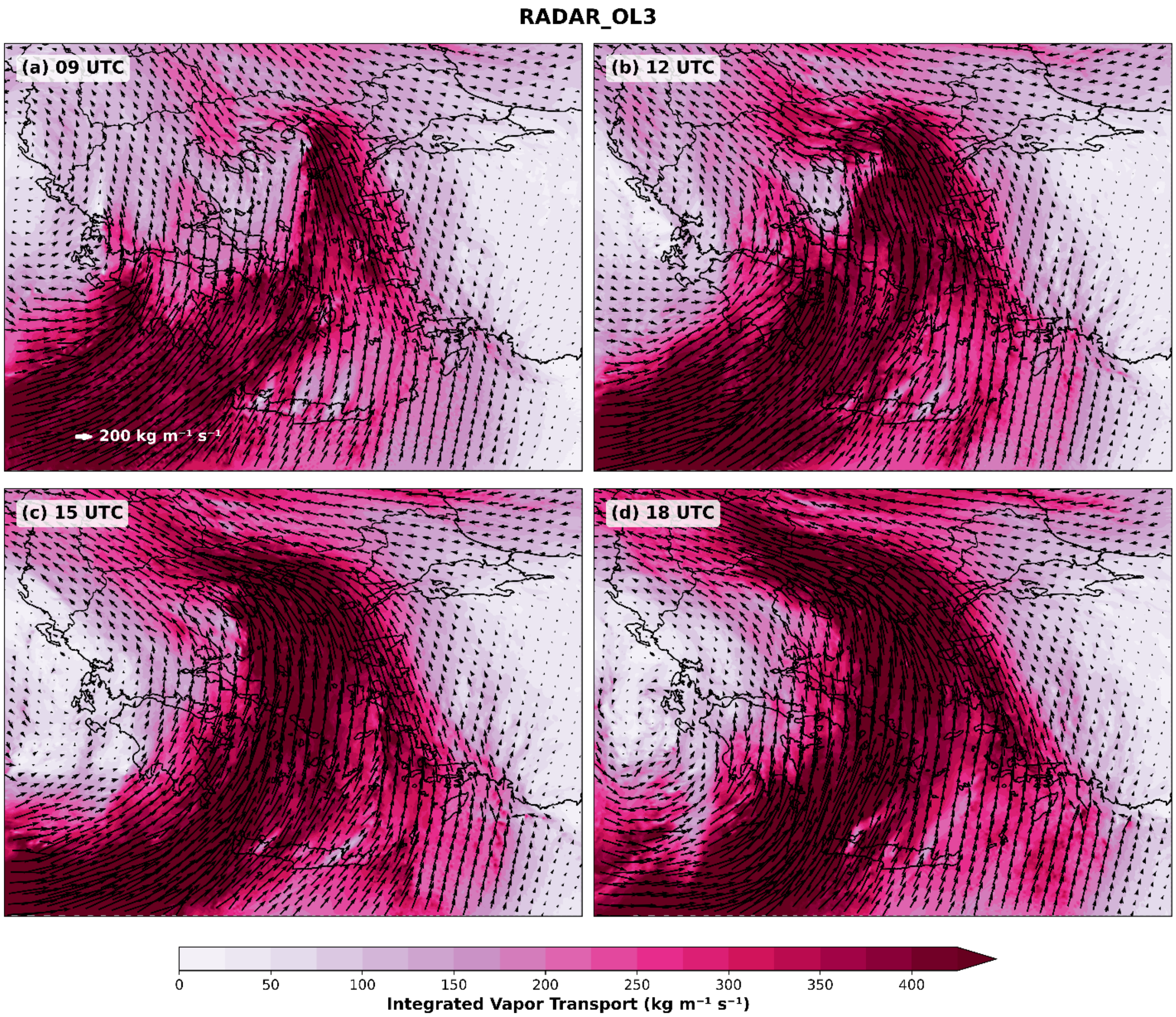

Fig. S10. Horizontal water vapor mixing ratio transport integrated from surface up to about 300hPa (corresponds to 22th eta level) (IVT) of RADAR_OL3. The figures show the evolution of IVT every 3 hours from 09 UTC to 18 UTC on 30/11/2024.

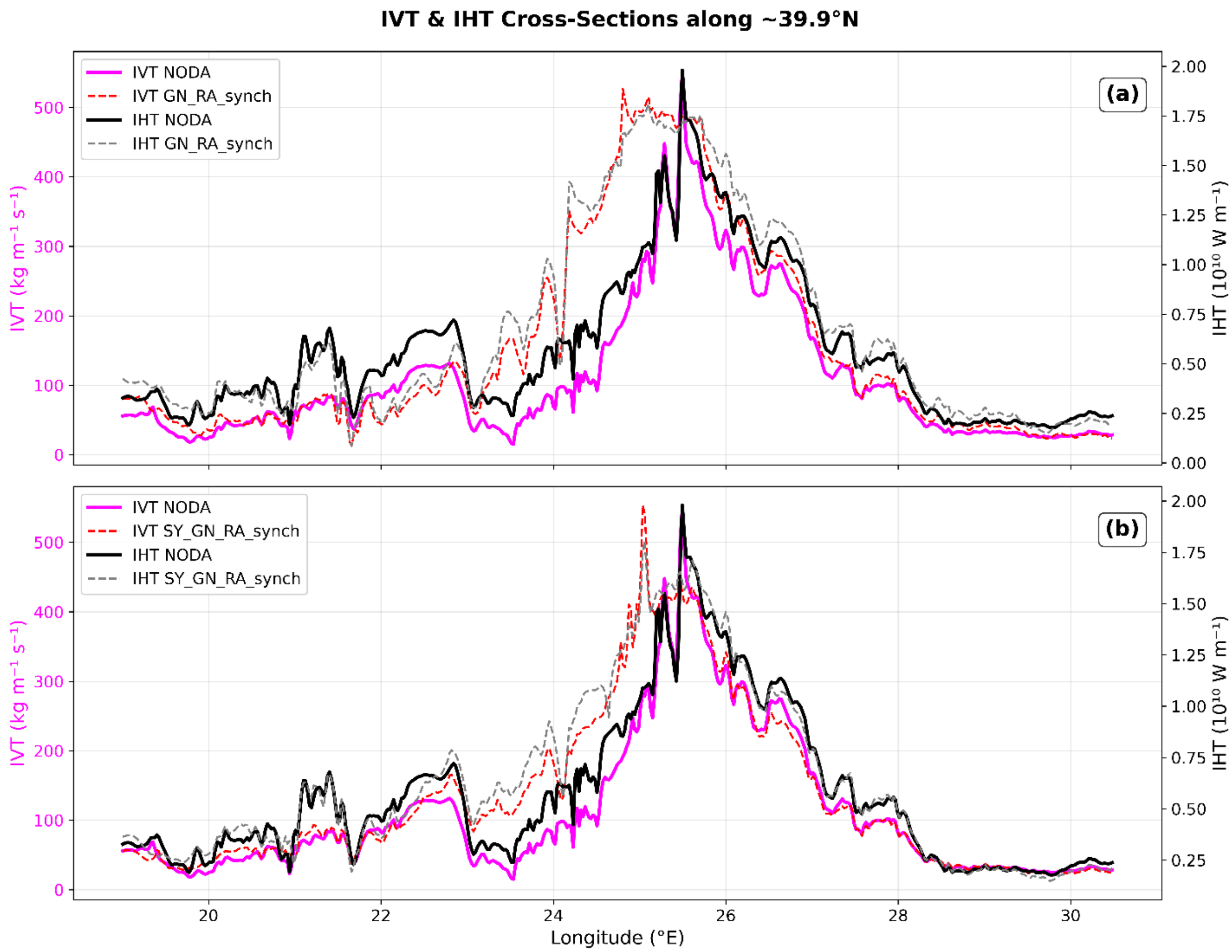

Fig. S11. Longitudinal profile of IVT and IHT (integrated from the surface to about 700 hPa across 39.9 ºN (Lemnos transect)). Solid curves represent the NODA, while dashed curves illustrate the impact of radar data assimilation GN_RA_synch (a) and SY_GN_RA_synch (b).

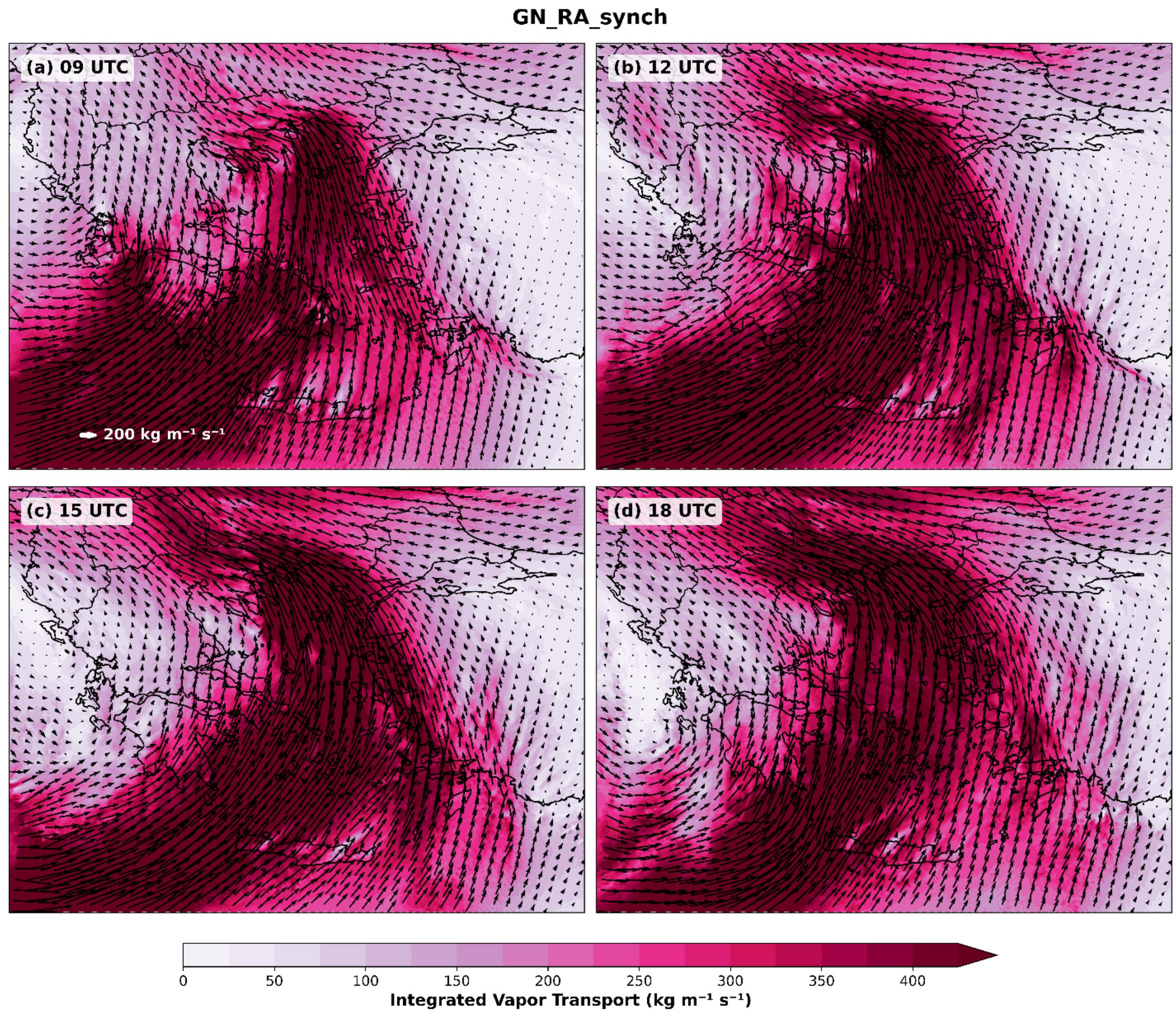

Fig. S12. Horizontal water vapor mixing ratio transport integrated from surface up to about 300hPa (corresponds to 22^{th} eta level) (IVT) of GN_RA_synch. The figures show the evolution of IVT every 3 hours from 09 UTC to 18 UTC on 30/11/2024.

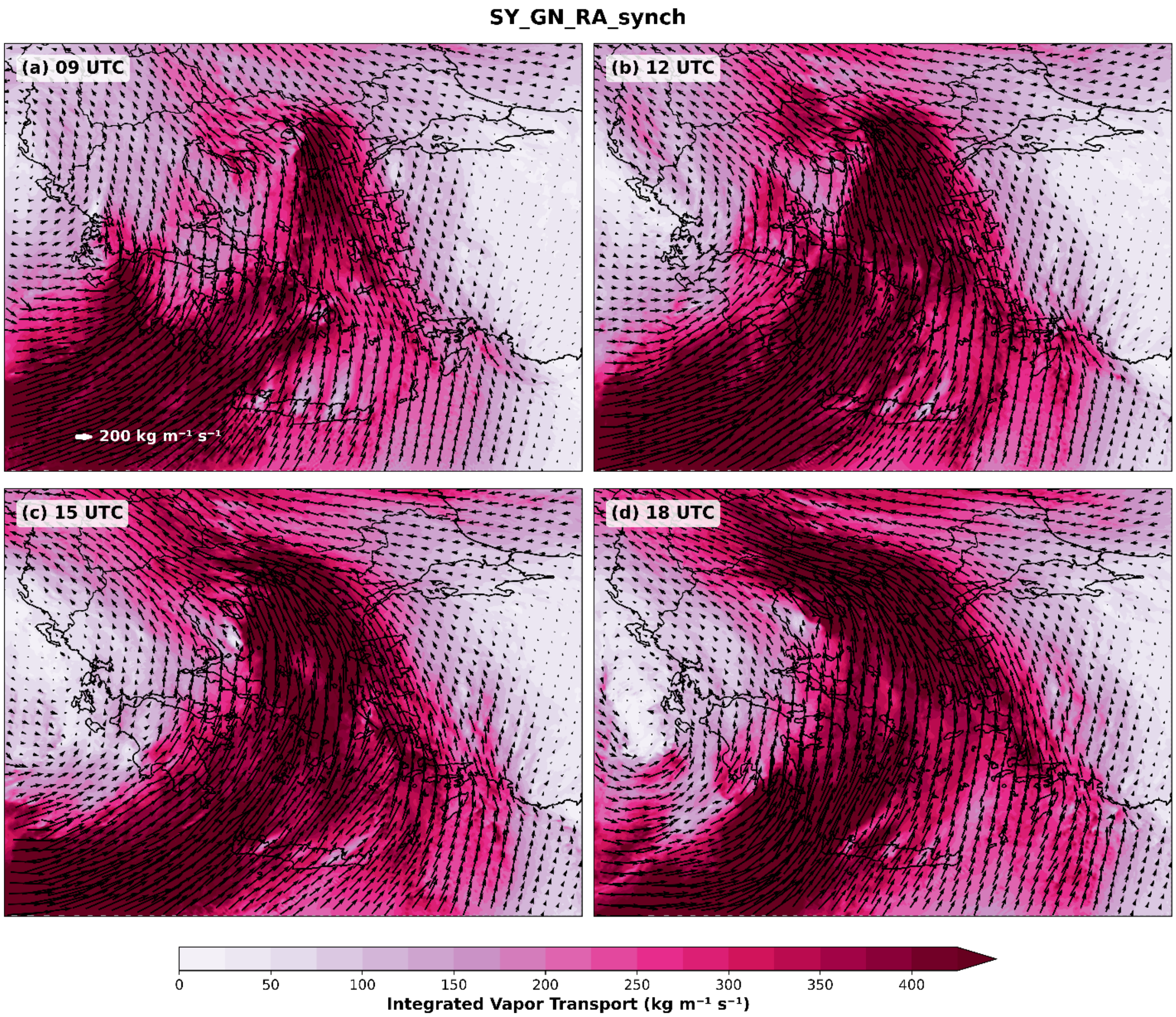

Fig. S13. Horizontal water vapor mixing ratio transport integrated from surface up to about 300hPa (corresponds to 22th eta level) (IVT) of SY_GN_RA_synch. The figures show the evolution of IVT every 3 hours from 09 UTC to 18 UTC on 30/11/2024.

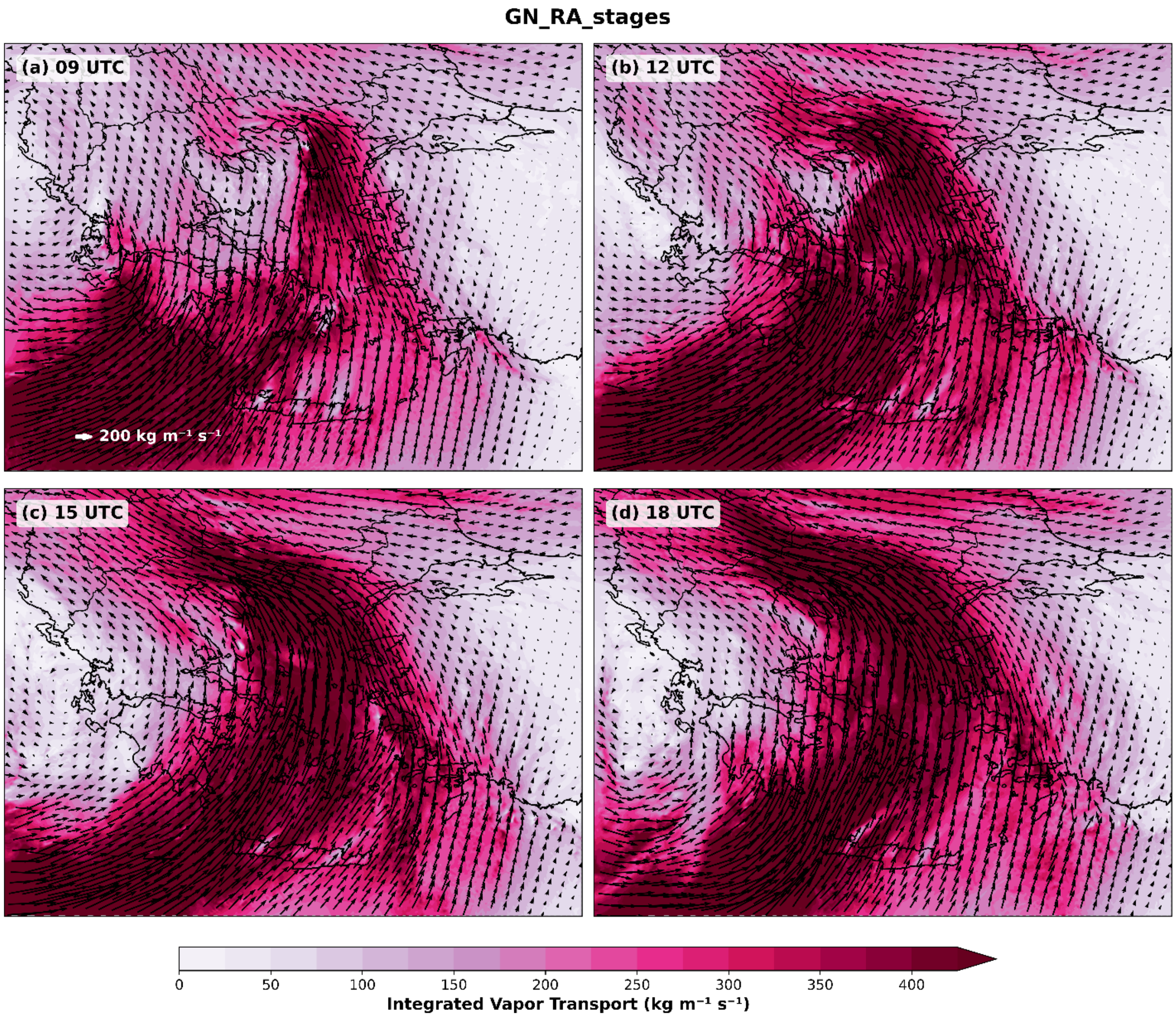

Fig. S14. Horizontal water vapor mixing ratio transport integrated from surface up to about 300hPa (corresponds to 22th eta level) (IVT) of GN_RA_stages. The figures show the evolution of IVT every 3 hours from 09 UTC to 18 UTC on 30/11/2024.

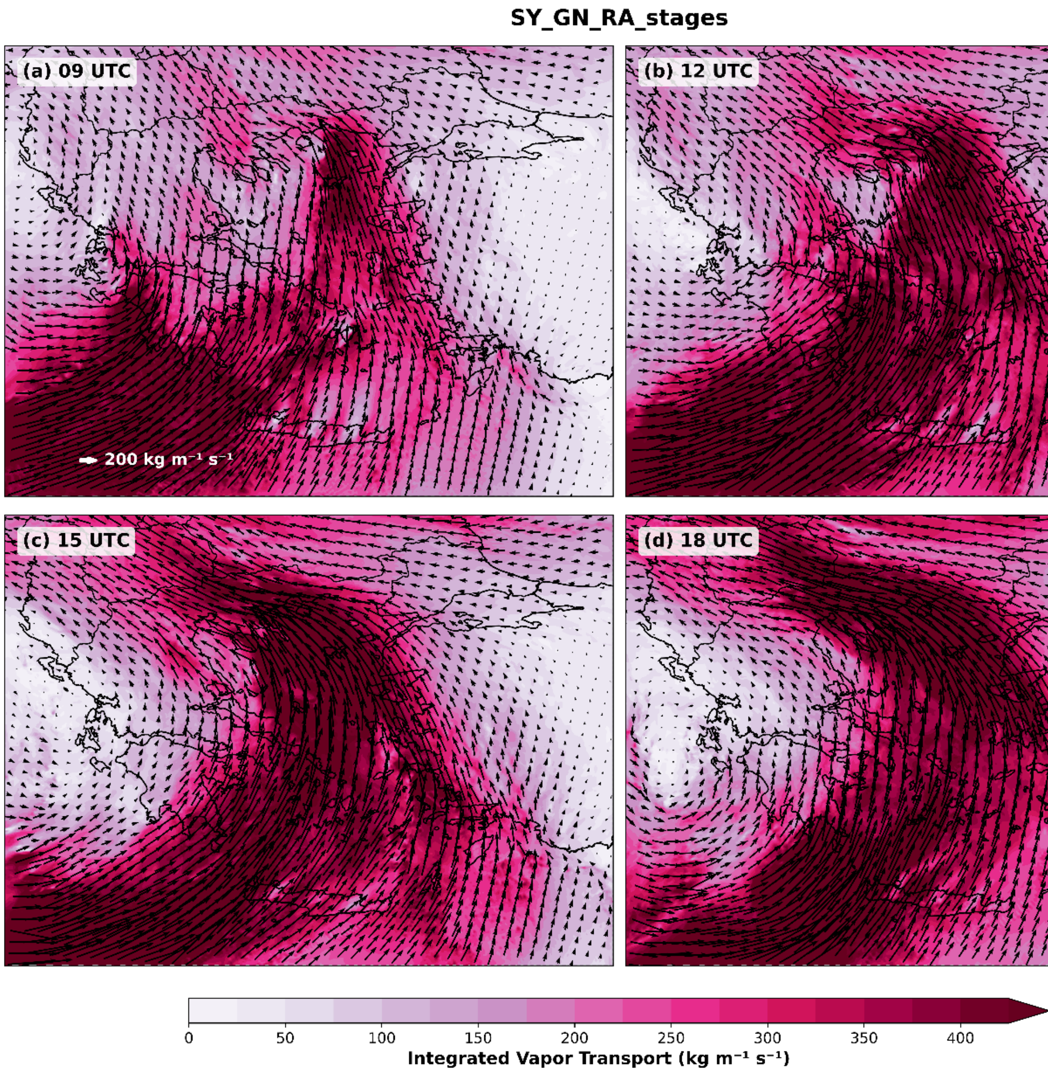

Fig. S15. Horizontal water vapor mixing ratio transport integrated from surface up to about 300hPa (corresponds to 22th eta level) (IVT) of SY_GN_RA_stages. The figures show the evolution of IVT every 3 hours from 09 UTC to 18 UTC on 30/11/2024.

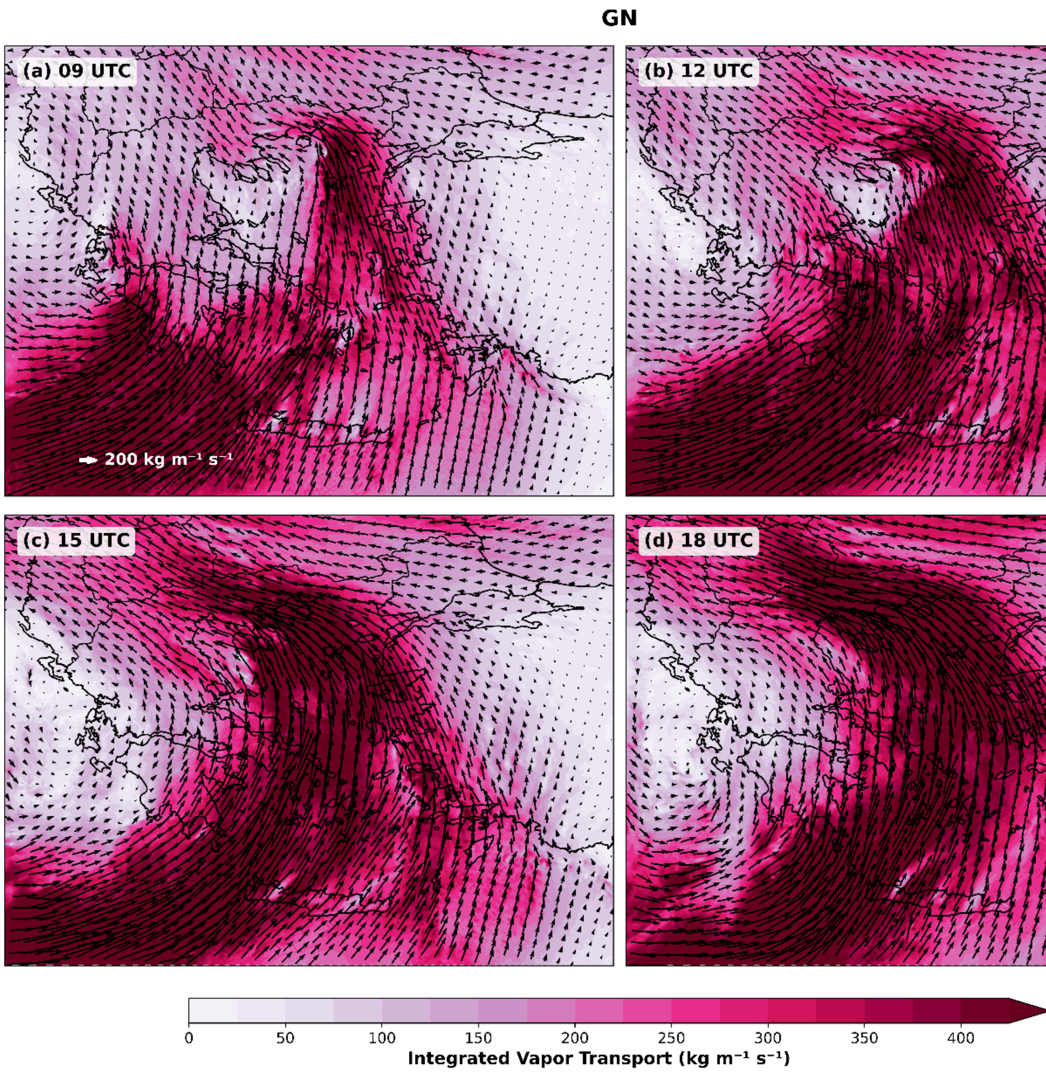

Fig. S16. Horizontal water vapor mixing ratio transport integrated from surface up to about 300hPa (corresponds to 22th eta level) (IVT) of GN. The figures show the evolution of IVT every 3 hours from 09 UTC to 18 UTC on 30/11/2024.

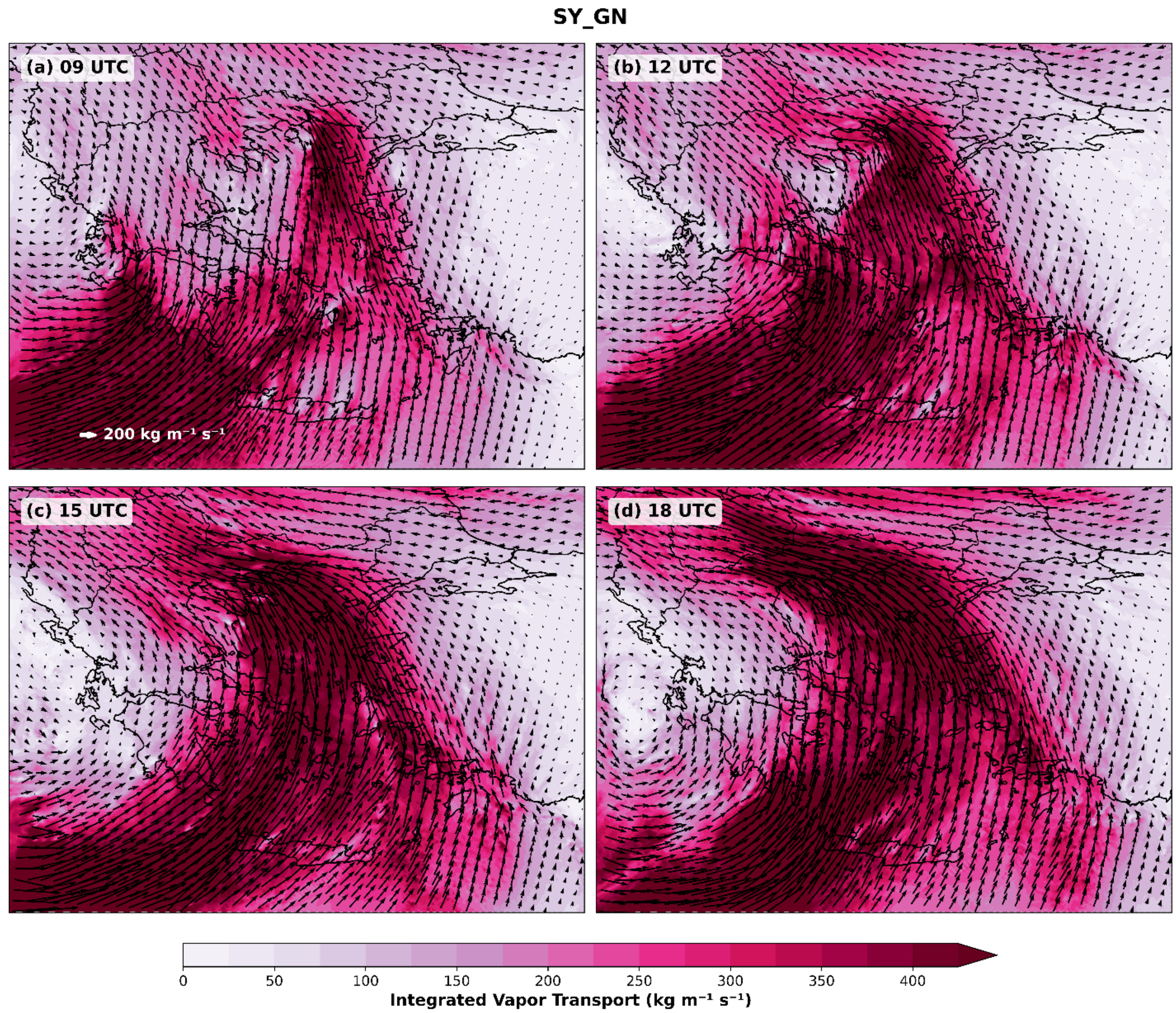

Fig. S17. Horizontal water vapor mixing ratio transport integrated from surface up to about 300hPa (corresponds to 22th eta level) (IVT) of SY_GN. The figures show the evolution of IVT every 3 hours from 09 UTC to 18 UTC on 30/11/2024.